Fabrication of Microfluidic Devices for Artificial Respiration

by

Hyesung Park

B.S. Physics
Illinois State University, 2004

SUBMITTED TO THE DEPARTMENT OF MECHANICAL ENGINEERING IN PARTIAL
FULFILLMENT OF THE REQUIREMENTS FOR THE DEGREE OF

MASTER OF SCIENCE IN MECHANICAL ENGINEERING
AT THE
MASSACHUSETTS INSTITUTE OF TECHNOLOGY

JUNE 2007

Signature of Author: _____ **Signature redacted** _____
Department of Mechanical Engineering
May 21, 2007

Certified by: _____ **Signature redacted** _____
Todd Thorsen
Assistant Professor of Mechanical Engineering
Signature redacted Thesis Supervisor

Certified by: _____
Richard Gilbert
Visiting Scientist, Department of Mechanical Engineering
Thesis Supervisor

Signature redacted

Accepted by: _____
- Lallit Anand
Graduate Officer, Department of Mechanical Engineering
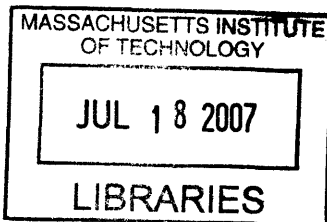
(This page intentionally left blank)

Fabrication of Microfluidic Devices for Artificial Respiration

by

Hyesung Park

Submitted to the Department of Mechanical Engineering on May 21,
2007 in Partial Fulfillment of the Requirements for the Degree of Master
of Science in Mechanical Engineering

Abstract

We are developing elastomeric polydimethylsiloxane (PDMS) microfluidic devices incorporated with photoactive thin films to create an implantable artificial respiration platform. Whereas state-of-the-art respiration support machines deliver oxygen gas directly to the blood via external macroscale devices, our technique utilizes a biomimetic photocatalytic process to generate energy from light and thus produce dissolved oxygen from water which is already present in the blood. Blood oxygenation will be achieved by the interaction between the photoactivated metal oxide film and blood in the setting of a molded microfluidic conduit, providing a stable and implantable oxygenation platform. As a basic, scalable building block, we developed a noble "network" design which was structurally similar to the native pulmonary capillary network. The interconnected channel geometry was designed in such a way to minimize shear stress and reduce hemolysis and thrombosis inside the microchannel. It allowed alternative flow pathways in the event of single channel occlusion while minimizing the establishment of detrimental pressure gradients. The hemocompatibility analysis demonstrated that the network construct showed acceptable levels of hemolysis rate ($< 8\%$) and thrombus formation. Critical to the success of this project is the understanding of the manufacture parameters for microfluidic devices molded from elastomeric materials like PDMS. In the initial development of our work, we performed the following three tasks to generate manufacture protocols for elastomeric microfluidic devices that will be ultimately used for biological applications: 1) Curing schedules of the heat-cure PDMS elastomers under various fabrication parameters were characterized. 2) The interlayer bonding chemistry of the double layer PDMS device was analyzed followed by subsequent mechanical analysis. 3) The efficacy of various surface treatment techniques on hydrophobic PDMS surfaces was investigated using fluorescently tagged bacteria (*E. Coli*) flowed through microchannels as reporter particles to measure non-specific adhesion, which will provide useful information in minimizing channel fouling for biological applications.

Thesis Supervisors: Todd Thorsen
Title: Assistant Professor of Mechanical Engineering

Richard Gilbert
Title: Visiting Scientist, Department of Mechanical Engineering

(This page intentionally left blank)

Acknowledgements

(This page intentionally left blank)

Contents

List of Tables and Figures

(This page intentionally left blank)

Chapter 1

Introduction

Major advances in health care over the past several decades have resulted in the reduction of mortality for most major diseases, such as cancer and cardiovascular disease. However, few major advances in patients with end-stage lung diseases were achieved during the same time period. In fact, the death rate of the chronic lung disease has continued to increase and this is largely due to inadequate means for providing intermediate and long-term respiratory support. While numerous technical solutions have been proposed and implemented over the past decades, the availabilty of a platform that provides a safe, reliable method of blood oxygenation remains elusive. The most common means for improving gas exchange in patients with acute respiratory failure has relied on closed, positive-pressure mechanical ventilation system. However, adverse effects such as oxygen toxicity, altered metabolism, and barotraumas are common, and these effects may in turn result in further injury to the already failing lungs and add significantly to morbidity and mortality.

Mechanical ventilation supports have been made possible by extracorporeal membrane oxygenation (ECMO) and intravenous membrane oxygenation (IVOX) techniques. Both of these approaches, however, have critical drawbacks which make them less appropriate for practical application.

ECMO augments oxygenation by promoting gas diffusion across a microporous membrane and gained a great attention as a mean to restore normal gas exchange.[1] Furthermore, technical improvements made this technology possible to be employed during cardiac bypass.[2-4] Nonetheless, ECMO suffered from several limitations. This technology requires a large and complex blood pumping and oxygenator system, and surgical cannulation. In addition, such membranes exibit frequent protein adsorption and platelet adhesion, and are associated with bleeding and infection. The natural extension

of ECMO was intravenous membrane oxygenation which was based on the ability of hollow fiber membranes to diffuse oxygen and carbon dioxide. While the IVOX technology improved oxygenation and hemodynamics, it was still limited by a low level of gas exchange, high number of adverse events, and device malfunctions.[5]

One of the most important recent advances in lung therapy has been the improvement in techniques for performing lung transplantation.[6-7] However, this approach, for several reasons, does not give a desirable solution to patients with chronic lung diseases either. First, the number of viable donors by far falls short of than the demand; even if there are enough supplies, temporizing during pre-transplantation is still very challenging. Also, the highly complex and strict matching process of donor lungs between the donors and recipients renders the lung transplantation extremely difficult.[8-9] Therefore, despite improvement in surgical techniques, methods for obtaining and preserving donor lungs will be not easily solved in the near future.

While prior ECMO-based efforts have sought to achieve intravascular respiration by diffusing gases across permeable, thin-walled, hollow fibers, we propose a fundamentally different approach. Rather than to deliver oxygen gas directly into the blood, our technology employs photocatalytic energy to generate oxygen from the water already present in the blood, thereby eliminating the need for exogenous gas delivery.

Photocatalytic processes are routinely used in nature to harness energy from light in order to drive chemical reactions. For example, photosynthesis utilizes energy derived from sunlight to drive key metabolic processes in green plants; it is based on the ability of a metal complex chromophore of magnesium and a transition metal oxide cluster of manganese to use light energy to produce charge separation, which then results in the generation of dissolved oxygen. When applied to blood in the manner proposed, DO binds rapidly to hemoglobin without the conversion to a gas phase. This approach avoids membrane diffusion barriers associated with hollow fiber technologies and further eliminates the exposure of tissue and blood to the mechanically disruptive effects of gas sparging. Therefore, the proposed artificial lung technology will apply these physical principals to create an artificial system, composed of durable biomimetic materials, designed to replicate normal respiratory function. The core technology utilizes a robust semi-conducting metal oxide photolytic thin film, TiO_2 in anatase form, as both the

photo-absorption element (on the light illumination side) and a DO generating porous film (on blood contact side). The pores in the TiO_2 thin film are nano-scale, which provides high reaction surface area while preventing blood cells and proteins from direct contact. TiO_2 semi-conductor material is selectively excited by a narrow bandwidth UV light and thus avoids wasted radiation by transmission. This technology avoids the need for gas-to-liquid diffusion membranes, pressurized gas, and gas cylinders. By generating oxygen directly from the water content of whole blood, we eliminate the need for gas delivery while retaining the full benefit of the red blood cell's ability to rapidly capture and transport dissolved oxygen.

The overall goal of this research is to develop a high quantum yield photo-transducing surface, which can be linked to flowing blood at the microfluidic scale in order to replicate pulmonary capillary respiration.

1.1   Development of Photocatalytic Respiration System

For the past decades, the most common techniques for improving gas exchange in patients with respiratory failure relied mostly on closed, mechanical ventilation system, which is based on the delivery of oxygen gas into the bloodstream via gas permeable hollow fibers.[10-12] The principal weakness of this system is that it requires major diffusion boundary layers, which results in slowed mass transport since the technology depends heavily on the membrane diffusivity and differential gas pressure in order to acheive O_2/CO_2 exchange, thus in need of a large surface area to achieve sufficient flux of gases. Furthermore, this system requires a continuous source of exogenous pressurized oxygen gas as well.

Here, we present an alternative approach for regulating intravascular respiration in which dissolved oxygen (DO) and oxyhemoglobin are generated from the water content of whole blood based on the interaction of UV light with a semi-conducting nanocrystalline titanium dioxide thin film. This idea has already been validated by showing the possibility of generating dissolved oxygen from the water content of synthetic serum, based on the interaction of UV light with a semi-conducting titanium dioxide thin film.[13] The driving force for this reaction is the displacement of electrons at

the photoactive surface following photon absorption. The photo-electronic interaction of metal chelate chromophores with transition metal oxides forms the basis for light-dependent oxygen gas generation in photosynthetic (PS) organisms; cyanobacteria, green algae, phycobilisomes (cyanobacteria and red algae), and higher plants.[14-17] The technology proposed herein builds upon the ability of the semiconducting anatase form of titanium dioxide, TiO_2, to serve both as the chromophore and the charge separation center[18-21] for such reactions. These results have allowed us to propose a model of artificial intravascular respiration, based on the ability of transition metal oxides to carry out optoelectronic conversion, and then to use the resulting charge separation to generate oxygen from the water content present in whole blood (Figure 1.1). The feasibility of this photolytic generation of dissolved oxygen and oxyhemoglobin formation in whole blood has already been demonstrated, a pivotal step in the development of an artificial technology for autonomous intravascular gas exchange. [13]
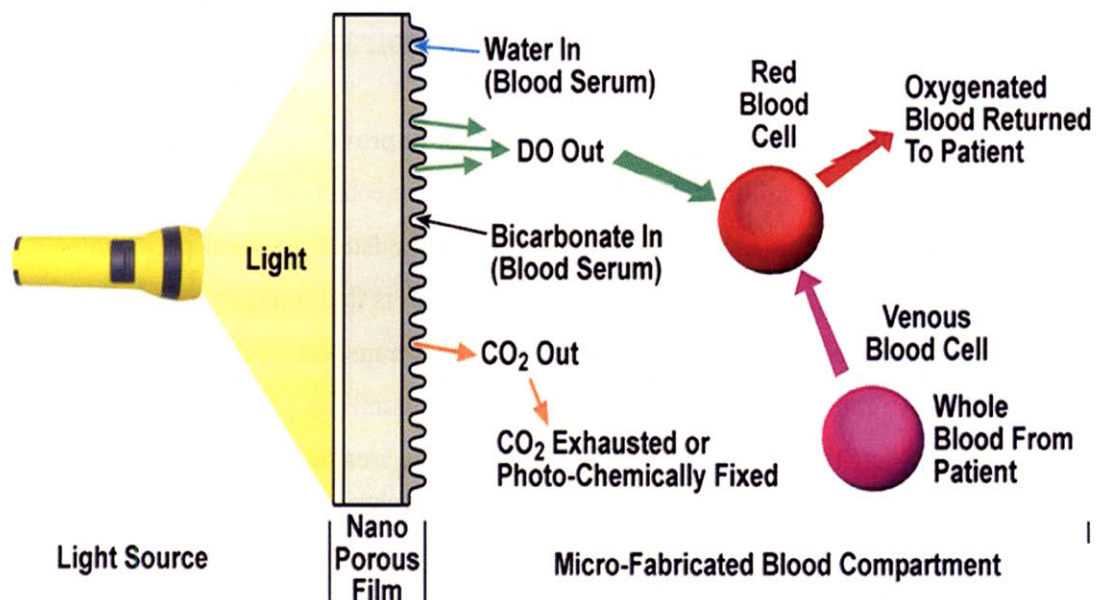
Figure 1. 1 Diagram showing the fundamental mechanism of a photolytic DO generation and oxyhemoglobin formation. The photolytic technology is based on the ability of transition metal oxides to convert light energy to electric current; the resulting charge separation is used to generate oxygen from adjacent (non diffusion) water molecules supplied from serum. The photochemical materials are designed to produce DO directly in an aqueous fluid (blood), without involving the gaseous phase, which is freely available for binding with hemoglobin. The photolytic artificial lung technology utilizes a semi-conducting metal oxide material, TiO_2, as

both the photo-absorption element and photochemically driven chemical conversion center. The light energy produces charge separation (electron-hole pairs) in the semi-conductor, which results in the production of active oxygen, hydrogen ions and free electrons.

1.2   Related works and goals

While the ultimate goal of the project is to create an elastomer-based (PDMS) artificial respiratory platform capable of partially assisting or replacing the human lung, this platform provided a model system to develop robust manufacture protocols for molded PDMS microfluidic devices since critical to the success of this project also lies in better understanding of the manufacture parameters for microfluidic devices molded from elastomeric materials like PDMS. In the initial development of our work, we characterized the curing schedules for the heat-cure PDMS elastomers by studying different monomer/catalyst ratio, curing time, and aspect ratio, which are described in detail in chapter 2. Once the curing parameters for individual and double-layer PDMS devices have been established, the interlayer bonding properties of multi-layer devices were investigated by analyzing the mechanical strength of the device; chapter 3 describes this in detail. Based on the manufacture protocols developed from chapters 2 and 3, surface modification protocols for PDMS polymers were investigated in chapter 4. Several methods, such as polymer coating or grafting, oxygen plasma treatment, and chemical treatment with strong acid, were discussed and the efficacy of each method was compared. With the essential fabrication techniques being developed, chapter 5 focuses on the fundamental technology that lies in the development of artificial respiration device emphasizing biocompatibility and oxygenation of the prototype device.

(This page intentionally left blank)

Chapter 2

Curing Schedules for PDMS Elastomers

2.1   Material selection

In order to manufacture such microfluidic devices introduced earlier, we used polydimethylsiloxane (PDMS), a two-part (monomer/catalyst) elastomeric material whose ideal mixing ratio is 10:1 parts A:B (Dow Corning Sylgard 184). PDMS is widely used in the fabrication of microchannel systems for biological applications since features can be reproduced with high fidelity by replica molding, it is optically transparent (suitable for detection schemes, *e.g.*, UV absorbance and fluorescence), and it is non-toxic. Mammalian cells can be cultured directly on PDMS and devices made from it can be implanted *in vivo*, and its low curing temperature and ease of fabrication make it ideal for soft lithography and rapid prototyping.[22] Also, PDMS is particularly appropriate for the oxygenation application due to its high permeability to oxygen gas, whose diffusivity is approximately $6 \times 10^{-9} m^2 s^{-1}$.[23] Despite the aforementioned benefits of PDMS, its hydrophobic surface makes it susceptible to non-specific protein adhesion, a particular concern for microfluidic devices to be used in biological assays. However, both chemical and physical modifications of the PDMS surface can increase its biocompatibility by rendering the surface hydrophilic or entropically unfavorable for protein adhesion. Currently available methods include oxygen plasma treatment, polymer coating or grafting, and chemical treatment with strong acids.[24-33]

2.2 Fabrication Process

2.2.1 Mold Fabrication

The fundamental technology that is used for the fabrication of the microfluidic device is based on the soft lithography. Soft lithography is a molding technique using etched or microfabricated structures created by photolithography as templates to fabricate high-quality microstructures or nanostructures. Most well known techniques include replica molding[34], microtransfer molding[35], microcontact printing[36], micromolding in capillaries[37], and solvent-assisted micromolding[38-39] Table 2.1 summarizes the minimum resolution that can be achieved from each method.

Method	Resolution
Replica molding	30 nm
Microtransfer modling	1 μm
Microcontact printing	35 nm
Micromolding in capillaries	1 μm
Solvent-assisted micromolding	60 nm

Table 2. 1 Various techniques of soft lithography

In soft ligthgraphy, an elastomeric stamp is patterned with relief structures on its surface. This method makes use of flexible organic materials rather than rigid inorganic materials which are commonly used in micro-electro-mechanical systems and provides a simple, low-cost method for micro- and nanostructure fabrication. Figure 2.1 illustrates general process for soft lithography, the so called rapid prototyping procedure; Once the design for the desired device is created using computer aided design (CAD) program, the pattern is transferred to a transparency mask from a high resolution printer (3550 dpi, Mikacolor, CA). Master for replica molding is prepared from negative (SU-8 50, Micochem) photoresist on a 3" silicon wafer (Silicon Quest, CA) at Experimental

Materials Laboratory (EML) from MIT following standard photolithography processes: negative photoresist was spun coated at 1000 rpm for 45 seconds on a silicon wafer to produce 100 μm high channels followed by pre-bake, UV exposure, post bake, and development.
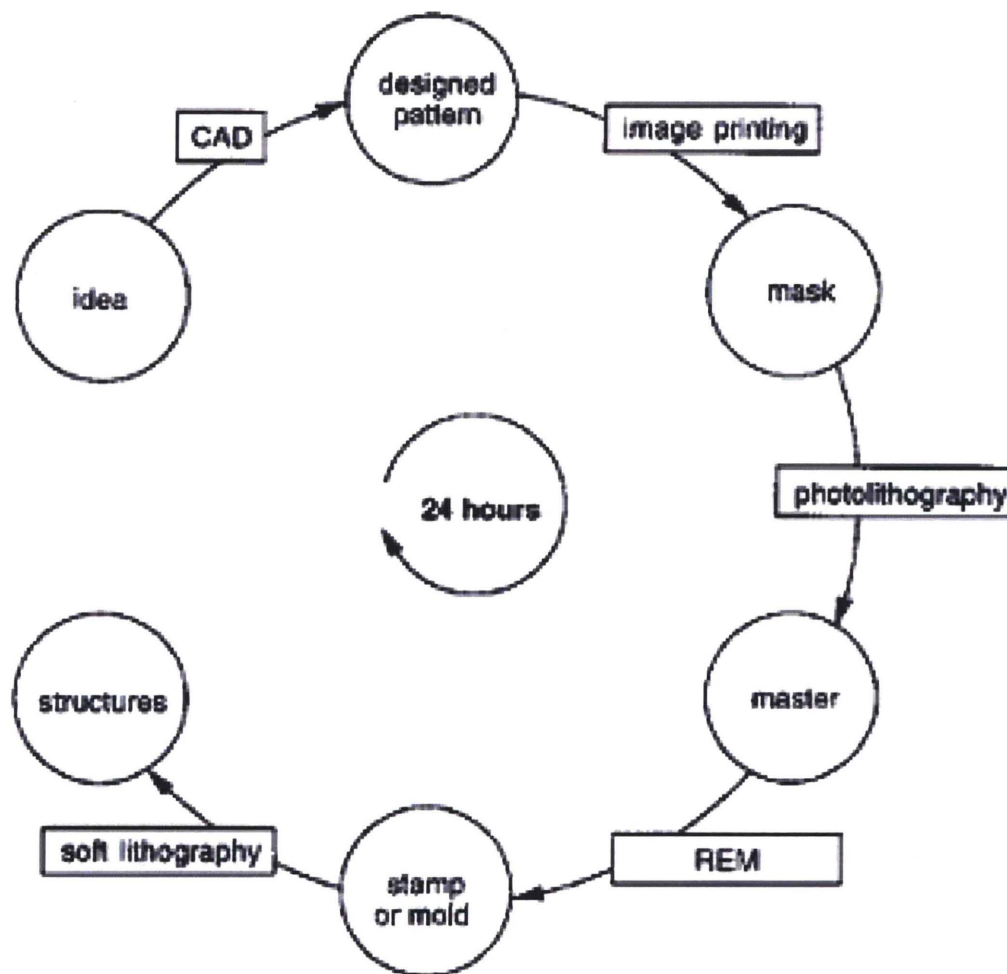
Figure 2. 1 Rapid prototyping procedure for soft-lithography.[40] The overall procedure from the device design to the stamping takes less than 24hours to complete.

2.2.2 Device Fabrication

Figure 2.2 describes the overall process for both the single and double layer microfluidic device fabrication. The 2D structure of microfluidic device was fabricated from poly (dimethylsiloxane) (PDMS) by replica molding from the master that has already been prepared. 5:1 monomer/catalyst mixture was mixed and degassed and then poured on the control mold to approximately 5 mm thickness (thick gas layer). This mold was again degassed under vacuum to remove air bubbles generated while PDMS was poured onto the mold. At the same time, 20:1 mixture of PDMS was prepared and spin-coated at 1000 rpm for 60 seconds onto the flow mold to 120 μm thickness (thin flow layer) yielding approximately 20 μm thickness membrane between the control and flow layer. Both molds were individually baked at 80°C for 11 to 19 minutes. Before coating the molds with PDMS, they were first treated with silane (high molecular trichloro-perfluorooctyl silane, Aldrich) for 10 minutes to prevent the adhesion of the PDMS onto the molds and enable easy mold release of the PDMS structure. After the primary bake, the partially cured control layer was peeled off from the mold, holes for the inlets and outlets were punched with a 20G surgical steel Luer Stub (BD), and optically aligned to the flow layer under a microscope. It is important to note that mask for the control layer needs to be scaled to 101.7 % in order to account for the shrinkage of the thick layer of PDMS during curing. This two-layer structure was again baked in an oven for additional 3 hours at 80°C to form a strong covalent bond between the two layers. During this secondary baking period, the two layers of PDMS, each of which has an excess of monomer and catalyst, start to cross-link resulting in a monolithic structure.[41] After the secondary bake, the final structure was cut and peeled off from the mold and bonded onto the glass slide via oxygen plasma to seal the flow channel, thus completing the fabrication process. Oxygen plasma bond provides a strong irreversible bond between the PDMS structure and the substrate which can withstand pressures up to 30 – 50 psi.[22]

Photoresist spin coated on the silicon wafer

5:1

UV exposure to the photoresist through mask

20:1

Develop photoresist

Cast PDMS onto the mold

Fabrication of two-layer structure:
Top layer (5:1)
Bottom layer (20:1)

Peel-off PDMS and puch inlets and outlets

Bond to the substrate

Fabrication process of PDMS device: Single Layer

photoresist

Silicon wafer

PDMS

UV

mask

glass substrate

Figure 2. 2 Schematic diagram of the mold fabrication process: Left column depicts the fabrication process of a single layer device and the right column describes multi-layer fabrication process.

2.3   Experimental and Results

To establish curing schedules for the heat-cure PDMS elastomers, we developed a PDMS bonding table for two-layer microfluidic devices whose monomer/catalyst mixing ratios were 5: 1 and 20:1 respectively. Individual layers of PDMS were cured at 80°C in an oven and secondary baking time was fixed for 3 hours. Microfludic test devices, described in Figure 2.3, were fabricated by varying the primary curing time and feature size (aspect ratio) while keeping the channel height constant at 100 μm: Channel widths were varied from 1.920 mm (which is somewhat large in terms of microfluidic scale) down to 0.587 mm. The primary curing time of individual layers was varied from 11 to 19 minutes.
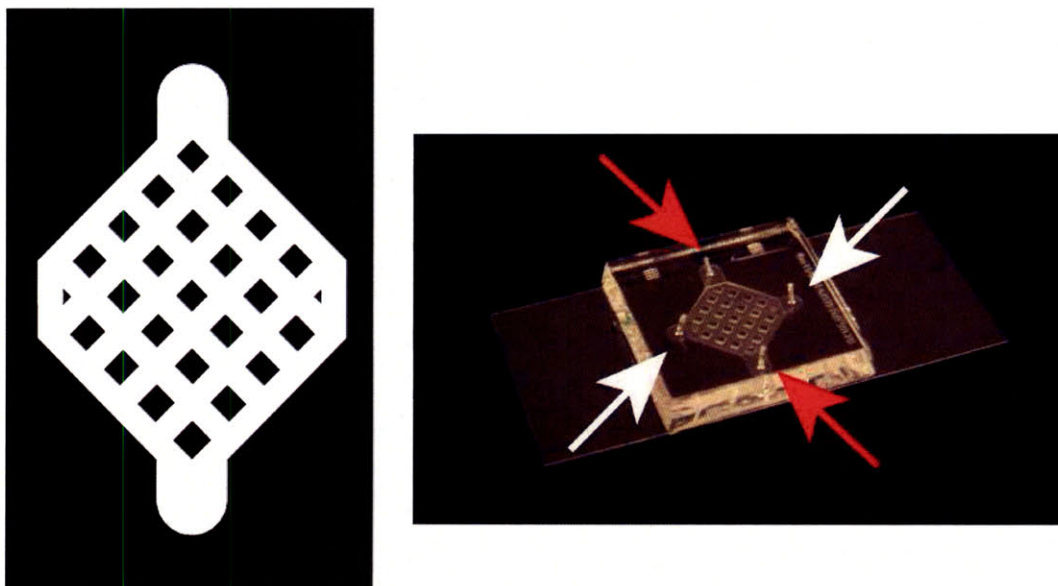
Figure 2. 3 Left: Schematic diagram of mesh type microfludic device. This device mimics the pulmonary alveolus structure of human lungs. Both top and bottom layers have the same configuration. The dimensions of each mesh (dark square) and channel (white region) width have the same length scale. Flow inlet and outlet are punched on the top and bottom circular channel regions. Each mold for the two layers consists of 100 μm high microchannels constructed from negative SU-8 photoresist photolithographycally patterned on a silicon wafer. Right: Diagram of double layer device. White arrow indicates flow channel and red arrow indicates gas channel.

The effective bonding between the two layers of PDMS was visually confirmed after the final structure of PDMS devices were peeled off from the mold. Properly bonded structures completely came off from the mold whereas inefficiently bonded structures did not entirely come off resulting in tearing the bottom (thin) layer of PDMS. There were even occasions where the inter-layer bonding was so weak that the top (thick) layer alone came off from the mold which was still entirely coated with a thin layer of PDMS.

A primary cure time of 15 minutes was found to be sufficient enough to release the thick (5:1) PDMS layer from its respective mold, and create a firm PDMS surface on the spin-coated wafer. Crude layer-layer adhesion tests were carried out after the secondary baking step, using tweezers to try to mechanically separate the layers (precision tests done in Chapter 3 using the Zwick/Roell testing machine in the Materials Laboratory at MIT). Excellent covalent bonding was observed for the narrower channels (0.59 mm to 0.84 mm) with primary cure times between 15 and 19 minutes. After 19 minutes, the layers were overcured, and frequent layer-layer adhesion failure was observed. For channels with larger widths (1.20 mm and above), creeping of the elastomer up and over, and along the edges of microchannels on the spin-coated mold was observed, which created an uneven surface profile of PDMS that led to inefficient layer-layer adhesion. This creeping elastomer caused formation of air pockets between the top and bottom layer when they were brought into contact and lessened the strength of layer-layer adhesion. Frequent adhesion failure was also observed for thin layer (bottom layer) microchannels with high aspect ratios (defined as width/height, >10:1). Even for the devices with well-bonded structures, they sometimes could not be considered as successful because the thin inter-layer membrane stuck to the top surface of the thick upper layer (top layer) microchannels thus blockading the channels in the top layer. Both the successful and unsuccessful bonding of the double layer devices are illustrated in Figure 2.4.
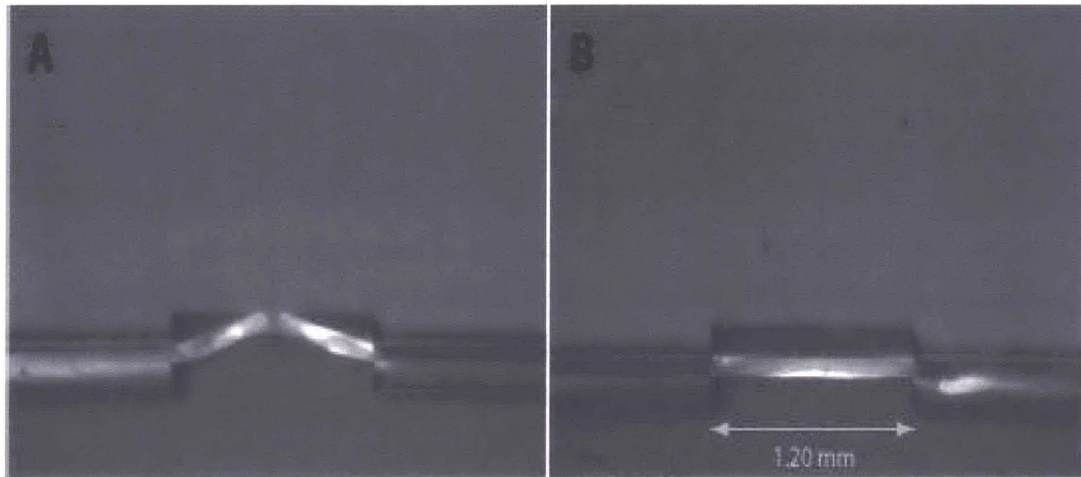
Figure 2. 4 Cross-sectional view of the two layer microfluidic device. A: Channels in which interlayer membrane stuck to the top surface of the gas layer. B: Diagram of successful fabrication of two layer device.

Creeping of the elastomer around the microchannels can be improved by simply increasing the height of PDMS layers spun coated on the mold by reducing the rpm of spin coater. Experiments demonstrated that reducing the rpm from 1000 to 800 greatly improved the creeping regions over and around microchannels thereby removing regions trapped with air pockets. Letting the spin-coated PDMS mold sit for a while (1-2 hours) also helped keeping the elastomer from creeping up and over the microchannels. On the other hand, the problem of inter-layer membrane attachment can be simply resolved by increasing the channel height of the top layer.

Channel Width (Interlayer surface area) / Bake Time	1.92 mm (45mm ×45mm)	1.71 mm (45mm ×45mm)	1.20 mm (23mm ×35mm)	0.84 mm (23mm ×23mm)	0.59 mm (23mm ×23mm)
11 min	Incomplete curing of each layer				
13 min	Incomplete curing of each layer				
15 min	X	X	X	O	O
17 min	X	X	X	O	O
19 min	X	X	X	O	O

Table 2. 2 Double layer of PDMS bonding table established by varying primary curing time and channel size (aspect ratio). O/X indicates layer-layer bonding success/failure.

(This page intentionally left blank)

Chapter 3

Interlayer Bonding Chemistry and Mechanics

In microfluidic structures with multiple layers, it is critical to verify the layer-layer bonding strength is sufficient to withstand any applied external pressure through the microchannels in order to prevent any channel leakage activity. Fortunately, the flow rate implemented in most microfluidic devices is in general quite slow, on the order of microliters per minute, with corresponding pressures of tens to hundreds of Pascal. Therefore, for most of the applications, thermal or plasma bonding provides enough sealing to work with in microfluidics. However, better understanding of the interlayer bonding chemistry and mechanics would provide useful information not only for the individual devices to be analyzed in research but in developing appropriate manufacture protocols in industry as well.

In this chapter, layer-layer adhesion characteristics were investigated for multilayer molded PDMS-based microfluidic devices. Bonding chemistry was analyzed as a function of catalyst ratio in individual layers, cure temperature, and interlayer surface area. Subsequent mechanical analysis of the bonded layers was conducted by measuring the force (both shear and normal force) required to separate the layers, and optical analysis of the separated parts was conducted to assess failure mode (simple delamination, tearing, etc.). Additional mechanical layer-layer adhesion tests were performed by applying pressure through microchannels whose boundaries are formed by the layer interface, looking for channel burst activity as a function of applied pressure.

3.1   Shear Stress

Shear Stress can be easily calculated by the applied force divided by the interlayer surface area between the top and bottom layers of PDMS.

$$\tau = \frac{F}{A} \quad (1)$$

, where τ is shear stress, F is applied force (shear load), and A is the area of layer interface (area resisting shear). Strictly speaking, eq. (1) must be interpreted as the average shear stress. However, since the distribution of direct shear stress is usually complex and not easily determined, it is common practice to assume that the shear force F is uniformly distributed over the shear area A.

3.1.1 Device description

In order to determine the test platform for the shear stress test on the multi-layer PDMS devices, several prototypes were investigated.

Legend:
- Glass
- PDMS
- Laxen
- Clamp

1st Generation

2nd Generation

3th Generation
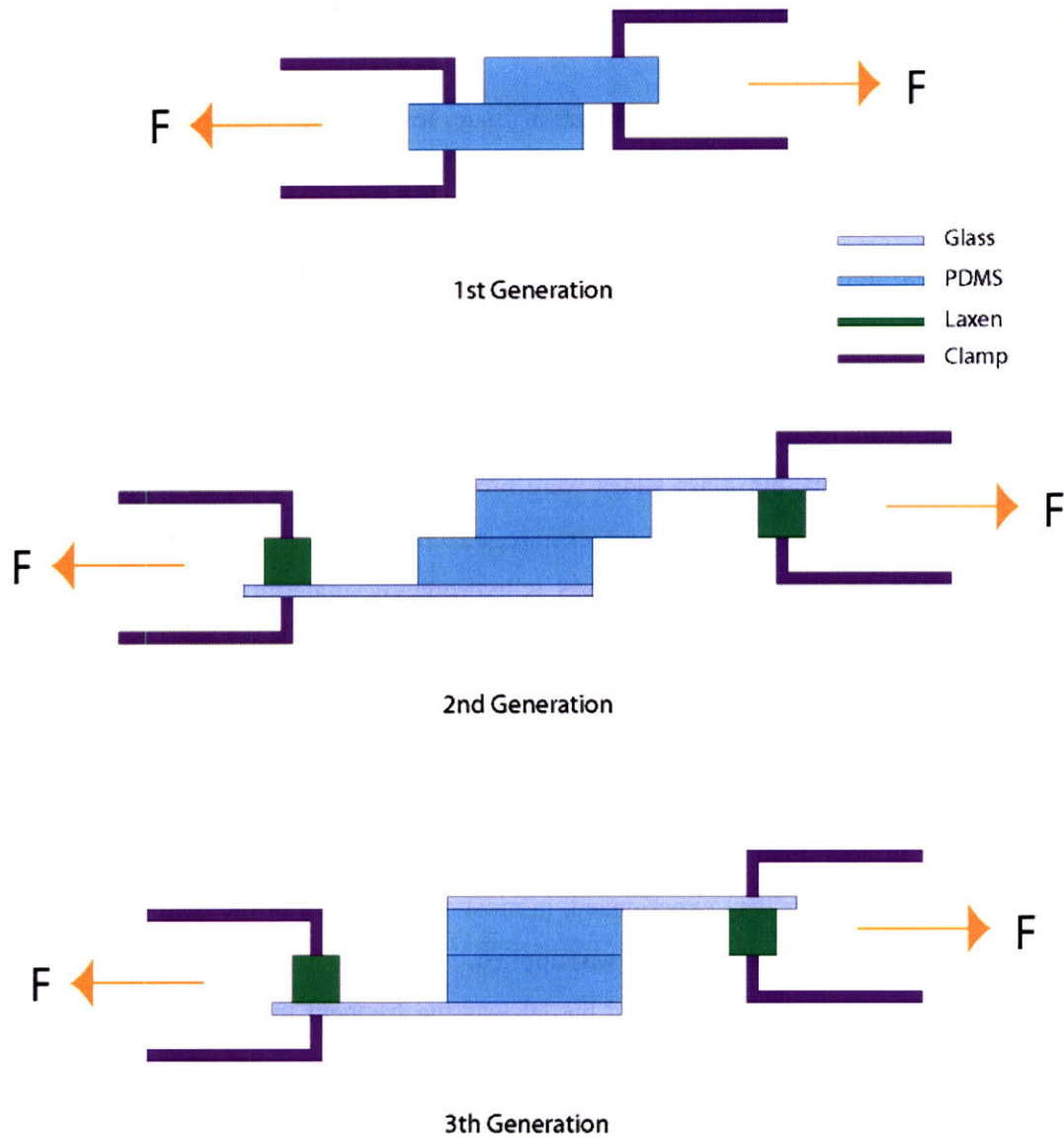
Figure 3. 1 Evolution of the test platforms for shear stress

Initially, the two layers of PDMS were thermally bonded, using layers with different catalyst ratios to form a covalent bond at the interface, with some offset so that each end of the layers could be placed on the clamp of the Zwick machine. This model turned out to be extremely inappropriate. PDMS, for being elastomer material, deformed greatly, especially for the higher ratios of monomer/catalyst layers, while the clamp was being tightened; this distorted the applied force to the interface between the two layers

and often times caused splits at the edges of the interlayer surface even before the force is applied to the test device.

In order to overcome the deformation issue, test samples were attached to glass slides via oxygen plasma bonding. At the ends of the glass slide, posts were mounted, which was about the same height as the individual layers of PDMS, so that the external force could be applied uniaxially. The choice of a fragile material like glass as the substrate for the test sample over other materials, such as metal or wood, was to minimize any rotational motion of the sample while the force was applied to the sample. If there was any significant rotational movement of the sample, which occurred from time to time during the experiment, the glass slides were broken before the external force had any noticeable impact on the sample. Furthermore, attaching PDMS to materials like wood or metal is also challenging; since PDMS is hydrophobic material, conventional glues would not work on PDMS surface. One trick that can be used, however, is to treat the surface of PDMS with oxygen plasma since exposing PDMS to plasma oxidation renders the surface hydrophilic and aqueous solutions can easily wet the oxidized surfaces.[42] However, the oxidized surface of PDMS is very unstable in air and reverts to being hydrophobic in less than 30 minutes. Nonetheless, experiments demonstrated that samples prepared in this way experienced, in most cases, failure of the bonding between the sample and glass slide while force was applied.

The drawback with the second model was the frequent tearing of PDMS at the interface where the offset between the two layers began during the application of the force to the specimen, rendering it hard to observe the desired interlayer failure mode. When external loads were applied, the downward or upward movement of the edge around the interlayer surface was pulling the other contacting surface of PDMS layer. This first caused tearing of surface along the edge, then subsequent tearing of the PDMS underneath the edge. One might assume that this is the inter-layer failure mode due to the applied external force and conclude that the specimen could withstand that specific amount of force to break the interlayer bond. However, the tearing around the edge would not have happened if both layers of the same dimension were placed precisely on top of each other, as shown in the 3rd generation schematic, thus resulting in the increase of threshold of applied external force required to break the layer-layer adhesion.

Therefore, we adopted the 3rd generation model as the test platform for future experiments, in which the offset between the two layers of PDMS was removed and top and bottom layers of the same dimensions were aligned exactly on top of each other. Figure 3.2 illustrates the actual test sample that has been used.
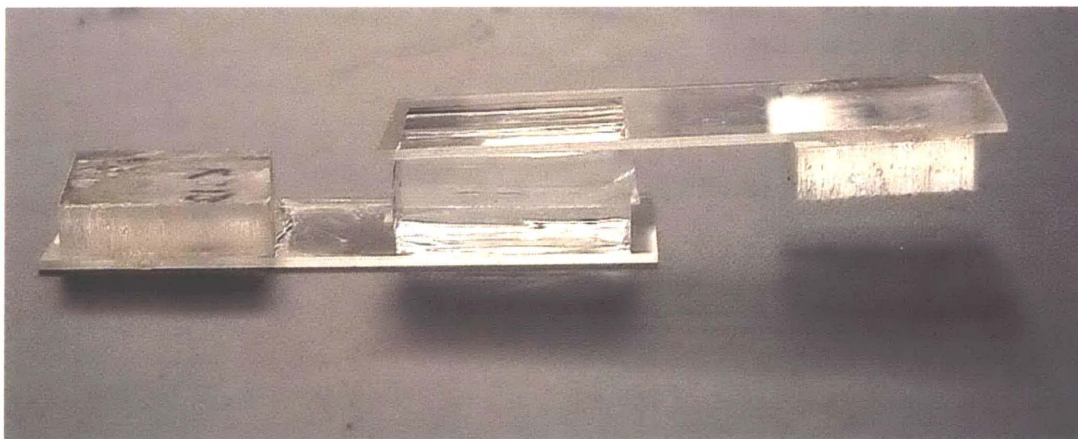
Figure 3. 2 Description of the shear stress test device.

3.1.2 Experimental and Results

In order to analyze the bond strength of the cure bonded double layer PDMS structure by measuring the shear force required to break the layer-layer adhesion, test samples were prepared by varying three parameters: catalyst/monomer ratio, secondary cure time, and interlayer surface area. Four sets of catalyst/monomer ratios for the double layer structure were investigated; 1:3/1:30, 1:4/1:25, 1:5/1:20, and 1:6/1:15. Two sets of secondary cure time were tested; 3 hours and 14 hours while primary curing time was kept between 16 and 18 minutes for excess catalyst layers and 66 to 98 minutes for excess monomer layers. Two sets of sample dimensions were analyzed; 20 mm × 30mm and 20mm × 15 mm while the height of both layers were maintained at 4 ~ 5 mm. These test parameters are summarized below.

Experimental protocols:

A) Primary Bake Time (at 80°C)
- 1:3 ~ 16 min
  1:30 ~ 80 min + 16 min
- 1:4 ~ 17 min
  1:25 ~ 70 min + 16 min
- 1:5 ~ 18 min
  1:20 ~ 60 min + 18 min
- 1:6 ~ 18 min
  1:15 ~ 50 min + 18 min

B) Secondary Bake Time (at 80°C)
- 3 hours
- 14 hours

C) Interlayer surface dimension
- 20 mm × 15 mm
- 20 mm × 30 mm

Two failure modes on the sample were observed from the applied shear force. One of them was the interlayer bond break and the other was PDMS layer tearing which occurred at the weakest point of the bonding, *i.e.* the interface between the PDMS layer and glass slide, before the interlayer bond failure.

Experiments demonstrated that, for the fixed secondary curing time and interface dimensions, the overall bond strength increased from the 1:6/1:15 device to the 1:4/1:25 device. However, it was hard to characterize the bond strength of the 1:3/1:30 samples since these samples were so rubbery resulting in very frequent PDMS tearing at the 1:30 layers before we could observe any adhesion failure. When interface dimensions and catalyst/monomer ratios were kept constant, the overall bond strength turned out to be higher for samples with longer secondary baking time. Varying the interlayer surface area while keeping the polymer mixing ratio and secondary curing time constant yielded an interesting outcome. For 14 hours secondary baking time, it took more force to separate samples with larger interlayer surface area. However, the opposite phenomenon was observed for 3 hours secondary cure time; more force was required to break the interlayer bonding for samples with smaller interlayer surface area. This phenomenon

might be explained from the fact that 3 hours of secondary curing did not provide sufficient time for the devices with larger interlayer surface area to have as good of bond strength as the devices with smaller interlayer surface area. Figure 3.3 illustrates the distribution of the shear stress for different combination of parameters and table 3.1 shows the maximum values at each of these combinations.

Mixing Ratio (Catalyst : Monomer) = 1:3 & 1:30

Legend:
- 20by15_14HR: AVG(136.7) / STD(2.7)
- 20by30_14HR: AVG(159.6) / STD(9.9)
- 20by15_3HR: AVG(104.2) / STD(10.0)
- 20by30_3HR: AVG(75.4) / STD(3.3)

Y-axis: Shear stress (KPa); X-axis: # of samples

Mixing Ratio (Catalyst : Monomer) = 1:4 & 1:25

Legend:
- 20by15_14HR: AVG(180.1) / STD(6.6)
- 20by30_14HR: AVG(201.2) / STD(6.6)
- 20by15_3HR: AVG(135.9) / STD(6.3)
- 20by30_3HR: AVG(80.7) / STD(9.4)

Y-axis: Shear Stress (KPa); X-axis: # of samples
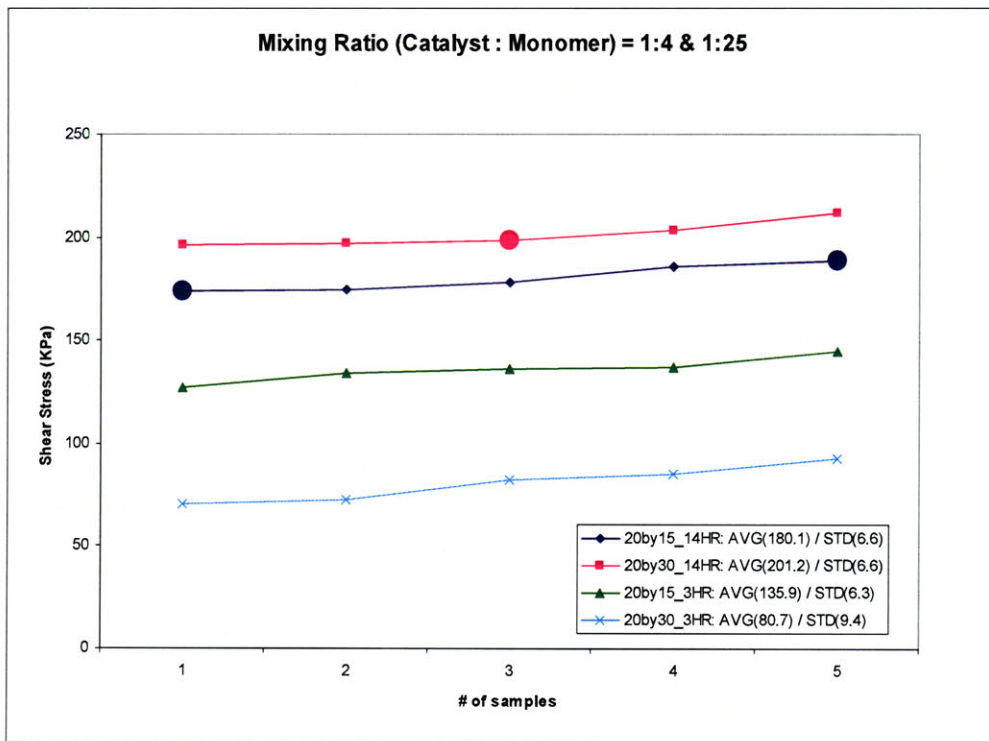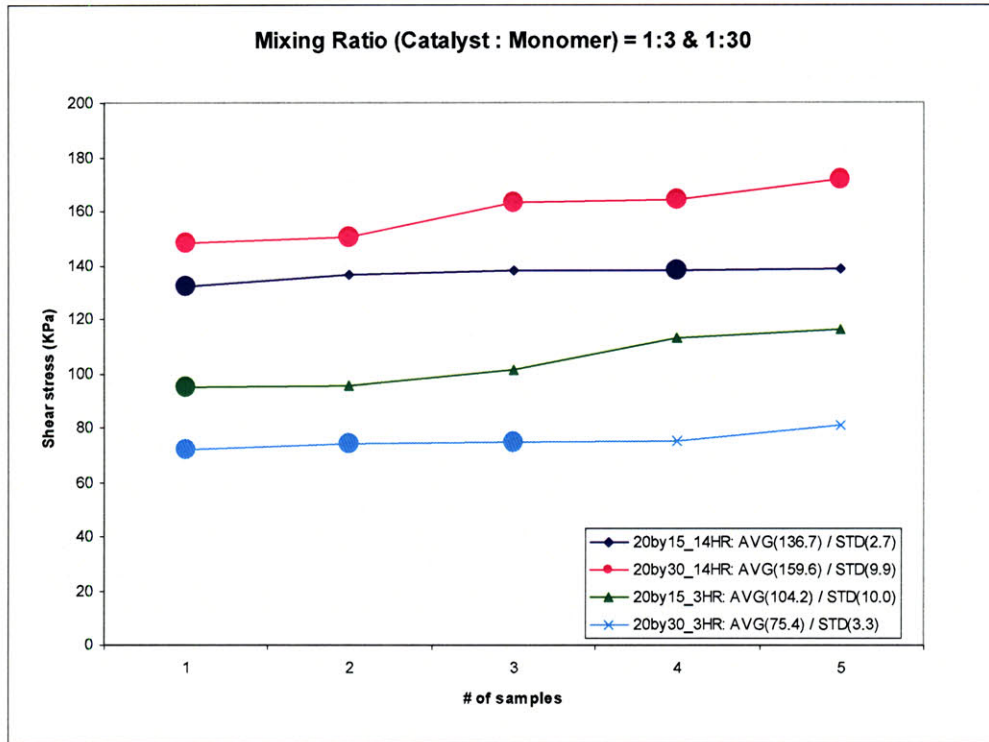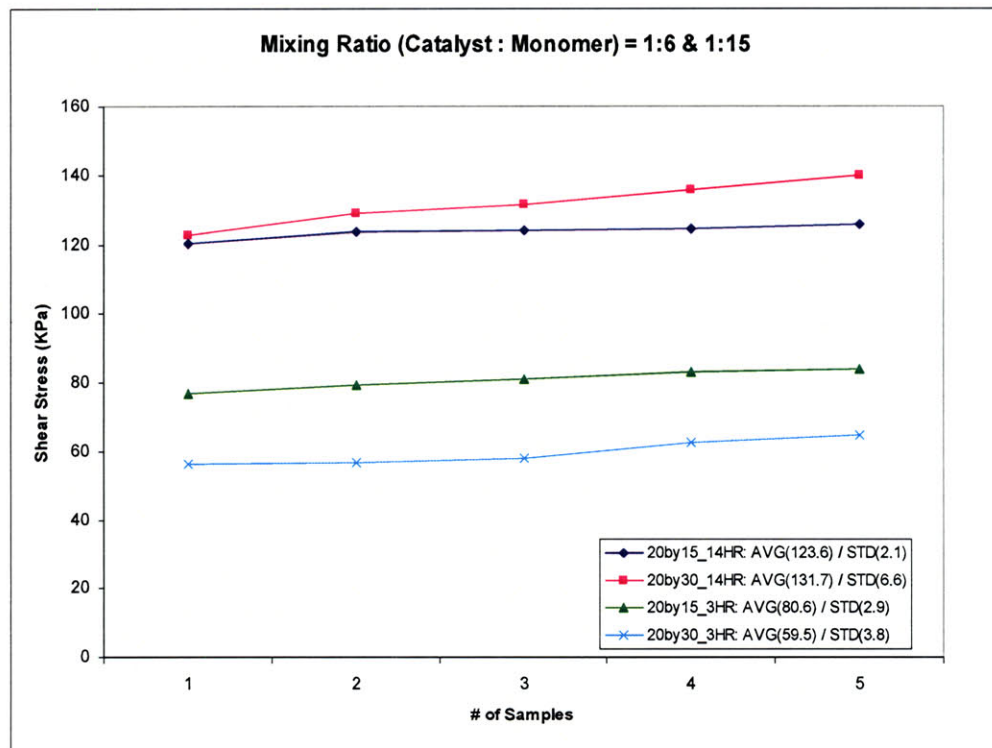
Figure 3. 3 Distribution of shear stress. Big circular sample points indicate PDMS tearing failure mode at the weakest point

Shear stress (kPa / psi)		1:3 / 1:30	1:4 / 1:25	1:5 / 1:20	1:6 / 1:15
3hour	20mm×15mm	116.4 / 16.9	144.8 / 21.0	92.9 / 13.5	83.8 / 12.2
	20mm×30mm	80.8 / 11.7	93.0 / 13.5	72.1 / 10.5	64.5 / 9.4
14hour	20mm×15mm	138.7 / 20.1	188.4 / 27.3	175.9 / 25.5	125.8 / 18.2
	20mm×30mm	171.7 / 24.9	211.8 / 30.7	200.2 / 29.0	139.8 / 20.3

Table 3. 1 Maximum values of shear stress for each combination of parameters.

3.2 Normal stress

Normal stress was investigated in a similar manner as the shear stress except now the applied force was in the direction perpendicular to the interlayer surface.

3.2.1 Device Description

PDMS samples were prepared in the same way as the shear stress test samples. These two layer devices were treated with oxygen plasma and bonded to the glass slides. Subsequently, T-shape aluminum pieces were attached to these glass slides completing the fabrication of the test platform. Figure 3.4 illustrates the schematic and actual test samples.
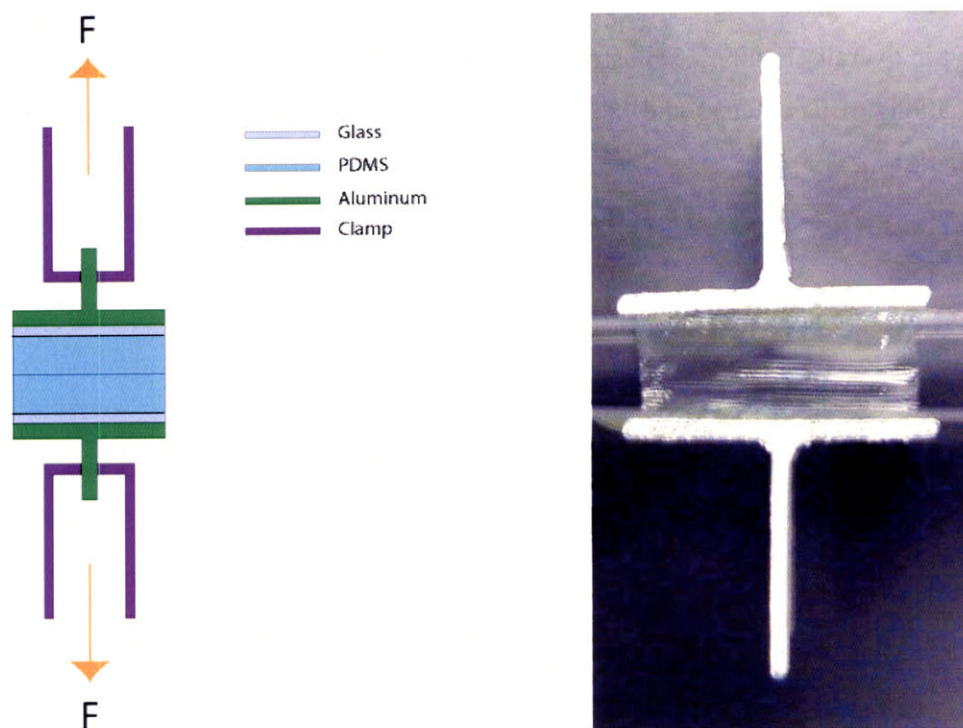
Figure 3. 4 Left: Schematic diagram of the normal stress test platform. Right: Description of the test device

3.2.2 Experimental and Results

Bond strength of the two layer PDMS devices was investigated by measuring the normal stress required to break the interlayer adhesion. The parameters varied in preparation of the test samples were the same as the shear stress case.

Similarly to the shear stress test, two failure modes, interlayer bond break and PDMS tearing at the weakest point, were observed. The observed values of the normal stress fluctuated a lot more than those from shear stress test. One common trend was the dominant PDMS failure mode (tearing in weakest spot) observed in 1:3/1:30 devices. Therefore, one might deduce that this specific mixing ratio would yield the strongest layer-layer adhesion in the heat cured double layer device. Furthermore, the effect of interlayer surface area was found to be more significant in the normal stress test: more force required in breaking the layer-layer adhesion for samples with larger interlayer

surface area. Also, longer secondary baking time produced more robust interlayer bonding in overall. Figure 3.5 illustrates the distribution of the normal stress for different combinations of parameters and table 3.2 shows the maximum values at each of these combinations.

Mixing Ratio (Catalyst : Monomer) = 1:3 & 1:30

Mixing Ratio (Catalyst : Monomer) = 1:4 & 1:25

Mixing Ratio (Catalyst : Monomer) = 1:5 & 1:20

Legend:
- 20by15_14HR: AVG(124.6) / STD(5.9)
- 20by30_14HR: AVG(187.4) / STD(30.8)
- 20by15_3HR: AVG(108.3) / STD(18.6)
- 20by30_3HR: AVG(135.9) / STD(45.6)

Mixing Ratio (Catalyst : Monomer) = 1:6 & 1:15

Legend:
- 20by15_14HR: AVG(130.5) / STD(11.3)
- 20by30_14HR: AVG(263.6) / STD(26.1)
- 20by15_3HR: AVG(132.7) / STD(13.8)
- 20by30_3HR: AVG(145.9) / STD(21.0)
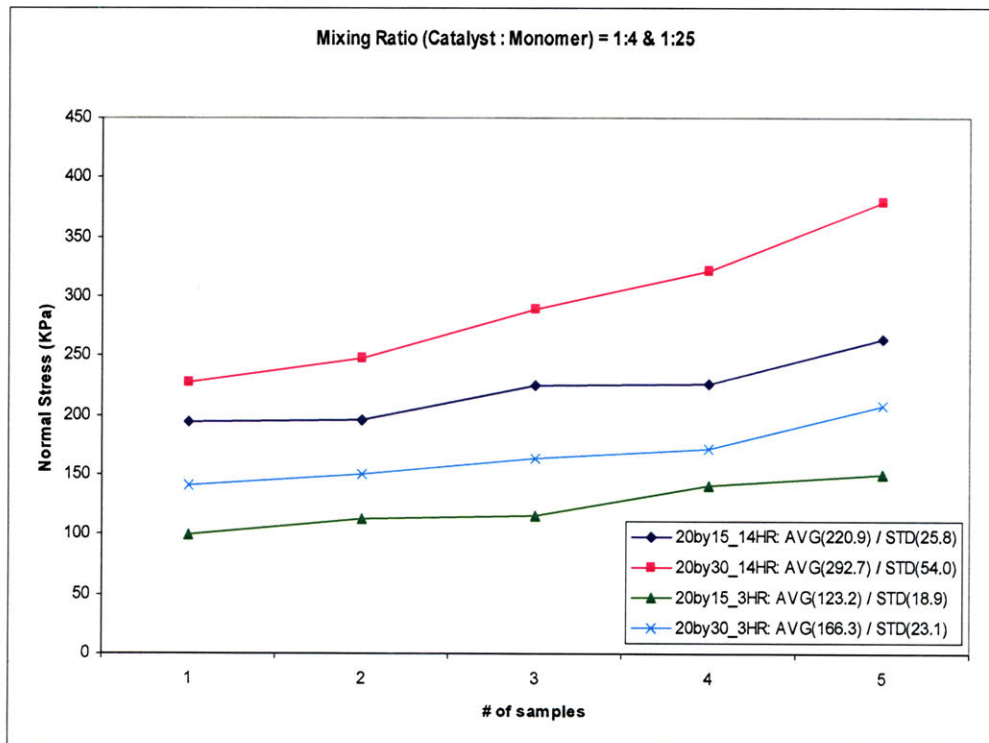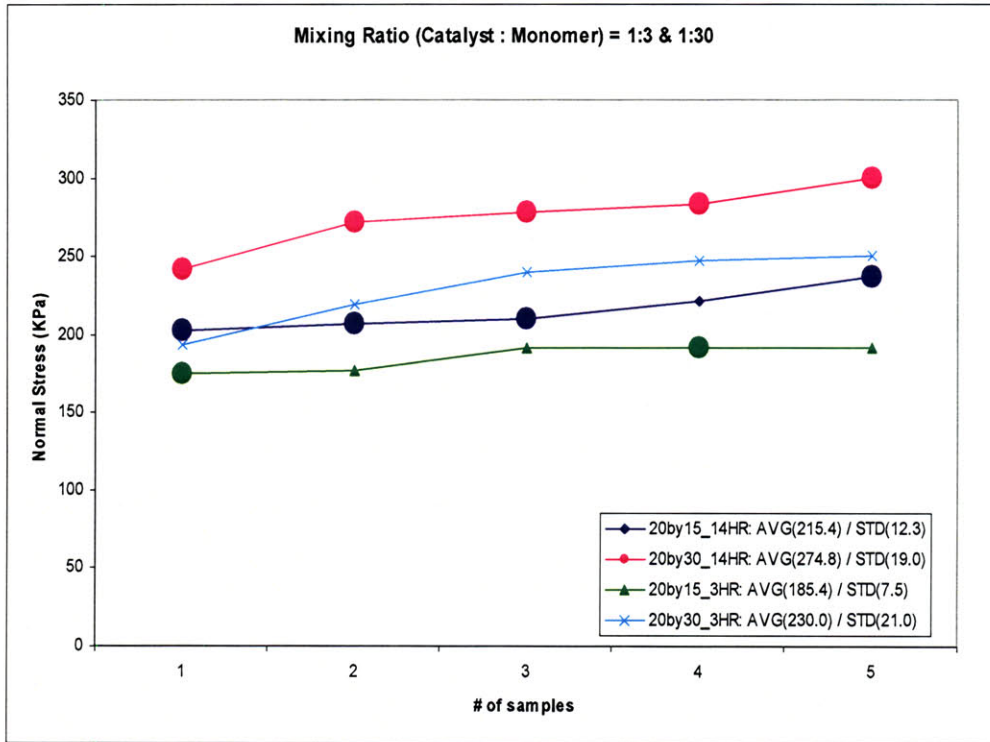
Figure 3. 5 Distribution of normal stress. Big circular sample points indicate PDMS tearing failure mode

Normal stress (kPa / psi)		1:3 / 1:30	1:4 / 1:25	1:5 / 1:20	1:6 / 1:15
3hour	20mm×15mm	191.8 / 27.8	149.4 / 21.7	131.5 / 19.1	156.0 / 22.6
	20mm×30mm	249.8 / 36.2	207.2 / 30.1	197.5 / 28.6	172.1 / 25.0
14hour	20mm×15mm	236.4 / 34.3	264.4 / 38.3	133.5 / 19.4	149.7 / 21.7
	20mm×30mm	299.5 / 43.4	379.0 / 55.0	232.9 / 33.8	306.6 / 44.5

Table 3. 2 Maximum values of normal stress for each combination of parameters.

3.3 Interlayer Burst Analysis

Previous shear and normal tests were conducted with samples in which no microchannels were patterned by directly applying mechanical forces to the samples. In order to investigate more realistic situations in microfluidic settings, interlayer burst tests were performed; Top layers of the PDMS were patterned with microchannels and cure bonded to another PDMS substrate layers. Nitrogen gas was directly flown inside the microchannels in order to determine the critical pressure at which interlayer burst occurs.

3.3.1 Device Description

The mold for microchannels was fabricated using standard photolithography. The top layer was replica molded from this master and then cure bonded to the blank PDMS substrate layer. Figures 3.6 and 3.7 illustrates the schematic diagrams and actual images of the test sample.
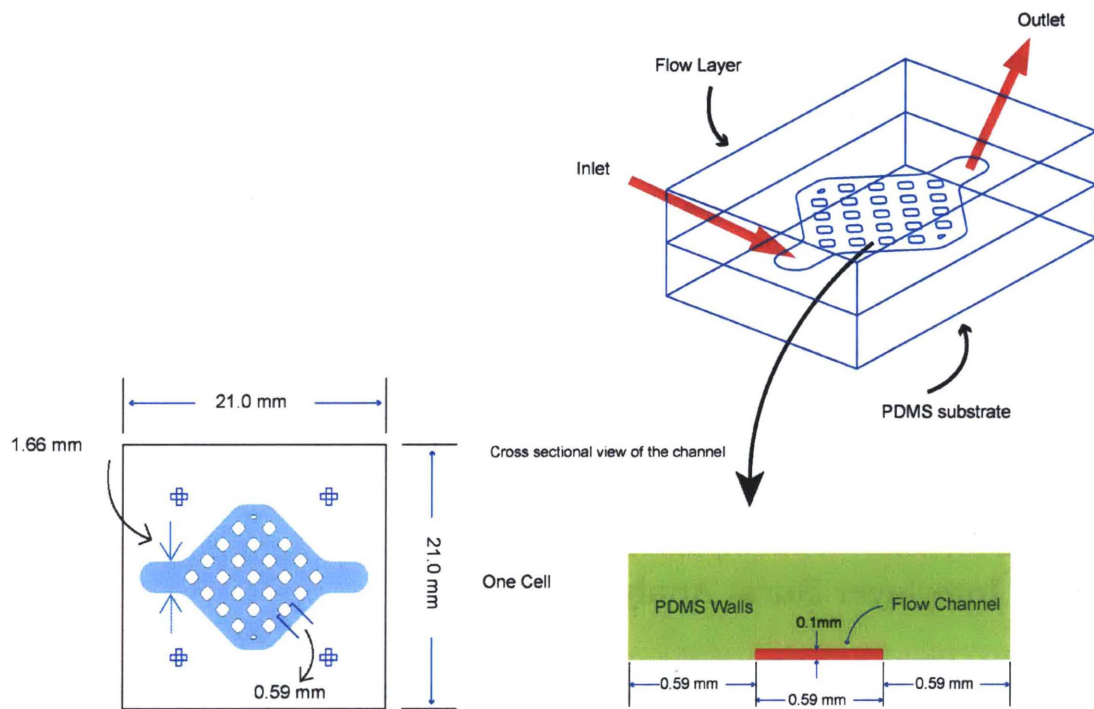
Figure 3. 6 Schematic diagram of the burst test device. Left: Top view of the device. Right: Three dimensional description of the device with cross-sectional view.
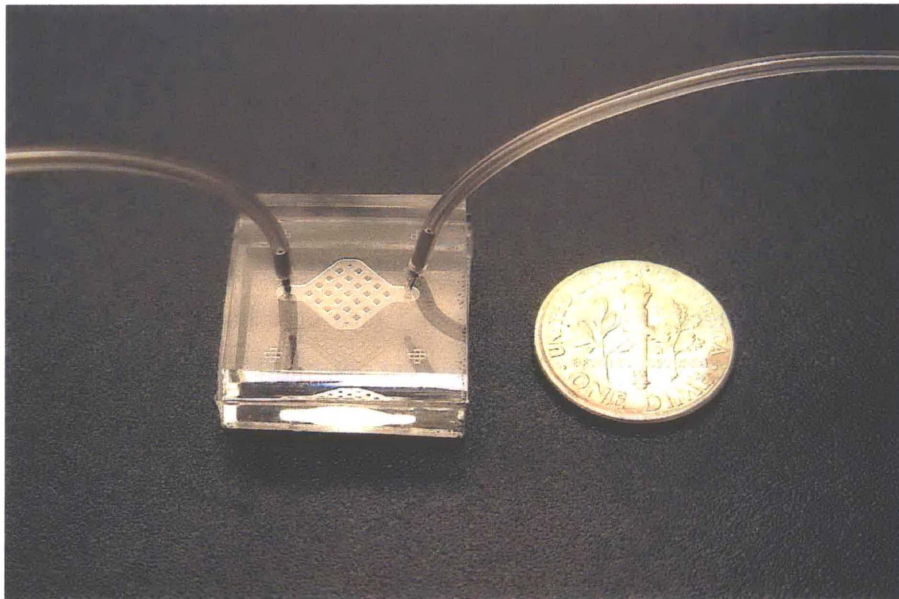
Figure 3. 7 Description of the burst test device

3.3.2 Experimental and Results

Interlayer burst mode was observed by directly blowing nitrogen gas through the microchannels. The applied pressure was varied from 0 up to approximately 50 psi until the channel burst activity was observed. Layer-layer adhesion failure was easily confirmed by the popping sound which occurred when the sealed channels burst. Interlayer failure was subsequently visually confirmed without any difficulty Test samples were prepared using the same parameters as shear and normal stress test except the device dimensions fixed. Apparently, the burst of interlayer bonding occurred around the microchannels centered in the PDMS device.

This test produced the most reliable results in characterizing the layer-layer adhesion property. The observed pressure values for samples with distinct sets of parameters were consistent with one another to a great extent. The bond strength increased from the 1:6/1:15 device to the 1:3/1:30 device for samples with fixed secondary curing time. Under the constant catalyst/monomer ratios, the strength of layer-layer adhesion of samples with 14 hour secondary bake was higher that those of 3 hour bake.

Additional test with fluid was conducted as well and the result for the burst pressure was in good agreement with the gas driven burst case. Figure 3.8 illustrates the distribution of the burst pressure for different combination of parameters and table 3.3 shows the maximum values at each of these combinations.
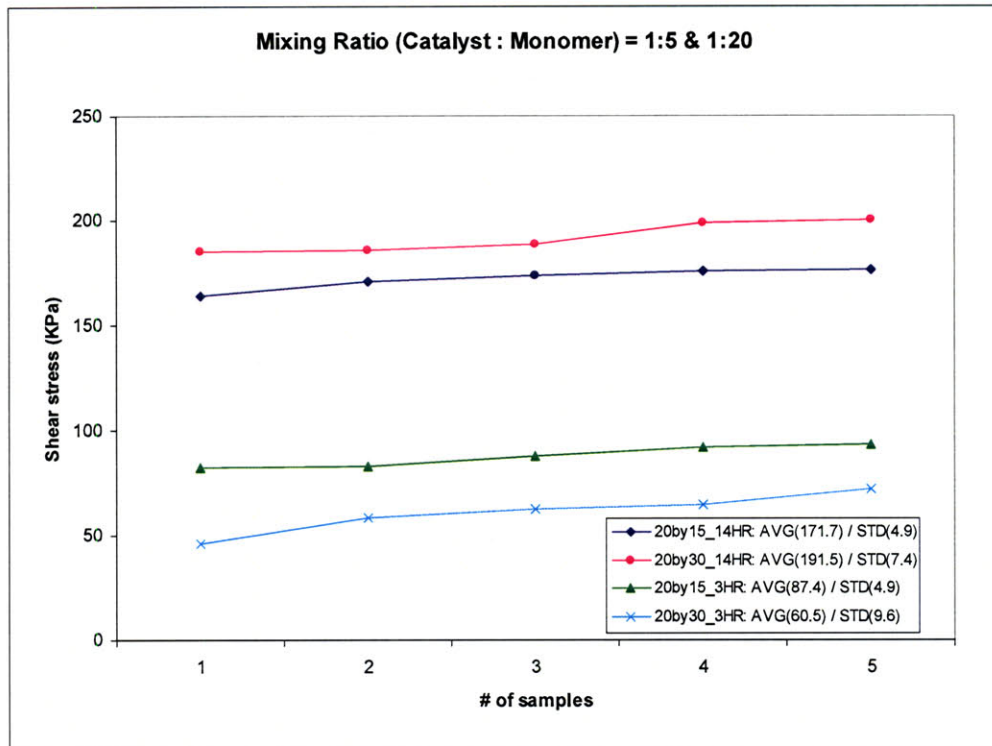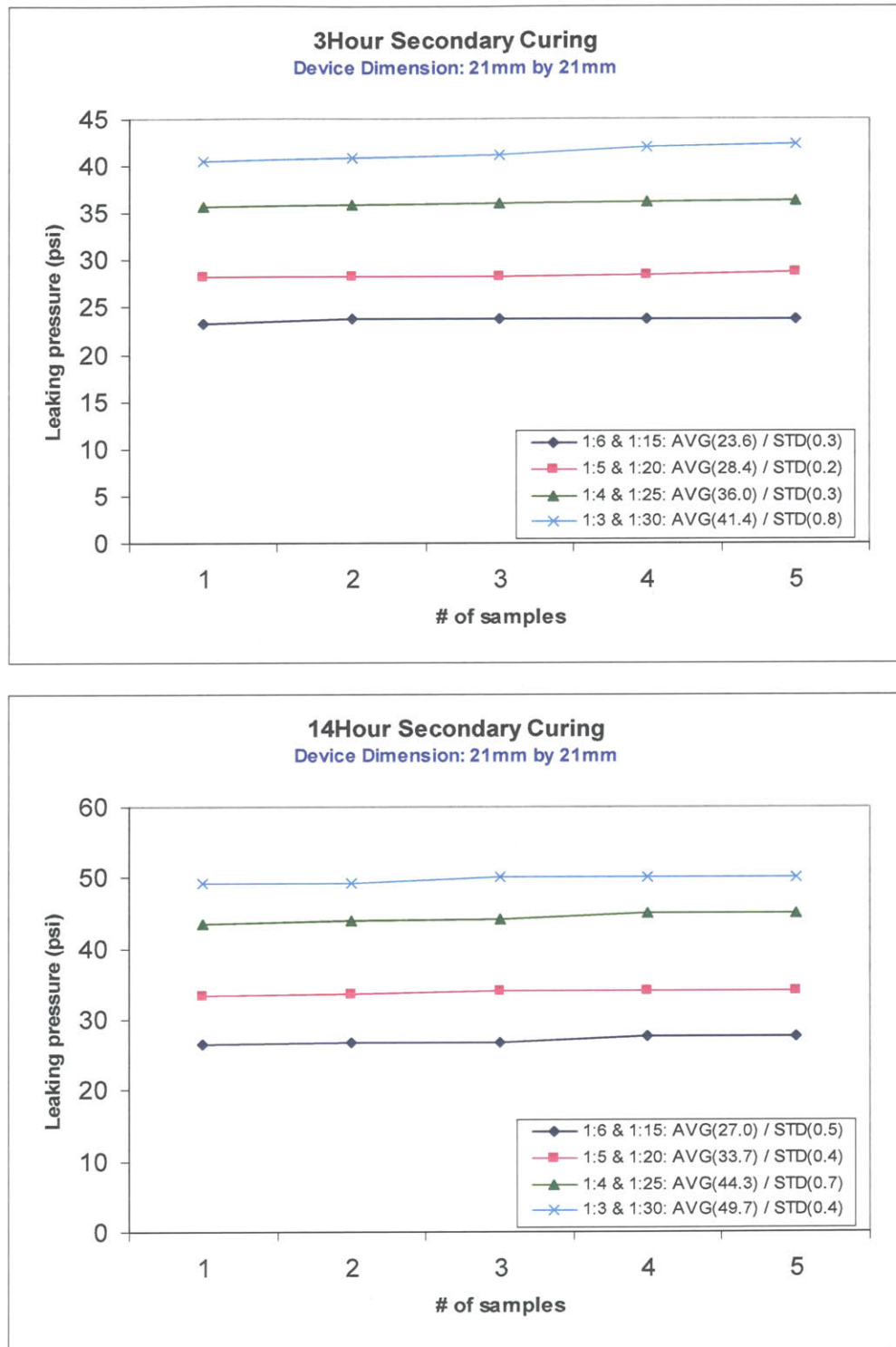
Figure 3. 8 Distribution of the applied pressures required to burst the microchannels at the interface between the top and bottom layer of PDMS.
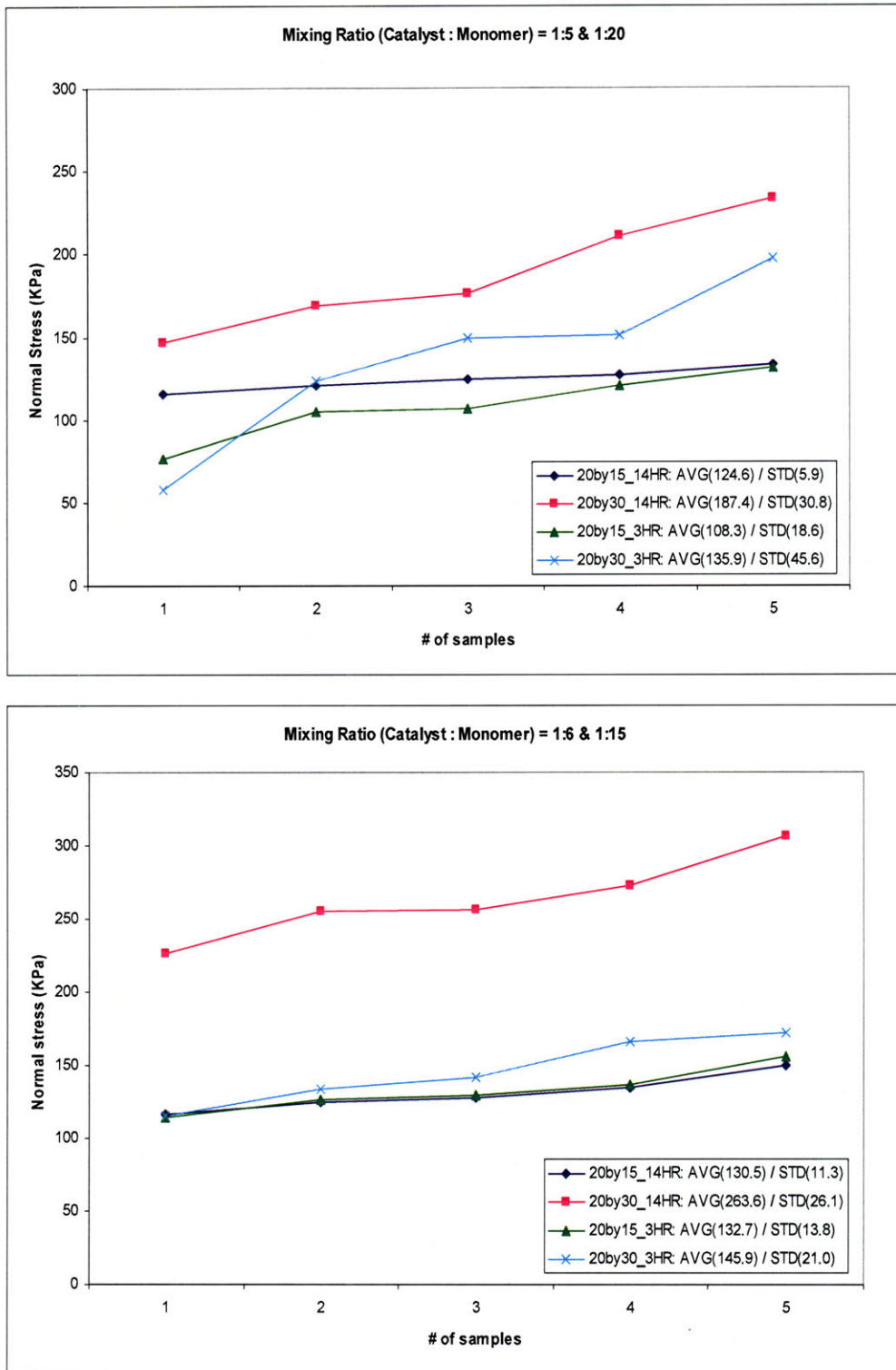
Pressure (psi)	1:3 / 1:30	1:4 / 1:25	1:5 / 1:20	1:6 / 1:15
3 hour	42.4	36.4	28.7	23.8
14 hour	50.1	45.0	34.0	27.5

Table 3. 3 Maximum values of the burst pressure for each combination of parameters.

Pressure (psi)	1:3 / 1:30	1:4 / 1:25	1:5 / 1:20	1:6 / 1:15
3 hour	42.5	36.0	27.0	23.5
14 hour	50.0	45.0	32.0	27.5

Table 3. 4 Burst pressures for liquid.

3.4 Conclusion

Multilayer microfluidic devices that are thermally bonded form a strong covalent bonding which provides enough sealing upon the exposure of external pressure in most of the practical application. This chapter investigated the interlayer bonding chemistry and mechanics of double layer elastomeric PDMS devices by varying several parameters, such as catalyst/monomer ratios, secondary curing time while fixing the primary curing time for each of different sets of catalyst/monomer ratio, and interlayer surface area. Three types of mechanical analysis, shear and normal stress, and interlayer burst activity, were performed on test devices with different combinations of parameters. All three tests yielded similar and reproducible results. As the catalyst/monomer ratio increases further away from the ideal mixing ratio of 1:10, the adhesion strength between the layers increased accordingly. Furthermore, increasing secondary curing time and the interlayer surface area seemed to enhance the bonding strength as well although the effect of

interlayer surface area did not seem to be as critical as that of catalyst/monomer ratio and secondary curing time.

Chapter 4

Surface Modification of PDMS Elastomers

While silicone rubber (PDMS) is easy to mold and has superior optical clarity, its hydrophobic surface makes it susceptible to non-specific protein adhesion and other hydrophobic species, a particular concern for microfluidic devices to be used in biological assays. Furthermore, hydrophobic channels are difficult to wet with aqueous solutions and easily nucleate bubbles inside the channel. Both chemical and physical modifications of the PDMS surface can increase its biocompatibility, rendering the surface hydrophilic or entropically unfavorable for protein adhesion. These procedures include oxygen plasma treatment, polymer coating or grafting, and chemical treatments with strong acids. In this section, we compared the efficacy of the several surface treatment methods by using fluorescently tagged bacteria (*E. coli*) flowed through microchannels as reporter particles to measure non-specific adhesion.

4.1   Device Description

Microchannels were fabricated from PDMS using soft-lithography and the mold was prepared from SU8-50 negative photoresist. The channels were 50 μm wide and 40 μm high. Once the PDMS device has been fabricated, it was thermally bonded to the cover slip that has been spun coated with PDMS to 20 μm thickness at 4200 rpm. The cover slip needed to be coated with PDMS so that all the channel walls were surrounded by PDMS.
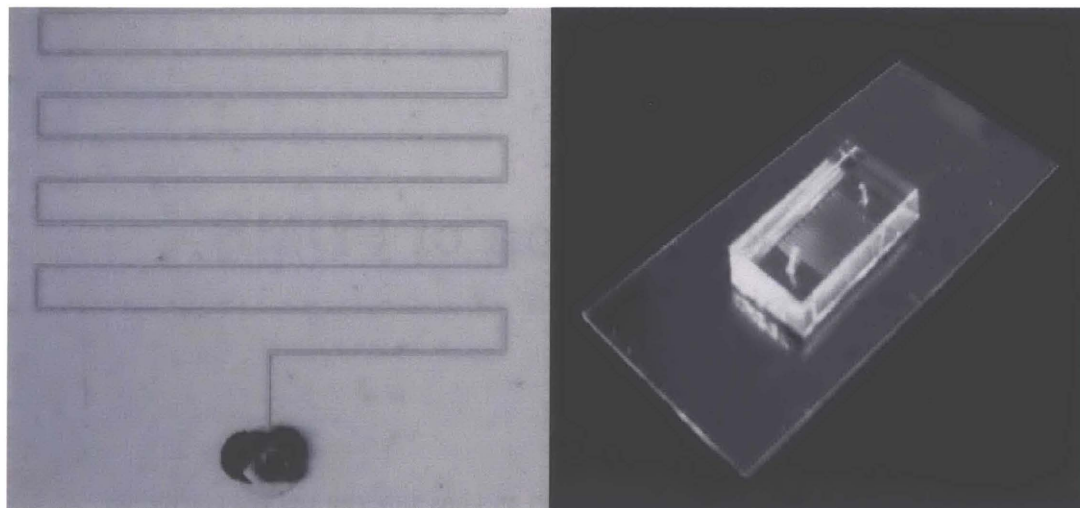
Figure 4. 1 Diagram of the surface modification test device. Microchannels are 6 mm long, 50 µm wide, and 40 µm high.

4.2   *E. Coli* Preparation

Medium (ATCC medium: #294 Broth) A mixture of 0.8g of Tryptone (BD 211705), 0.05g of NaCl, and 100ml of DI water was prepared and autoclaved at 121°C for 30 min.

E. Coli (Escherichia coli ATCC® 10798™) The entire pellet of *E. coli* was mixed with 6 ml of the medium and cultured at 37°C for 24 hours at 170 rpm. *E. coli* solution was then stained with the blue fluorescent DAPI nucleic acid stain (excitation / emission maxima: 358 / 461 nm, Invitrogen) at 1:1 volumetric ratio in order to observe and count individual *E. coli* particles under the fluorescent microscope.

4.3   Oxygen Plasma

PDMS has repeating units of $-O-Si(CH_3)_2$-groups and this chemical structure leads to a hydrophobic surface. Exposing PDMS surface to air or oxygen plasma introduces silanol groups (Si-OH) at the expense of methyl groups (Si-CH$_3$) on the surface and changes the surface property from hydrophobic to hydrophilic due to the presence of silanol groups,

whereas unmodified PDMS surface is hydrophobic and thus difficult to wet the surface with aqueous solutions and susceptible to other hydrophobic species.[43-45] Channels that have been treated with plasma can be kept hydrophilic indefinitely by keeping the surfaces in contact with water or polar organic solvents; otherwise surface rearrangements may occur over time that bring new hydrophobic groups to the surface to lower the surface free energy.[46]

Furthermore, oxidization using plasma produces silanol groups on PDMS and −OH-containing functional groups on the other materials. These polar groups form covalent −O-Si-O-bonds with oxidized PDMS when these surfaces are brought into conformal contact.[47] For PDMS and glass, this reaction yields Si-O-Si bonds after loss of water; These covalent bonds form the basis of a tight, irreversible seal.[46, 48,-49]

4.3.1 Methods

For the plasma experiment, the PDMS device and the substrate were not thermally bonded. Instead, each part was exposed to the oxygen plasma for 30 seconds at 100 Watt (SPI Plasma-Prep II) and brought into conformal contact forming an irreversible bonding.

4.4   Ultra-Violet Graft Polymerization

In this section, a one-step procedure to covalently link polymers to the surface of PDMS microchannels by ultraviolet graft polymerization was utilized. Two materials, acrylic acid and 2(dimethylamino)ethyl methacrylate (DMAEMA), were used to graft onto PDMS to yield hydrophilic surfaces. Graft polymerization involves creation of reactive sites (radicals) on the polymer surface followed by covalent linkage of a preformed polymer or more commonly a monomer that can then be used as the initiation site for a polymeric chain. Radicals on a previously inert polymer surface can be created by various methods such as application of chemical reagents or by exposure to ionizing radiation or ultraviolet (UV) light. In particular, UV graft polymerization is getting more

attention over the other methods since it involves fewer steps and possesses low or no penetration into the bulk polymer.[42, 47-50]

4.4.1 Materials

Acrylic acid (Fluka)

DMAEMA (2(dimethylamino)ethyl methacrylate, Aldrich)

NaIO$_4$ (sodium (meta)periodate, Sigma)

Benzyl Alcohol (Aldrich)

Photoinitiator (Irgacure 500, mixture of benzophenone and 1-Hydroxycyclohexyl phenyl ketone, Ciba)

4.4.2 Methods

Surface graft polymerization was carried out by the method reported in the using the protocol of E. Uchida et al.[51] First off, an aqueous solution containing NaIO$_4$ (0.5mM), benzyl alcohol (0.5 wt %) was prepared. Then, each monomer of Acrylic acid (10 wt %) and DMAEMA (1 wt %) were added to this solution. Each mixture was thoroughly mixed using magnetic stir bar for two hours. Inclusion of benzyl alcohol in the monomer solution have been reported to substantially increase the efficiency of surface grafting.[52-53] Microchannels were filled with the final mixtures and exposed to UV (Electrolite, ELC-500, 9W×4) for 30 min. After the irradiation, the channels were flushed with deionized (DI) water via syringe pump at the flow rate of 2 μl/min for 2hours to remove residual surface homopolymer. *E. coil* solution was perfused via syringe pump at the flow rate of 1 μl/min for 1 and 3 hours after 1 and 48 hours of surface modification. Then, the channels were flushed with DI water via syringe pump at the flow rate of 5 μl/min for 30 min.

4.5   Non-UV based Graft Polymerization

Non UV-based polyethylene glycol (PEG) grafts were used to modify the surface of PDMS using the protocol of S. Hu et al.[54] Instead of UV light, PDMS polymerizes as SiH groups react with vinyl groups in the presence of a Pt catalyst.[55]

4.5.1 Materials

Pt catalyst (chloroplantinic acid, Aldrich)

DAPEG (diacrylated polyethylene glycol SR610, Sartomer)

4.5.2 Methods

A mixture of DAPEG and Pt catalyst was prepared at the volumetric ration of 200:1. The mixture was thoroughly mixed using magnetic stir bar for 2 hours. This mixed solution was then fed into the syringe and the microchannels were completely filled with. Next, the PDMS device filled with mixture of DAPEG and Pt catalyst was baked in the conventional oven at 80°C for 30 min. Finally, the DAPEG mixture was flushed out of the device with DI water via syringe pump (Harvard, MA) at the flow rate of 5 μl/min for 2 hours to completely remove any residual of the mixture. E. coli solution was flowed through the channels via syringe pump at the flow rate of 1 μl/min for 1 and 3 hours after 1 and 48 hours after the preparation of the test device. After the channels were exposed to E. coli, they were flushed with DI water via syringe pump at the flow rate of 5 μl/min for 30 min.

4.6   Results

Four different sets of experiment with four different surface modification methods were investigated; E. coli was continuously flowed for one and three hours after one and forty-eight hours of surface treatment. After E. coli was perfused inside the channel, photos of

the microchannels were recorded (XCD-V50, SONY) and additional photos were taken after *E. coli* was flushed with DI water (Figures 4.2 and 4.3). Figure 4.2 shows images of the microchannels after *E.coli* was flowed at the flow rate of 1μl/min (A-1, B-1, and C-1) and then flushed with DI water (A-2, B-2, and C-2) at 5 μl/min. Channels A and B are untreated while channel C has been treated with acrylic acid. *E. coli* has been stained (dye) in channels B and C. One of the most well-known defects of PDMS, non-specific protein adhesion on the surface, is observed in B-2. Although the channels were flushed with DI water for 30 minutes, most of the *E. coli* particles were still adherent inside the channel. However, once the channel was treated with acrylic acid, great improvements on non-specific adhesion was observed (C-2). The other three methods also improved the channel fouling to different degrees.
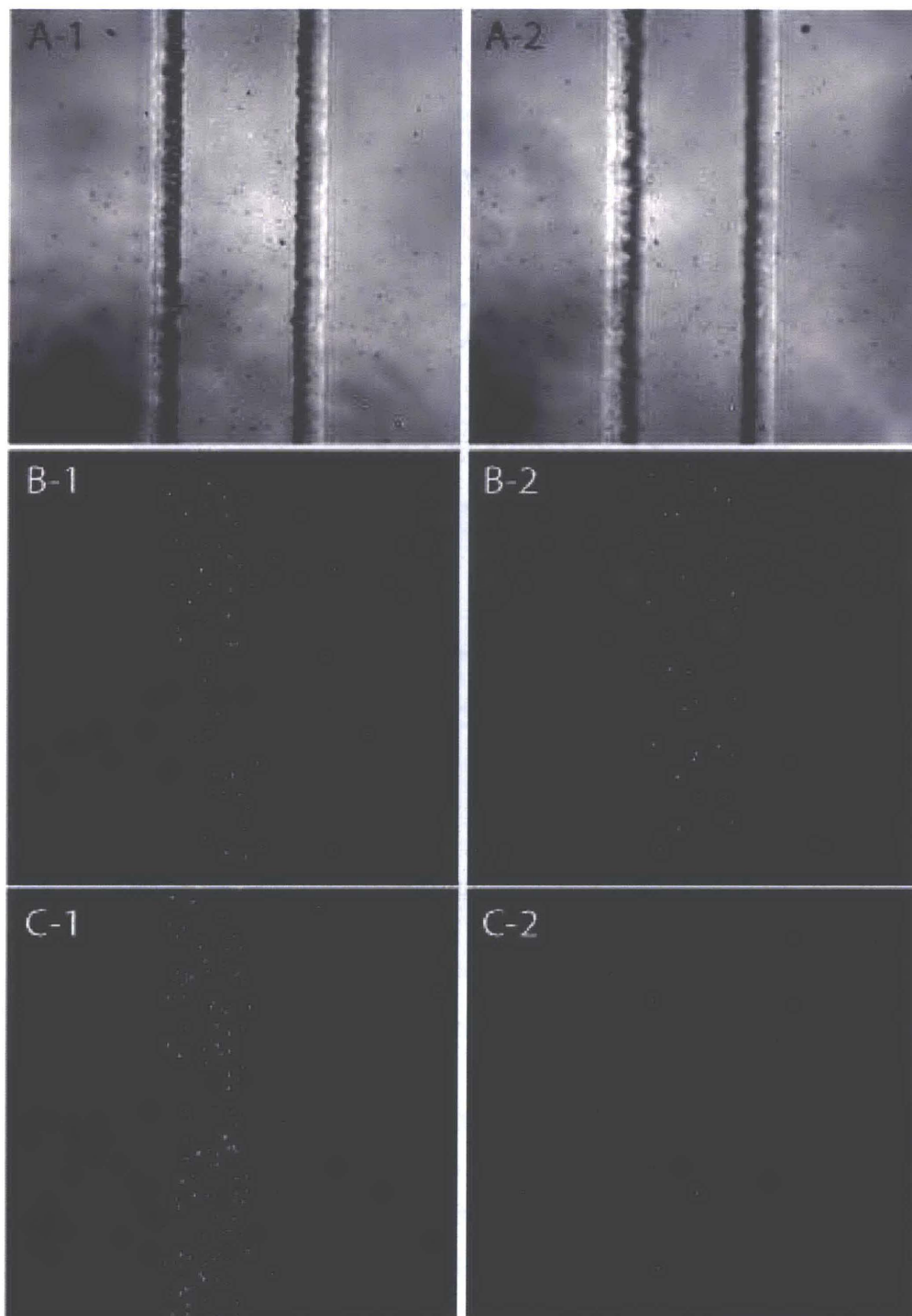
Figure 4. 2 Photos of channels before and after the channels were flushed with DI water after E. coli was flown through the channel. White dots in pictures B and C indicate fluorescently tagged E. coli 1: After E. coli flow 2: After flushed with DI water A: Non treated channels without fluorescently tagged E. coli B: Non treated channels with fluorescently tagged E. coli C: Channels treated with Acrylic acid
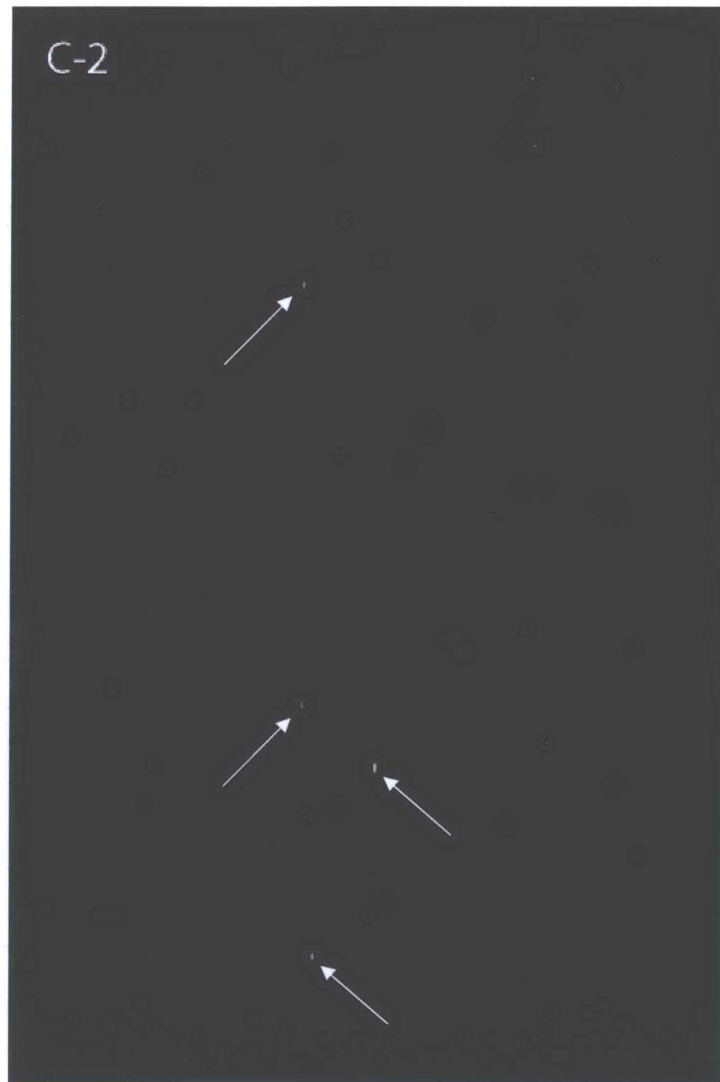
Figure 4. 3 Magnified image of C-2 from Figure 4.2

To assess treatment efficacv, the number of *E. coli* particles before and after the DI-water-flush were counted in the image captures of the microchannels . The actual counts of the *E. coli* particles from four different surface treatments are summarized in Tables 4.1 to 4.5 and visualized with bar graphs in Figures 4.4 to 4.7. The efficacy of these four different methods on the degree of *E. coli* adhesion inside the channel was evaluated and compared to the untreated control channels.

Control / # of E. Coli	1 hour run		3 hours run	
	Before	After	Before	After
Trial_1	119.0	30.0	120.0	44.0
Trial_2	104.0	38.0	127.0	46.0
Trial_3	108.0	32.0	118.0	45.0
Trial_4	120.0	34.0	124.0	53.0
Trial_5	101.0	36.0	134.0	52.0
Average	110.4	34.0	124.6	48.0
Standard Deviation	8.7	3.2	6.3	4.2

Table 4. 1 Control: Number of E. coli inside the channel before and after channels were flushed with DI water after E. coli was perfused.

Acrylic Acid / # of E. Coli	1 hour after				48 hours after			
	1 hour run		3 hours run		1 hour run		3 hours run	
	Before	After	Before	After	Before	After	Before	After
Trial_1	98.0	3.0	134.0	5.0	124.0	12.0	116.0	4.0
Trial_2	111.0	4.0	128.0	5.0	128.0	7.0	109.0	5.0
Trial_3	115.0	3.0	117.0	4.0	123.0	5.0	123.0	4.0
Trial_4	131.0	4.0	128.0	4.0	121.0	6.0	111.0	5.0
Trial_5	121.0	6.0	121.0	5.0	122.0	8.0	108.0	5.0
Average	115.2	4	125.6	4.6	123.6	7.6	113.4	4.6
Standard Deviation	12.21	1.22	6.7	0.6	2.7	2.7	6.2	0.6

Table 4. 2 Acrylic acid: Number of E. coli inside the channel before and after channels were flushed with DI water after E. coli was perfused.

Oxygen Plasma / # of E. Coli	1 hour after				48 hours after			
	1 hour run		3 hours run		1 hour run		3 hours run	
	Before	After	Before	After	Before	After	Before	After
Trial_1	111.0	6.0	108.0	10.0	107.0	4.0	111.0	9.0
Trial_2	126.0	3.0	115.0	10.0	111.0	5.0	100.0	10.0
Trial_3	115.0	5.0	100.0	9.0	95.0	7.0	102.0	7.0
Trial_4	99.0	3.0	94.0	8.0	104.0	6.0	105.0	13.0
Trial_5	110.0	3.0	103.0	7.0	123.0	5.0	112.0	10.0
Average	112.2	4.0	104.0	8.8	108.0	5.0	106.0	9.8
Standard Deviation	9.7	1.4	8.0	1.3	10.3	1.1	5.3	2.2

Table 4. 3 Oxygen Plasma: Number of E. coli inside the channel before and after channels were flushed with DI water after E. coli was perfused.

DAPEG / # of E. Coli	1 hour after				48 hours after			
	1 hour run		3 hours run		1 hour run		3 hours run	
	Before	After	Before	After	Before	After	Before	After
Trial_1	112.0	2.0	108.0	2.0	147.0	17.0	105.0	12.0
Trial_2	123.0	4.0	103.0	4.0	125.0	12.0	102.0	13.0
Trial_3	126.0	3.0	117.0	3.0	137.0	16.0	100.0	13.0
Trial_4	119.0	2.0	117.0	2.0	132.0	16.0	94.0	11.0
Trial_5	134.0	2.0	106.0	3.0	140.0	19.0	96.0	14.0
Average	122.8	2.6	110.2	2.8	136.2	16.0	99.4	12.6
Standard Deviation	8.2	0.9	6.5	0.8	8.3	2.6	4.5	1.1

Table 4. 4 DAPEG: Number of E. coli inside the channel before and after channels were flushed with DI water after E. coli was perfused.

DMAEMA / # of E. Coli	1 hour after				48 hours after			
	1 hour run		3 hours run		1 hour run		3 hours run	
	Before	After	Before	After	Before	After	Before	After
Trial_1	138.0	7.0	84.0	4.0	119.0	23.0	103.0	11.0
Trial_2	147.0	5.0	94.0	4.0	103.0	26.0	108.0	11.0
Trial_3	123.0	6.0	107.0	3.0	127.0	21.0	91.0	12.0
Trial_4	132.0	7.0	110.0	4.0	111.0	31.0	90.0	12.0
Trial_5	124.0	5.0	98.0	4.0	111.0	28.0	100.0	13.0
Average	132.8	6.0	98.6	3.8	114.2	25.8	98.4	11.8
Standard Deviation	10.0	1.0	10.4	0.5	9.1	4.0	7.8	0.8

Table 4. 5 DMAEMA: Number of E. coli inside the channel before and after channels were flushed with DI water after E. coli was perfused.
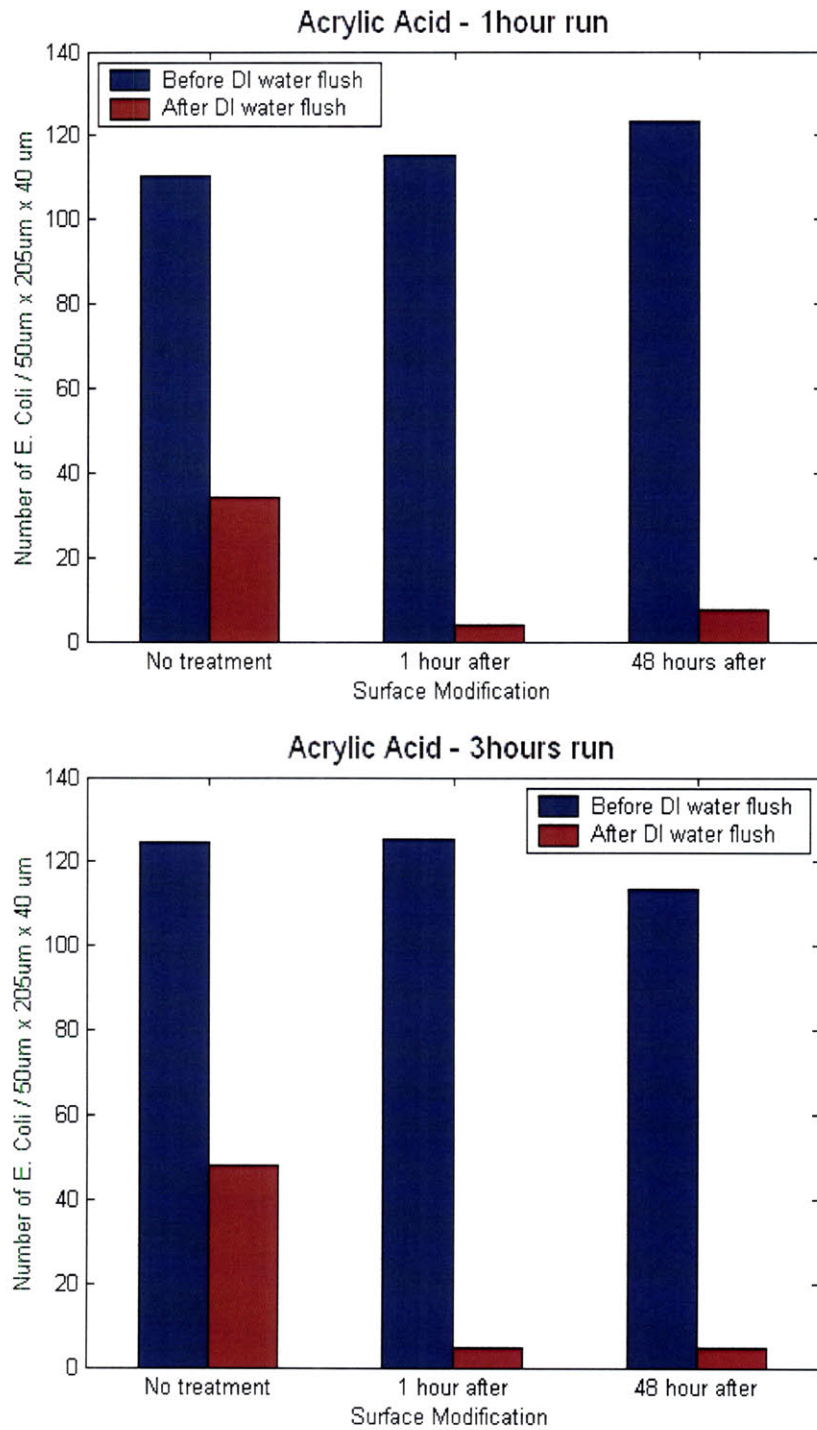
Figure 4. 4 Number of E. coli inside the channel treated with Acrylic acid before and after the channels were flushed with DI water Top: 1 hour flow Bottom: 3 hours flow
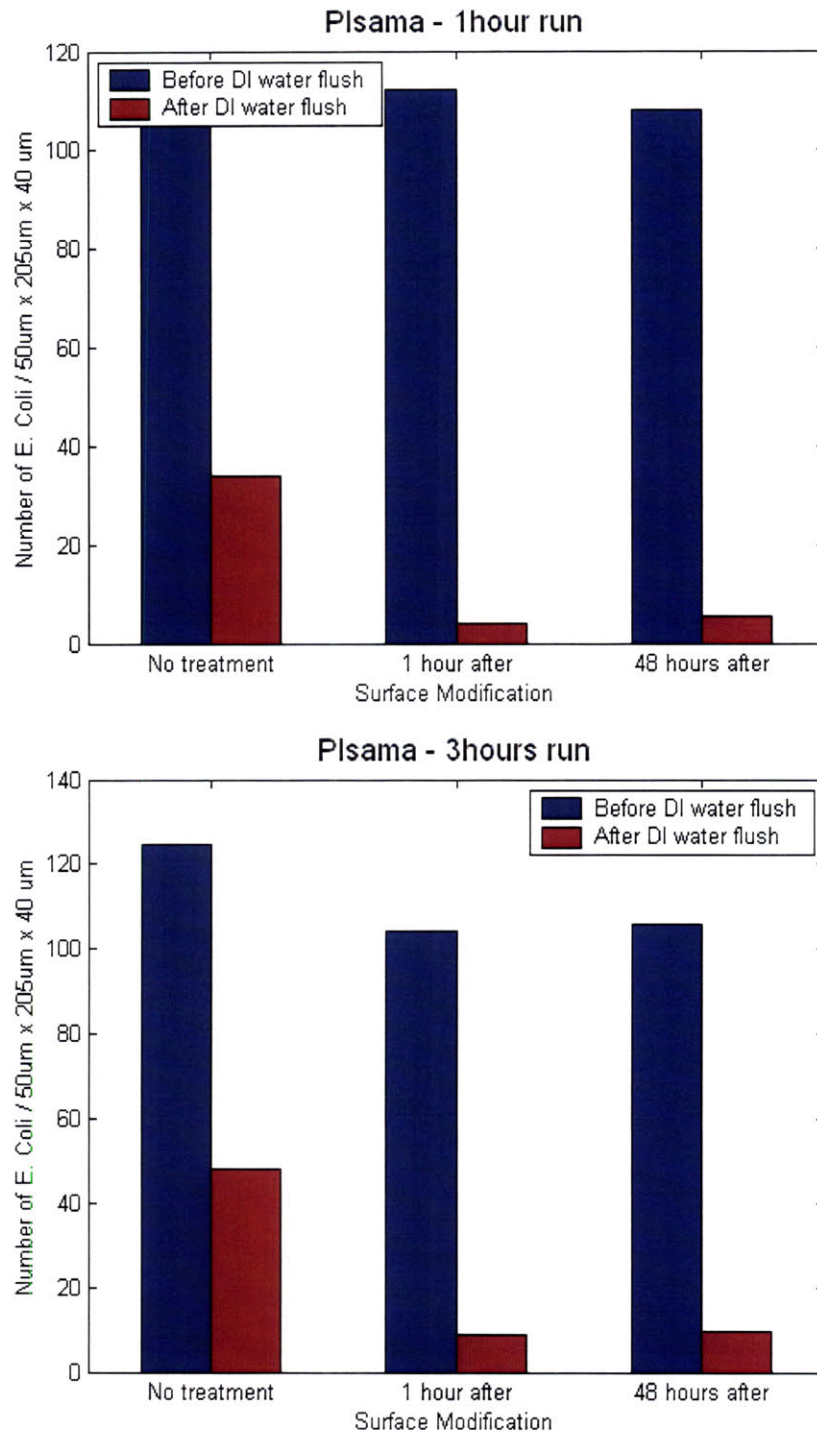
Figure 4. 5 Number of E. coli inside the channel treated with Oxygen Plasma before and after
the channels were flushed with DI water Top: 1 hour flow Bottom: 3 hours flow
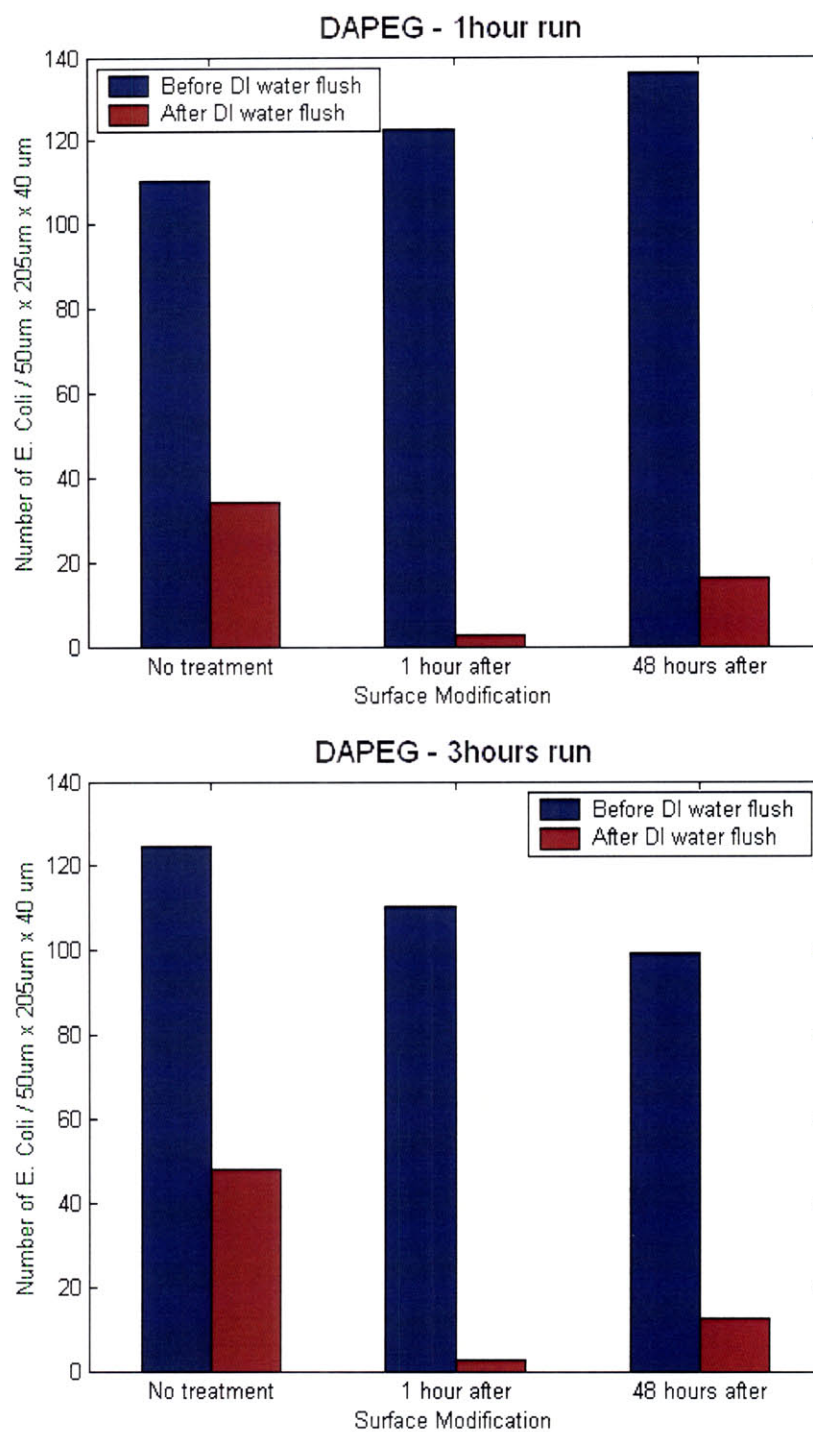
Figure 4. 6 Number of E. coli inside the channel treated with DAPEG before and after the channels were flushed with DI water Top: 1 hour flow Bottom: 3 hours flow
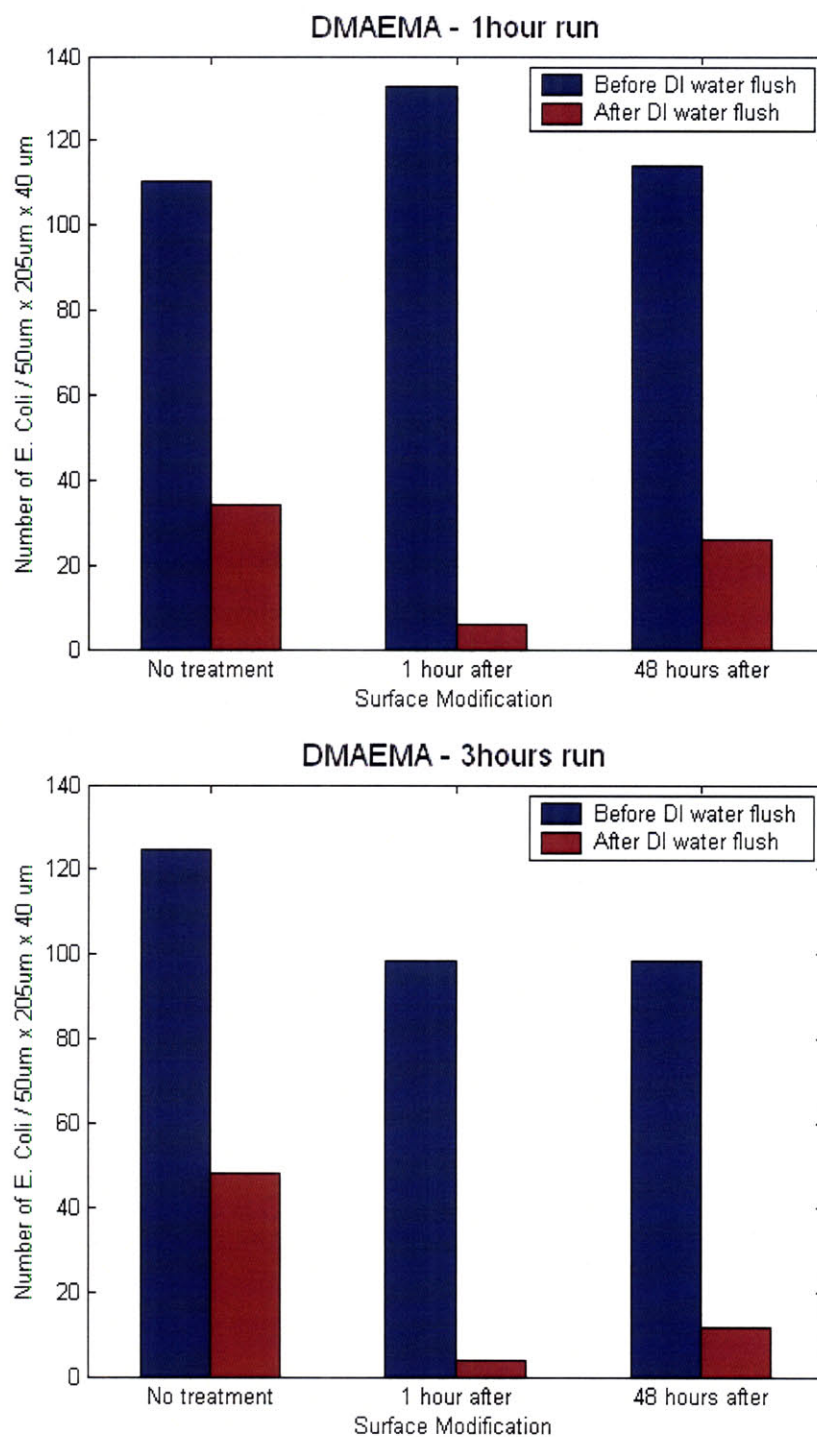
Figure 4. 7 Number of E. coli inside the channel treated with DAMEMA before and after the channels were flushed with DI water Top: 1 hour flow Bottom: 3 hours flow

From the data, it can be observed that the anti-biofouling efficacy of each treatment degrades with time. Furthermore, the run time of *E. coli* solution had a minimal affect on the degree of biofouling; the results from 1 hour and 3 hours running showed not much of a variation from each other. In comparing the efficacy of the four different surface treatments, it was observed that acrylic acid was the most effective in improving the non-specific adhesion on PDMS surface followed by plasma, DAPEG, and DMAEMA..

4.7 Conclusion

Despite the numerous advantages of PDMS for microfluidic devices (such as rapid prototyping, optical clarity, and gas permeabiity), PDMS elastomers suffer from non-specific protein adhesion which raises a particular concern for devices to be used in biological assays due to its hydrophobic surface profile. However, several approaches in regard to improve the non-specific adhesion have been attempted and some simple yet effective methods were introduced in this chapter. The efficacy of suggested methods was investigated by studying the effects of aging of the surface treatment and flow duration of target solution on the surface-treated microchannels.

Chapter 5

Development of Artificial Respiration Device

Most current artificial lung technologies require the delivery of oxygen gas into the blood via permeable hollow fibers, which depends on membrane diffusivity and differential pressure to drive gas exchange. In this chapter, we introduce an alternative approach in which dissolved oxygen (DO) is generated directly from the water content of blood through the interaction of UV light with a semi-conducting titanium dioxide thin film. The driving force for this reaction is the displacement of electrons at the photoactive surface following photon absorption. The resulting generation of electron holes promotes the oxidation of adjacent water molecules to form active oxygen (AO), which then decomposes into DO.

5.1   Oxygenation: Theory

The fundamental technology in this so called active oxygenation system lies in the interaction between the semi-conducting metallic oxide, TiO_2 photolytic thin film, and water contents present in blood via photolytic energy. As one side of the TiO_2 film is exposed to the light source, the other side of the film (porous film) in contact with blood generates DO by the following cascade chemical reactions. The following equations comprise the basis for the photolytic conversion of water into DO and the generation of carbon dioxide (CO_2). [56]

Reaction 1. Photolysis yielding charge separation and active oxygen:

$$hv + TiO_2(anatase) \rightarrow AO + 2e^-_{(scb)}$$
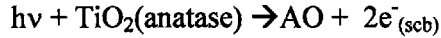
where AO designates a solid state active form of oxygen, for example the peroxo "$[TiO_2(O_2^=)^{2+}]$" species occurring in the bulk solid phase of the photocatalyst film. The quotations indicate a surrogate formula for the transient photo-activated catalyst site within the TiO_2 film where the photon was absorbed (i.e. the "hole" or h^+) or any locations within the solid to where the "hole" has migrated via electron exchange other than the surface. "scb" indicates that the electron produced upon photon absorption is energetically transferred into the semiconductor band of the titania crystal. As shown below, AO has a very short life once it migrates to the surface of the photocatalyst that is in contact with the water supplied from the blood plasma. This migration step reforms the photon absorption bulk titania film site as follows.

Reaction 2. AO migration to the thin film surface and hydration to adsorbed peroxy species:

$$[TiO_2(O_2^=)^{2+}]_{(bulk)} + 2[TiO_2\text{—}OH_2]_{(surf)} \rightarrow 2[TiO_2\text{—}OOH]_{(surf)} + 2H^+_{(aq)} + [TiO_2]_{(bulk)}$$
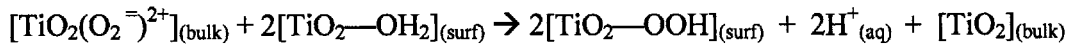
The H_2O present on the DO generating surface is supplied from the bulk aqueous phase (nominally 55.5 molar) and thus does not represent a significant diffusion boundary layer. Theoretically, water diffusion rate constraints would be expected only at very high lamp intensities and the highest DO flux values, a limitation not expected for the proposed technology based on current work. Once at the surface, DO is generated by spontaneous disproportionation in the following manner.

Reaction 3. Disproportionation

$$2[TiO_2\text{--}OOH]_{(surf)} \rightarrow 2[TiO_2\text{--}OH]_{(surf)} + DO$$
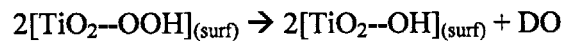
The hydrated surface titania species is regenerated at the same time where it is ready to undergo the next DO generation cycle. The DO diffuses out of the nanoporous surface at a flux proportional to the lamp intensity, the quantum yield, and the overall rate of reactions 1, 2 and 3. The DO migrates through the blood plasma where it is taken up rapidly by red blood cells (RBC) and hemoglobin.

Reaction 4. Oxygenation of hemoglobin

$$DO + Hb_{RBC} \longrightarrow O_2Hb_{RBC}$$
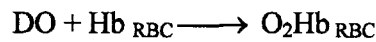
The hydrogen ions from Reaction 2 transfer through the aqueous phase by the well known "hopping" mechanism and react with the bicarbonate ion in the blood to enable the release of carbon dioxide (CO_2) in the manner already involved in the natural lung.

Reaction 5. CO_2 removal using physiological chemistry, involving protonation:

$$H^+ + HCO_3^- = H_2CO_3$$
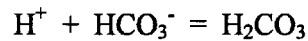
This reaction is followed rapidly by:

Reaction 6. Spontaneous catalyzed dehydration:

$$H_2CO_3 \xrightarrow{\text{CarbonicAnhydrase}} H_2O + CO_2\uparrow$$

The chemical substrate for DO formation is a small amount of water derived from the blood. The formation of DO within the TiO_2 ceramic nanoporosity prevents direct contact of blood cells to the DO formation region. The illumination region is only solid state and does not contact the aqueous or blood phases.

5.2   Concept validation

A macroscale test cell has already been constructed by *Dasse et al.* [13] to determine the extent to which the indicated chemical conversions occurred during UV illumination of active surface material. Figure 5.1 is a diagram of the flow cell constructed with the essential elements of design, a conductive coating of vacuum deposited titanium metal, a coating of adherent TiO_2 (anatase), and a MnO_2 particulate layer. Ultraviolet (UV) laser light was introduced to irradiate transparent quartz substrates. This cell was used to collect pH, electrical current, DO, and gas phase CO_2 data as a function of UV irradiation time with the intensity of 88.1 mW/cm^2 filtered at 365 nm wavelength.
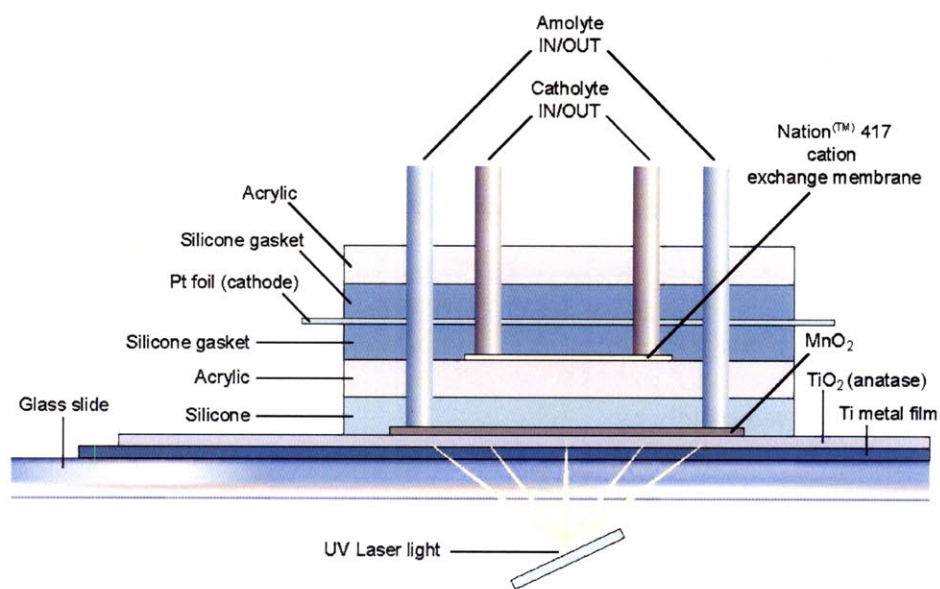
Figure 5. 1 Flow-through cell for DO generation and measurement. Schematic illustrating the individual elements of test cell construction. For purposes of clarity, film thicknesses are not drawn to scale. Shown are the configuration of the cell components, including photoactive films, light source, and inlet/outlet for both anolyte and catholyte.

5.2.1 Measurement of dissolved oxygen generation

A liquid phase reaction chamber was used to monitor DO production. This device uses a Clark Electrode to measure DO. A two-point calibration procedure was used to the DO sensor; 2.35 ml of air saturated water at 36°C (217.2 nmol/ml) was added to the cell, and measurements were taken. Then the cell was emptied and flushed with nitrogen to obtain a zero oxygen measurement. A blood substitute was then added to the batch cell at a volume of 2.35 ml and a temperature of 36°C. This blood substitute, commonly referred to as Lockes-Ringer Solution, contains 0.15 M NaCl, 5.6 mM KCl, 4.2 mM $CaCl_2*2H_2O$, and 7.1 mM $NaHCO_3$. Shortly after this addition, deoxygenation of the solution was performed by bubbling with nitrogen gas. Once the oxygen content dropped to minimal levels, the nitrogen bubbling was halted, the photoactive construct and Pt wire counter-electrode are added, and the reaction chamber is sealed. The process of removing the sparge tube and sealing the chamber allows some oxygen from the atmosphere to reenter the system. It takes some time for the oxygen concentration to equilibrate. Once this occurs, a bias voltage is applied to the cell to produce an electric field to promote immediate removal of photo-generated electrons but insufficient to produce electrochemical reactions. A DC power source is used to supply this constant potential to the system; a Pt wire is connected as the cathode, and the Cu wire extending from the photoactive construct, and not exposed to the test solution, is connected as the anode. Electrical current is measured with a high-impedance VOM multimeter. The UV source is directed to the reaction chamber and the light emitted from the pipe is filtered to produce light of only 365 nm; the intensity at this wavelength is 88.1 mW/cm^2. Heating of the solution during illumination was prevented by use of the water jacket surrounding the reaction chamber; water from a constant temperature circulating bath flowing through this jacket kept the system at a constant 36°C throughout the experiment. Furthermore, the light energy associated with activation by a 365 nm UV laser light selectively excites the TiO_2 semiconductor electronic transition (350 – 389 nm band, or about 3.2 eV) with minimal wasted radiation or transmission. Special dopants may adjust this wavelength to reduce the energy requirement and even to allow activation within the range of visible light.

5.2.2 Observations

The test cell described previously was able to verify that the chemical conversions occurred only during illumination and in association with the active surface material. The ability of the thin films of TiO_2 to impart energy into the anatase matrix and thereby to activate the sequence of chemical reactions described earlier was shown by several criteria.

The generation of active oxygen (AO) at the anatase surface using the energy from the UV light was evidenced by the disappearance of MB (methyl viologen) dye at the surface of the anatase film opposite the side irradiated by the UV laser. In turn, the generation of freed electrons at the anatase surface was evidenced by the appearance of MB blue color at the surface of the anatase, opposite the site of irradiation. Transport of the electrons to a conductive surface, where they are then removed so that they do not recombine with the active oxygen being produced, was evidenced by electrical current in the anatase semiconductor film to a metallic collector, wire, and amp meter. Electrical current was found to flow only when the laser was on and never when it was off. The effect was observed through many on/off cycles. By cycling the UV light, it was shown that the generation of oxygen only occurred when the cell was illuminated and not otherwise (Figure 5.2).
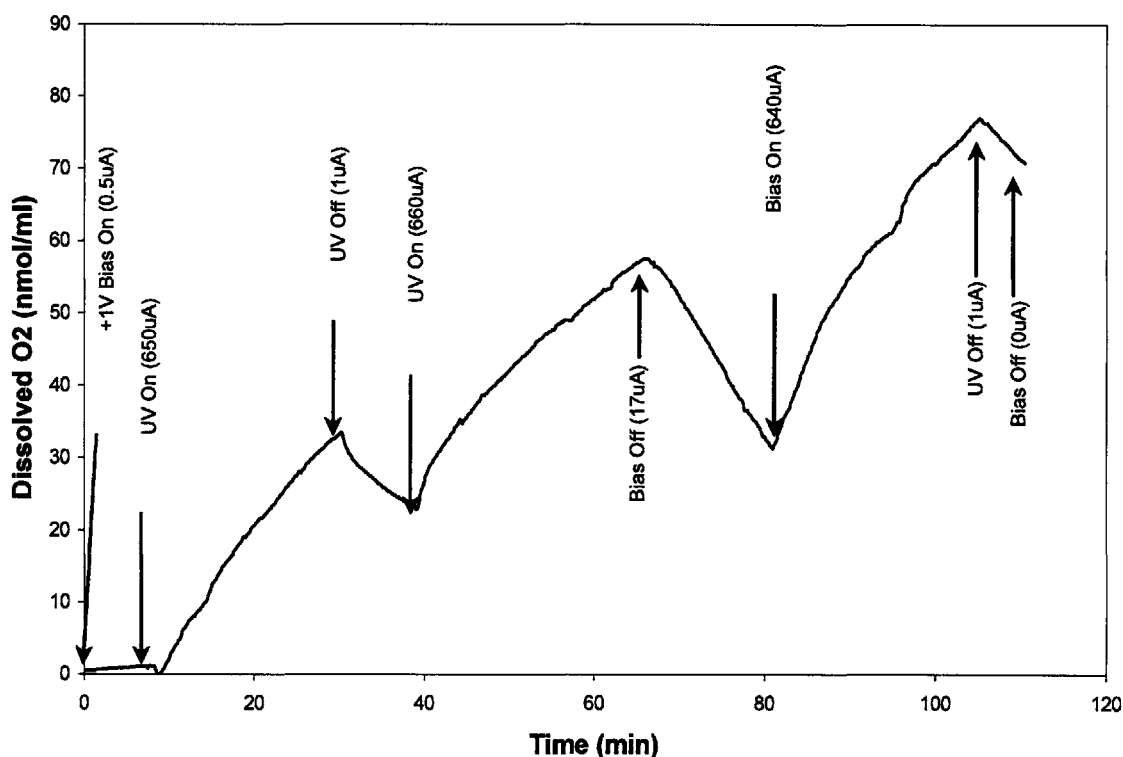
Figure 5. 2 Photolytic induction of dissolved oxygen (DO). Real time demonstration of DO production in a glass substrate (9 mm x 25 mm) containing 1230Å Ti and TiO₂ in 2.35ml of Locke's Solution (7.2 pH) at 36°C. Bias voltage of +1V was applied using photoactive construct as the anode and a Pt wire as the cathode, and UV light supplied.

As shown by the comparison of Figure 5.3, the presence of electrical potential between the conducting layer of the construct and a Pt. counter electrode during illumination produces an electric field across the photolytic layer, which forces electron flow away from the TiO₂ layer and results in enhanced DO production. When the bias voltage is removed, and the illumination with UV light ceases, the oxygen concentration decreases, and the current flow is observed to reverse for a short time. This reversal of current indicates that during illumination a charge accumulation occurs within the photolytic construct. Once the light source and bias voltage are turned off, electrons flow back into the semiconductor layer and oxygen is adsorbed.
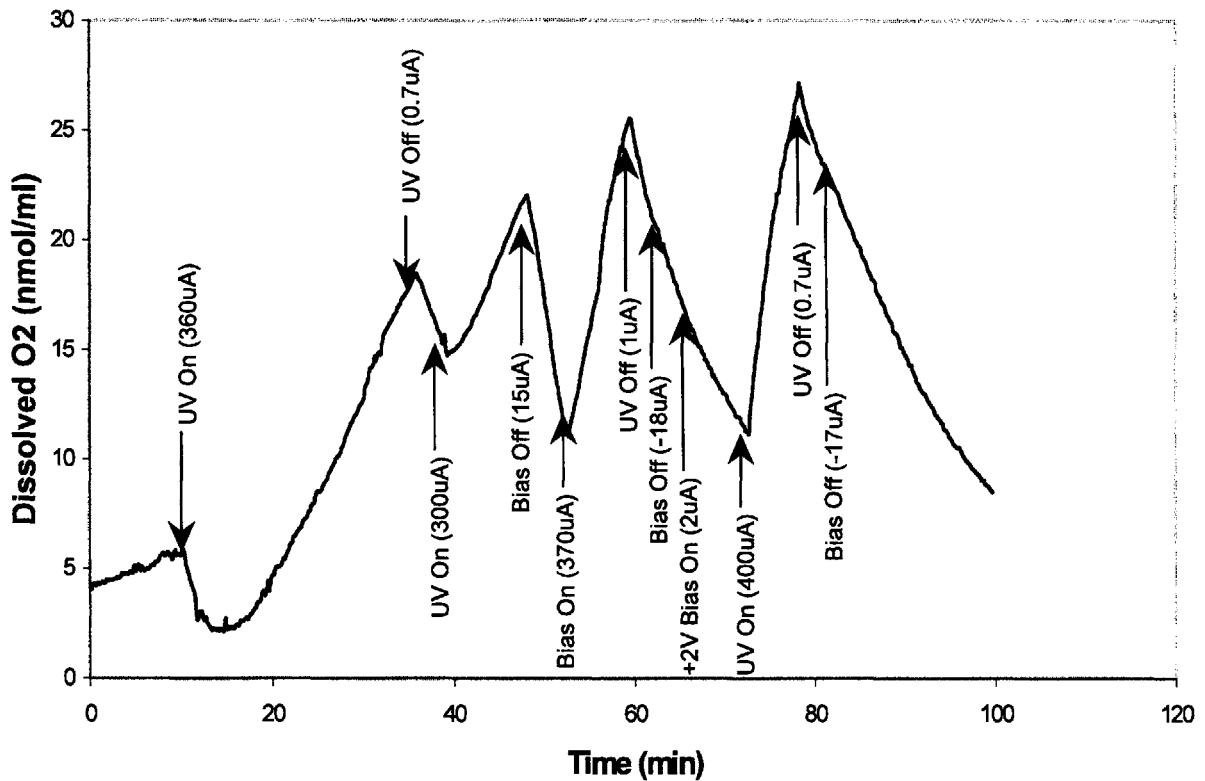
Figure 5. 3 Dependence of DO generation on the application of a bias voltage. Real time demonstration of DO production under the same conditions described in Figure 5.2, with the exception that bias voltage in the range of +1 to +2 V was applied.

5.3 Basic Design Elements for a microfluidic capillary network

Microfluidic blood flow devices with complex channel geometries employing high flow conditions may be associated with impaired hemocompatibility. Therefore, scaling up of these networks to accommodate physiologically relevant blood flow rates (L min^{-1}) is likely to be associated with increased diffusion length and requires through assessment of the channel geometry, flow rate, and their effects on hemocompatibility. We have previously examined in detail the relationships between microchannel geometry and configuration, flow and oxygen diffusion in a microcapillary device.[57-58] Acknowledging

the presence of relatively large viscous forces in most microfluidic devices, and the resulting effect on shear stress,[59-60] it has been previously suggested that blood flow microchannels embodying a branching network require a minimum diameter of 100 μm.[61] Although this channel diameter is considerably larger than native pulmonary capillaries (approximately 5 μm) this diameter is analogous to that of the branching pulmonary arterial system.[62-65] and thus may constitute a reasonable design template. Such a design represents a pragmatic compromise since it may itself introduce diffusive boundary layers not present in native pulmonary capillaries. The mass transfer properties of microcapillaries with similar diameter was previously characterized analytically through a simple convective mass transfer model.[67] accounting for the diffusivity of oxygen in blood and the channel diameter (in this case the channel height), and deriving the Peclet number as a measure of the ratio of the convective to diffusive mass transport both analytically and experimentally. These results confirmed that hemoglobin saturation is feasible assuming the above channel configurations and physiological flow lengths. However, preliminary hemocompatibility experiments to assay thrombogenesis by microscopic visualization for devices possessing a 100 μm X 100 μm channel diameter and a 90° branching configuration during flow (0.1 - 0.64 mL/min) of anticoagulated blood (ACT > 300 seconds) revealed thrombus at 25% of channel inlets/outlets and bifurcations as early as 20 minutes.[66] (Figure 5.4) As a result, we considered a series of channel configurations employing y-shaped bifurcations with the goal of minimizing reduced flow regions and thus reducing the rate of thrombus. The current design also employed the concept of y-shaped bifurcations, but specifically embodied several novel design elements described below.
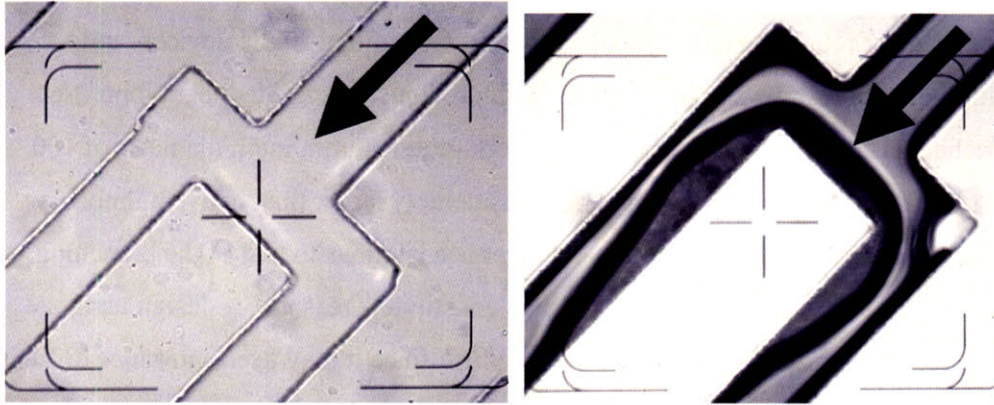
Figure 5. 4 Image of microchannel bifurcation before and after exposure to flowing blood. The image on the left shows a channel bifurcation prior to blood contact. The image on the right shows the same channel bifurcation after 20 minutes of blood flow (the flow rate was 20 µL/min in the inlet channel). The dark areas in the channel are thrombi and areas of reduced flow. The arrows indicate the direction of flow. The pattern of thrombus occurred in areas of flow separation and recirculation.[48]
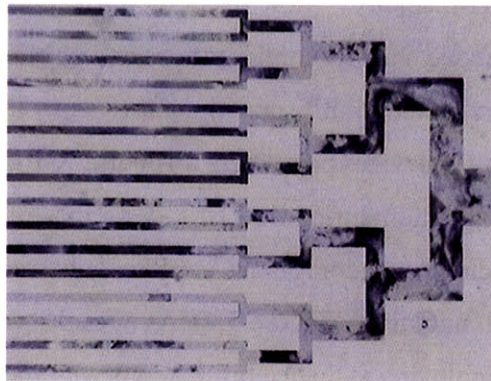
Figure 5. 5 Microchannel image following 45 min. of blood perfusion. Occlusion of the majority of the channel lumen generated prohibitively high back pressure, forcing termination of the test.[48]

As a basic, scalable building block to minimize damaging tangential shear forces, we adopted an asymmetrically configured microchannel network design (Figure 5.6). Our design was similar to the computational model of the human pulmonary capillary system described by Huang *et al.*[67] and the network model of endothelialized microcapillaries proposed by Shin *et al.*[68] The latter device embodied a microcapillary system with variable channel widths (ranging from 35 µm to 5 mm) and uniform channel depth (35 µm), and was designed to specifically emulate microvascular physiology and promote the viability of attached cells. Similarly, Kaazempur-Mofrad *et al.*[69] proposed a

variation on this design for the purpose of renal filtration, based on prior fractal-based design concepts.[70] Our microfluidic chip design incorporated the following specific physical properties: 1) The individual channels possess a high aspect ratio, exhibiting a width of 1.197 mm and a channel height of 0.1 mm. The width of the inlet and outlet channels is 3.38 mm, while the overall footprint of the microfluidic array is 2 x 2 cm. The channel height was derived directly from prior computational and experimental results.[57] The channel width was chosen empirically on the basis of practical limitations of current microfabrication capabilities, and was not systematically varied in the current study. 2) The set of microchannels comprising the 2D aligned chip are each interconnected with four other channels in a network configuration, thus allowing alternative flow pathways in the event of single channel occlusion while minimizing the establishment of detrimental pressure gradients that would be observed using a right angled hierarchically branching channel architecture.
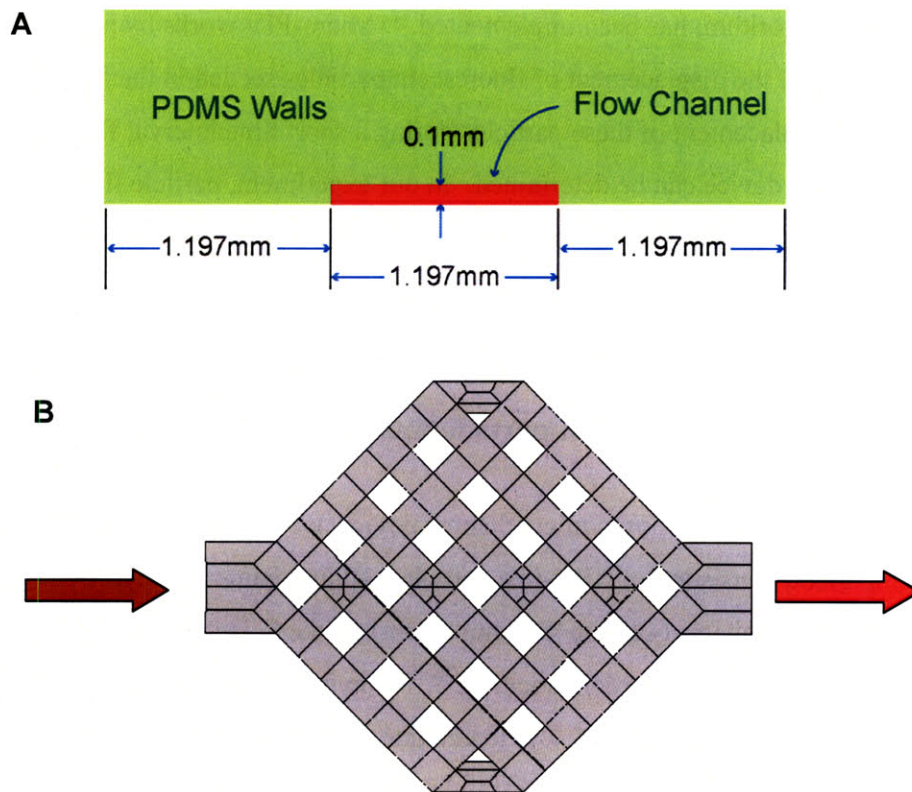
Figure 5. 6 Microfluidic device employing a network construct. A novel construct was employed which combined low channel height for efficient diffusion with relatively broad channel width to minimize shear stress. Shown here are diagrammatic representations of the microchannel network from the perspective of A) An individual microchannel illustrating the asymmetric geometry, height of channel is relatively small compared with channel width. B) Top down view of the overall microchannel network depicting the set of orthogonal interconnections characteristic of the chip configuration.

5.4   Particle tracking

Particle Image Velocimetry (PIV) is an optical method used to measure velocities and related properties in fluids. The velocity information is calculated by the motion of the seeded particles in the fluid. PIV is a non-intrusive technique: The added tracers generally cause negligible distortion to the fluid flow.[71] In order to analyze velocity fields in microfluidic devices with high spatial resolution, Micro-Particle Image Velocimetry (μPIV), which combines fluorescent microscopy and specialized image interrogation algorithm, has been implemented.[72] Micro-PIV works by making measurements of the displacement of fluorescent particles seeded in the fluid. By tracking the displacement of these particles during a short time interval fluid velocities in the microfluidic device can be determined. In our experiment, particle flow was recorded to the high speed camera (AVI format) and exported as digital image files (TIFF format), which were analyzed with a μPIV software.[73]

5.4.1 Flow visualization and particle image velocimetry (PIV)

To display flow in the proposed microchannel device, we prepared a fluid sample emulating blood consisting of RBC-like particles, 10 μm diameter polystyrene green fluorescent microspheres (488 nm/ 508 nm ex/em) (Duke Scientific), and determined local velocity profile with particle tracking.[74-75] The fluorescent microspheres were mixed with deionized water (1:15 v/v) to emulate the intravascular flow patterns of RBCs. Based on the results of the initial flow simulations, a constant flow of 250 μL min^{-1} was selected (Harvard syringe pump) for the experiments. Since the individual microspheres

could not be resolved at this high flow rate, a high speed (1000 frames/sec) camera
(Phantom HD, Vision Research, Inc) was used to capture fluid flow inside the
microfluidic device channels. The captured movies were analyzed using micro-particle
image velocimetry (μPIV), a software method which produces a velocity vector profile of
the non-deforming microspheres present inside the individual channels. By tracking local
displacement of these particles during a short time interval, fluid velocity in the
microfluidic device can be analyzed and represented as local streamlines.
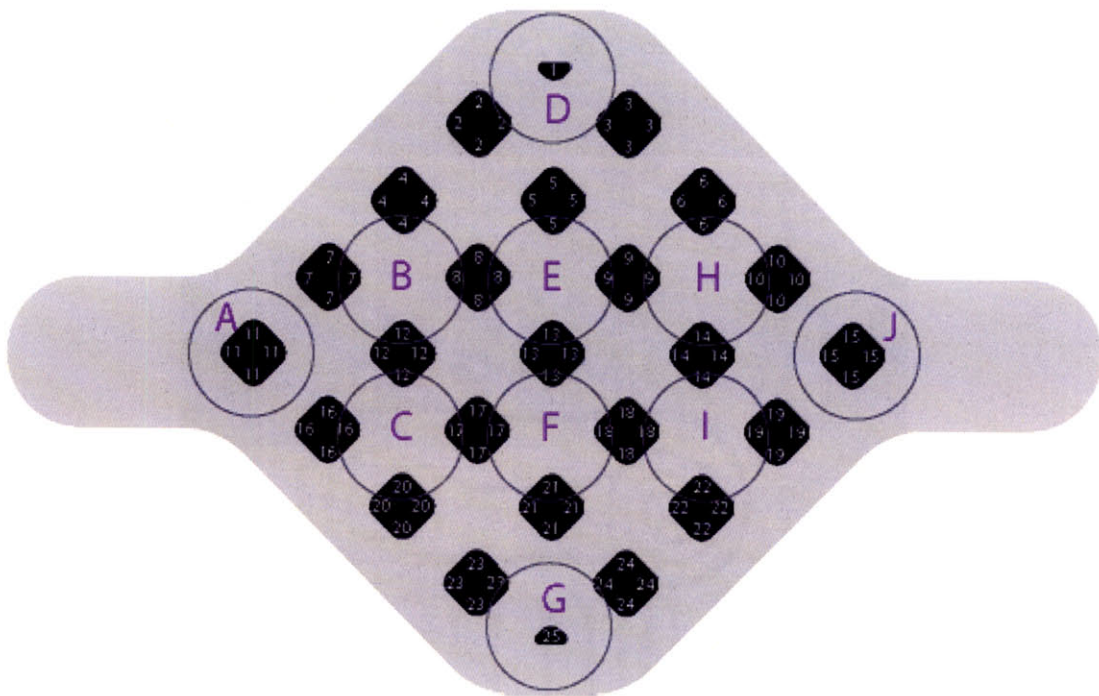
F.5.7.1
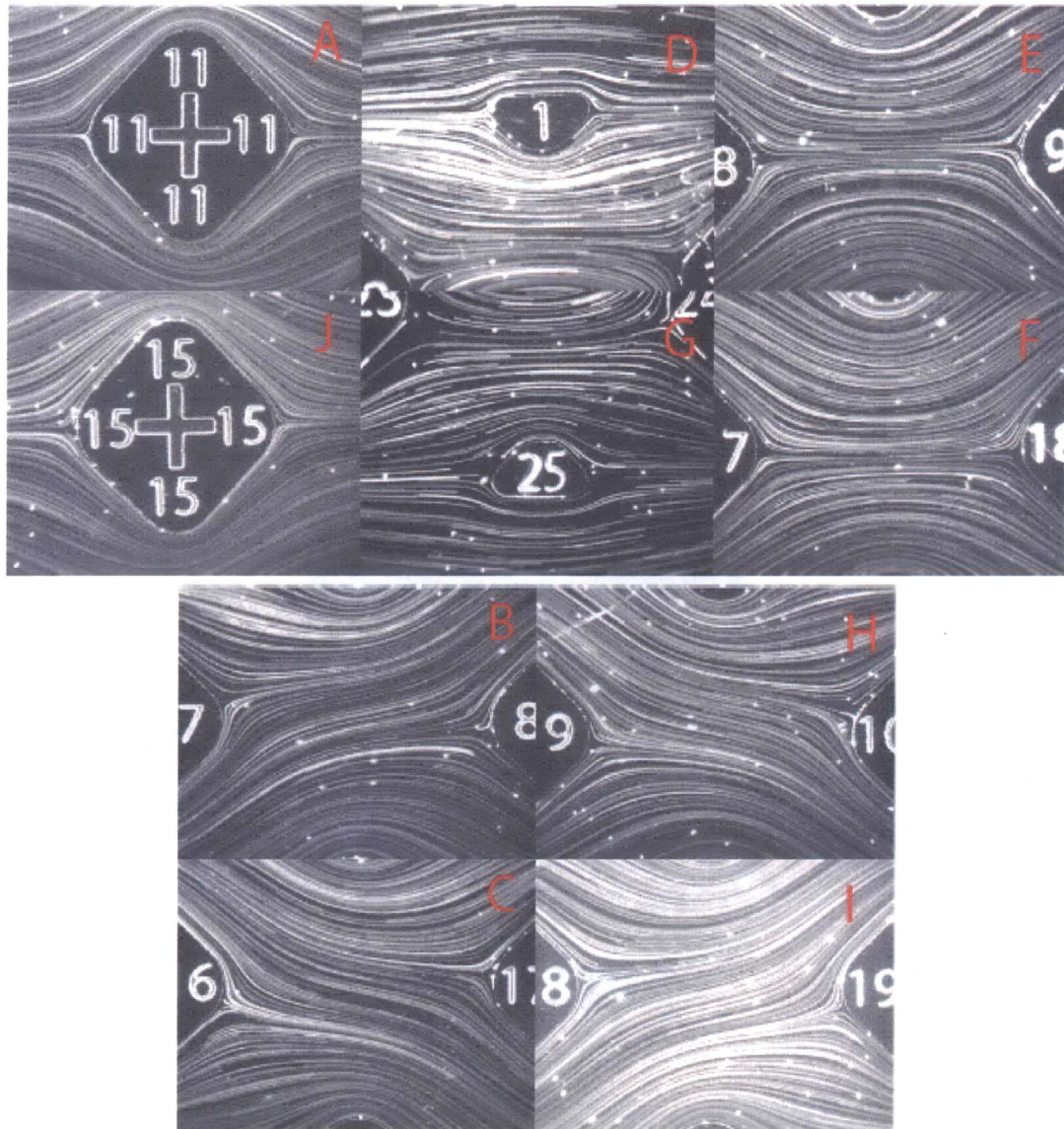
F.5.7.2
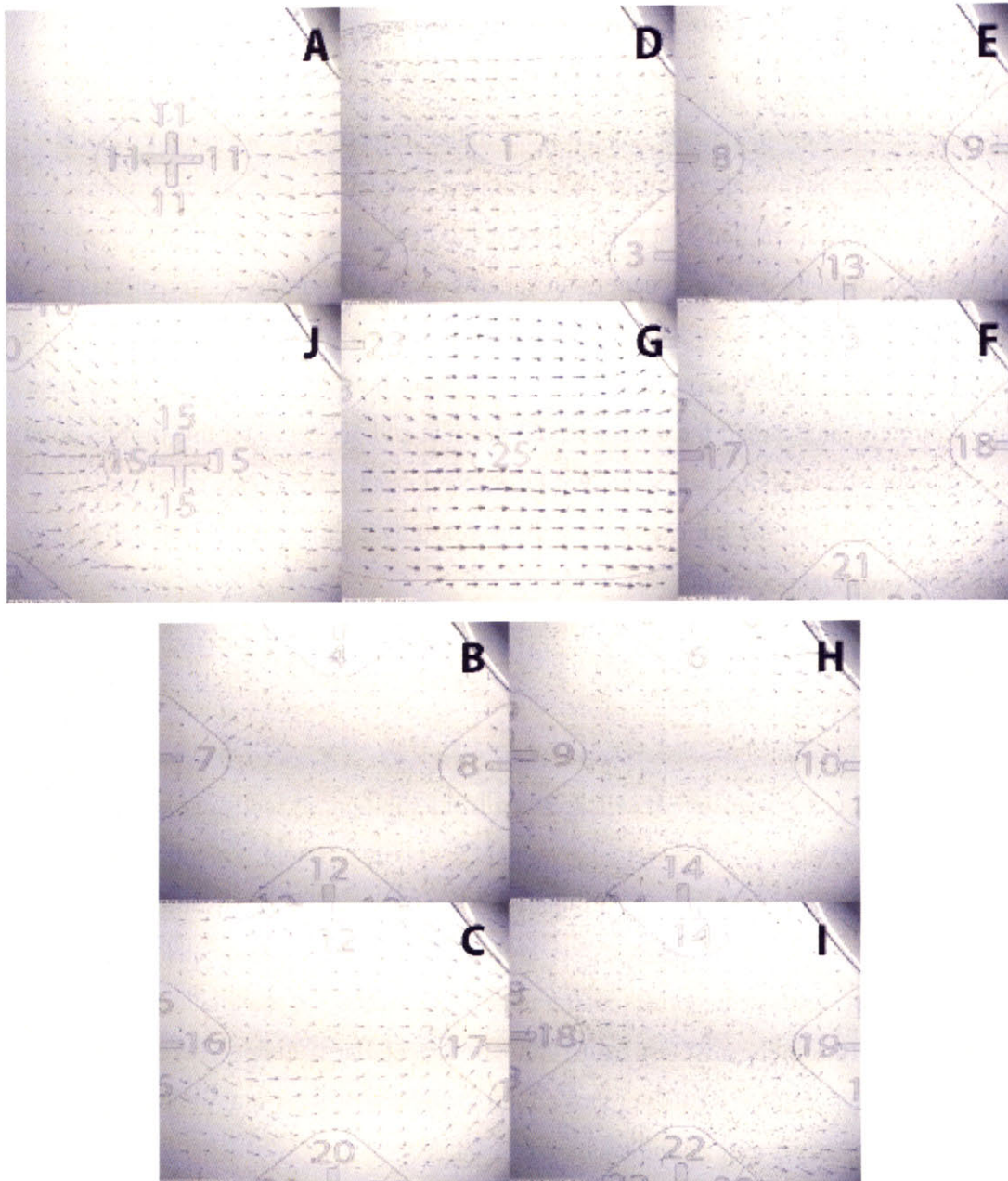
F.5.7.3

Figure 5. 7 Assessment of the attributes of local blood flow by particle tracking To assess the local flow patterns of red blood cells within the chip microchannels, 1:15 mixtures (v/v) of 10 µm size microsphere particles suspended in deionized water were passed through the device at 250 µL min⁻¹. F.5.7.1: The device was marked at key junctions by numbers (1-24), and the interfaces between these junctions labelled by letters (A-J). The flow patterns corresponding to these locations were identified by streamline construction (F.5.7.2) and particles tracking (F.5.7.3) linking the principal directions of the velocity vectors. The upper set of data (A, D, E, F, G, J) depicts velocity profiles around post structures, whereas the lower set of data (B, C, H, I) depicts

velocity profiles around the convergence of flow. These data demonstrate that flow follows well developed and symmetrical streamlines at all points of the microfludic chip.

To assess local flow patterns at key junctions in the chip network, we generated local velocity vector profiles then represented the aligned velocity vectors as streamlines. Each region was identified by a number for tracking purposes. In general, the flow pattern exhibited by the fluorescent microspheres displayed symmetric streamlines (Figure F-2), *i.e.* absence of local turbulence. The velocity of the fluid flow was highest at the inlet and gradually decreased at each junction of mesh bifurcation until it reached its minimum value at half the distance from the inlet and outlet. After this turning point, the velocity started to increase again until it reached it maximum value at the outlet. Particle speed along the same horizontal distance from either the inlet or the outlet was similarly identical, indicating structural symmetry.

5.5 Blood

Human blood is a suspension of cells in an aqueous solution, *i.e.* cells in plasma. The plasma is approximately 90% water by weight, 7% plasma protein, 1% inorganic substances, and 1% other organic substances. Most of the cellular constituents are composed of red blood cells (RBCs or erythrocytes) with white blood cells (WBCs or leukocytes) of various categories making up less than 1/600th of the total cellular volume, and platelets (thrombocytes) less than 1/800th of the cellular volume. There are approximately 5 million RBCs per mm^3, 5000 to 8000 WBCs per mm^3, and 250,000 to 300,000 platelets per mm^3 in human blood.[76]
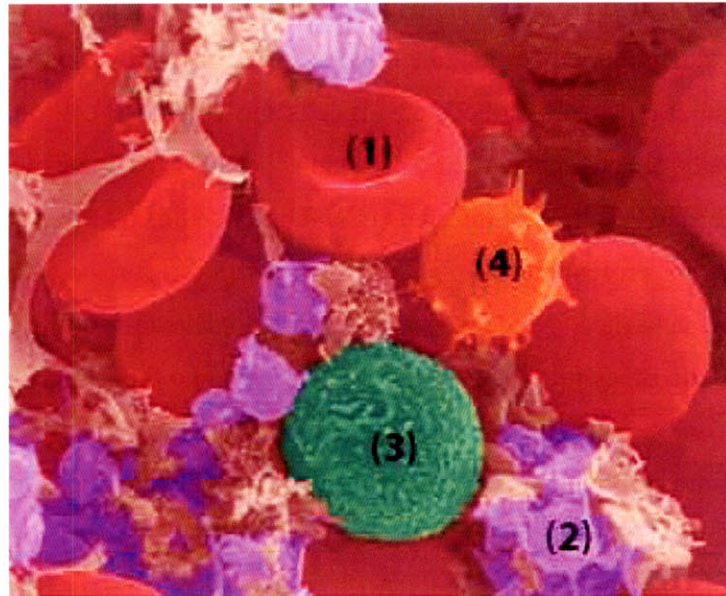
Figure 5. 8 Blood contents (1) Red Blood Cells, (2) Platelets (stained purple), (3) T-Lymphocyte white cell (stained green) (4) Monocyte white cell (stained gold) as seen through a scanning electron microscope.[77]

RBCs form a disk shape, or more specifically thinner in the center and thicker around the edges, with a diameter of 7.6μm and thickness of 2.8μm roughly and take up about 50% of the blood volume. They are extremely flexible and can deform through the blood vessels by aligning the largest dimension paralleled with the direction of the flow. The main function of RBC is to transport oxygen from the lung to the tissues and return carbon dioxide back to the lung. The majority of the red blood cell consists of hemoglobin (approximately 33 % hemoglobin w/w) and its role is to bind molecular oxygen to its heme irons at the lungs and to deliver it to the tissues. It carries the carbon dioxide by-product of oxidation back to the lungs, releasing it to the atmosphere. In contrast, myoglobin stores oxygen in muscle tissue until it is required for metabolic oxidation rather than transporting oxygen.[78]

WBCs are spherical and larger than RBCs. There are several types of white blood cells (leukocytes) and depending on the presence of granules they are categorized into granulocytes (presence of granules) and agranulocytes (absence of granules). Granulocytes come in three different types – neutrophils, basophils, and eosinophils. Neutrophils deal with defense against bacterial infection and inflammatory processes.

Basophils are responsible for allergic and antigen response. Eosinophils deal with parastic infection. Agranulocytes include lymphocytes, monocytes, and macrophages. There are two major types of lymphocytes – B cells and T cells. B cells make antibodies which bind to pathogens to enable their destruction. T cells coordinate the immune response and are able to kill virus-infected cells. They also defend against intracellular bacteria. Monocytes present pieces of pathogens to T cells so that the pathogens may be recognized again and killed. Monocytes are then able to develop into the phagocytosing macrophage cell after they migrate from the bloodstream into the tissue and undergo differentiation.[79]

Platelets are cell fragments that are involved in the cellular mechanisms of primary hemostasis. They measure 1.5 – 3.0 μm in diameter. Platelets are activated when brought into contact with collagen (which is exposed when the endothelial blood vessel lining is damaged), thrombin, receptors expressed on white blood cells or the endothelial cells of the blood vessels, a negatively charged surface (e.g., glass), or several other activating factors. Once activated, they release a number of different coagulation factors and platelet activating factors. Platelet activation further results in the scramblase-mediated transport of negatively charged phospholipids to the platelet surface. These phospholipids provide a catalytic surface for the tenase and prothrombinase complexes. The platelets adhere to each other via adhesion receptors or integrins, and to the endothelial cells in the wall of the blood vessel forming a haemostatic plug in conjunction with fibrin. The high concentration of myosin and actin filaments in platelets are stimulated to contract during aggregation, further reinforcing the plug. Besides being the chief cellular effector of hemostasis, platelets are rapidly deployed to sites of injury or infection and potentially modulate inflammatory processes by interacting with leukocytes and by secreting cytokines, chemokines and other inflammatory mediators.[80-83] (The term *whole blood* that will appear in the context indicates blood that has not been modified in any physical sense.)

A region with a small amount of suspended material exists close to the wall of a blood vessel, *i.e.* plasma rich zone next to the wall. Although this layer is very thin, it has a significant effect on blood rheology. This phenomenon is referred to as the wall-effect. Table 5-1 summarizes the aforementioned blood contents.

	Composition		Concentration
	Water 90% (w/w)		
Plasma	Proteins 7% (w/w)	Albumins	$4.5 - 5.7 \times 10^{-5}$ g/μL
		Globulins	$1.3 - 2.5 \times 10^{-5}$ g/μL
		Fibrinogen	$1.3 - 2.5 \times 10^{-5}$ g/μL
	Salts		
	Dissolved gases		
	Hormones		
	Glucose		
	Metabolites		
	Nutrients		
Cellular Components	Red Blood Cells	7 μm	$3.6 - 5.4 \times 10^{6}$ g/μL
	White Blood Cells	8-20 μm	$5.0 - 10.0 \times 10^{3}$ g/μL
	Platelets	1.5-3.0 μm	$1.5 - 4.0 \times 10^{5}$ g/μL

Table 5. 1 Constituents of human whole blood.[76, 84-86]

5.5.1 Thrombosis and Hemolysis

A blood clot that is coagulated inside the living organism is called thrombus and the process is called thrombosis. A coagulation process is a favorable phenomenon which seals the wounds and stop blood leakage; however it can be extremely dangerous to life once it occurs inside the blood vessels or in the heart. The process basically involves polymerization of fibrinogen into fibrin and the principle mechanism is the conversion of prothrombin into an active enzyme, thrombin. The process is initiated when platelets adhere to the subendothelial collagen at the point of damage to the endothelium. The proteins of the coagulation system, through a series of cascading reactions, eventually form fibrin, the insoluble protein that forms the scaffolding of the thrombus. As blood flows by the thrombus, more platelets and fibrin are deposited. Then, red blood cells and white blood cells become entrapped in the thrombus and are integrated into its structure.

Hemolysis, on the other hand, is the breakage of the red blood cell's membrane, causing the release of the hemoglobin and other internal components into the surrounding fluid. Hemolysis in serum or plasma can be visually observed as pink or red. Hemolysis can occur both *in vivo* and *in vitro*. *In vivo* hemolysis can lead to an anemia and *in vivo* hemolysis can lead to an undesirable effect in medical test; test results from all laboratory disciplines can be affected by hemolysis, especially in chemistry. Hemolysis may cause certain analytes to be increased due to leakage of red cell constituents (e.g., lactate dehydrogenase and potassium), or may cause interference in the test method (e.g., spectrophotometric methods). The amount of interference will depend on the degree of hemolysis and on the specific test method being used.

It is essential to determine biocompatibility of all elements of the microfluidic system during each stage of the design process. The broad question of biocompatibility will require in depth study before the proposed microfluidic artificial respiration device can be considered for the marketplace. Our approach for this challenge is to test biocompatibility of the metal oxide thin film from a materials perspective, effects of plasma and blood constituents on thin film and DO generation, and the effect of construct geometry on blood.

Our work on the biocompatibility testing completed thus far includes hemolysis and preliminary microscopic thrombosis analysis, i.e. the effect of microchannel geometry on blood flow, rate of hemolysis, and thrombus formation with the goal of developing microfluidic structures capable of long-term use while minimizing bio-fouling of the channel. Although more in depth analysis needs to be followed up, our preliminary study on biocompatibility provides a fine path to accomplish this process successfully.

5.6   Experimental and Results (Hemocompatibility)

5.6.1 Experimental set up

The mesh network model was composed of a single flow layer of PDMS attached to blank PDMS substrate. Using PDMS rather than glass as a substrate helped preventing

thrombus formation on the substrate. Glass substrate generated immediate thrombus when exposed to the blood. Any sharp edges were avoided in order to minimize possible thrombosis effect, if any, due to the sharp corners or edges.
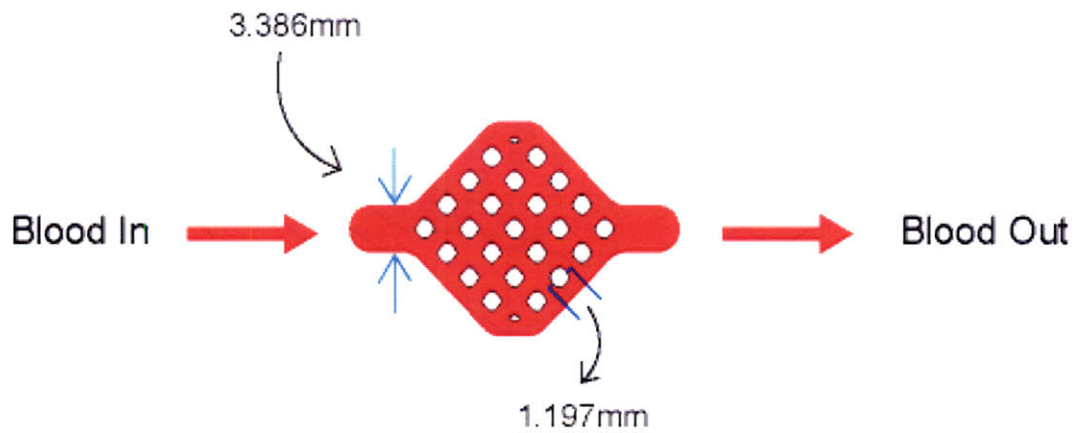
Figure 5. 9 Network model design of microfluidic device with channel width of 1.197mm, and entrance/exit width of 3.386mm.
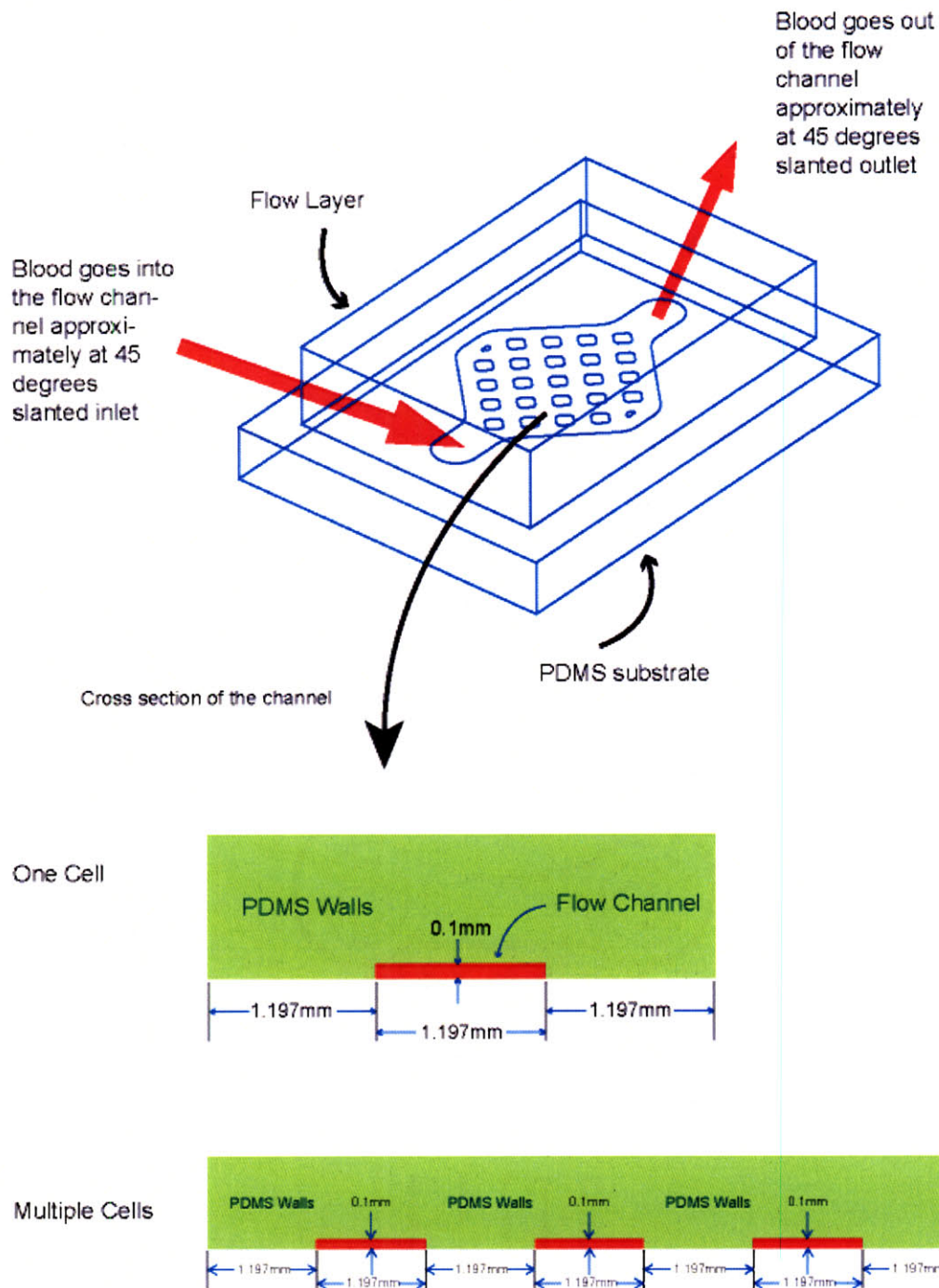
Figure 5. 10 Schematic of the microfluidic device. Single flow layer of PDMS was bonded to the PDMS substrate. Blood was flown in and out of the channel at a slanted angle in order to minimize any possible hemolysis and thrombosis effect.

In order to perform the blood flow test through the chips, 10mL of blood was first directly extracted from a reservoir to a test tube via a 10cc syringe. This was named as a control unit. Then, another 10mL of blood was transported from a reservoir via a 10cc syringe to the test tube through the PDMS structure at the flow rate of 0.250mL/min via syringe pump (Harvard Apparatus). We refer to this as a sample unit. After each cycle was completed, the above procedure was performed repetitively for 6 to 12 hours. After both control and sample were collected in the test tube, they were centrifuged for 10 minutes to obtain blood plasma. 2mL of the plasma mixed with 1mL of cyanmethemoglobin were prepared and the absorption rate was measured under spectrophotometer to calculate the Total Plasma Hemoglobin. After the test was finished, the device was flushed with saline, ethanol, and saline to get rid of any residual blood inside the channel in order to confirm that there was indeed no thrombi formation during the blood perfusion.

5.6.2 Results

Five sets of blood tests were performed to assay the rate of hemolysis and thrombosis generation in the microfluidic device. Bovine blood obtained from a slaughterhouse (Lemay, Goftstown, NH) with a normalized hematocrit (Hct) of 29-30 was used (Autocrit Ultra 3) for each experiment. The blood used was 24 to 120 hours old. No difference was observed in regard to results as a function of blood age. Blood acquired from the slaughterhouse was treated as follows: A solution of 50,000 units Heparin in 1000 ml sterile Dextrose (5%) was combined with approximately 4 gallons of blood obtained from an individual animal. The blood was then gently stirred to distribute the heparin into the fresh blood. The activated clotting time (ACT) was determined by conventional clinical methods and was found to be approximately 400 seconds at room temperature, an accepted value for during clinical cardiopulmonary bypass.[87-90] For assay of hemolysis, 10 mL samples of blood were collected from the device outlets at each time point (every 40 minutes for a total duration of 6 or 12 hours) and compared to a control blood sample that was flowed at the same rate but not through the microfludic device. Both control and sample were collected and were centrifuged for 10 minutes at 3400 rpm

to isolate the plasma. After centrifugation, 2 mL of the plasma was mixed with 1mL of cyanmethemoglobin and the absorption rate was measured by a spectrophotometer (Thermo Spectronic) to calculate the total plasma hemoglobin (TPH) (mg/dl) in terms of absorption x 242.65 + 3.07.[91] Hemolysis was represented as the TPH (sample – control) / TPH (control) during 6 and 12 hour infusions performed at room temperature, at a flow rate of 250 μL min^{-1} as predicted by prior simulation. Since the flow rate and sampling interval did not vary, further normalization procedures[92] were judged to be unwarranted. Thrombus formation was assessed by microscopic visualization of the channels with an upright microscope (Industrial Products Group, Inc) at 5 and 10X magnification during and following flow through the microfluidic chip for 6 and 12 hours at 0.25 mL min^{-1}. Since early platelet activation events associated with activation[93-94] are likely to be undetected by this method, this assay should properly be regarded as a preliminary assessment of in vivo thrombogenesis.

Figure 5. 11 Photos of microfluidic device taken after 7 hours of blood perfusion. The possibility of thrombus formation was studied by microscopy at following a 6 hour perfusion at a constant flow rate of 0.250 ml min⁻¹. Images are displayed at various locations in the microchip at approximate magnifications ranging from 5-10X. Images are displayed immediately following the perfusion period. No thrombus was observed at any point of the device. The width of single channels is 1.197 mm.
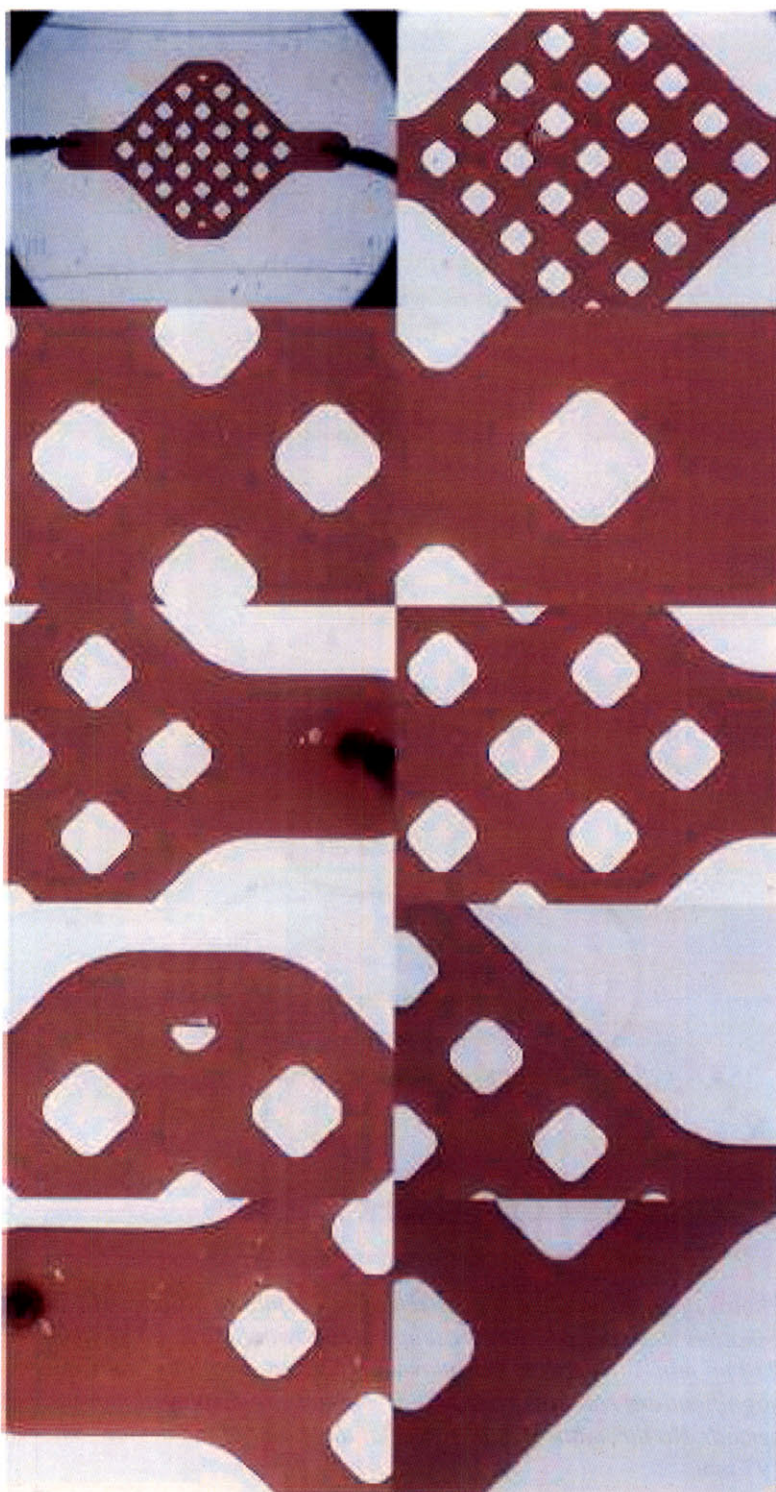
Figure 5. 12 Photos of microfluidic device taken after 12 hours of blood perfusion.
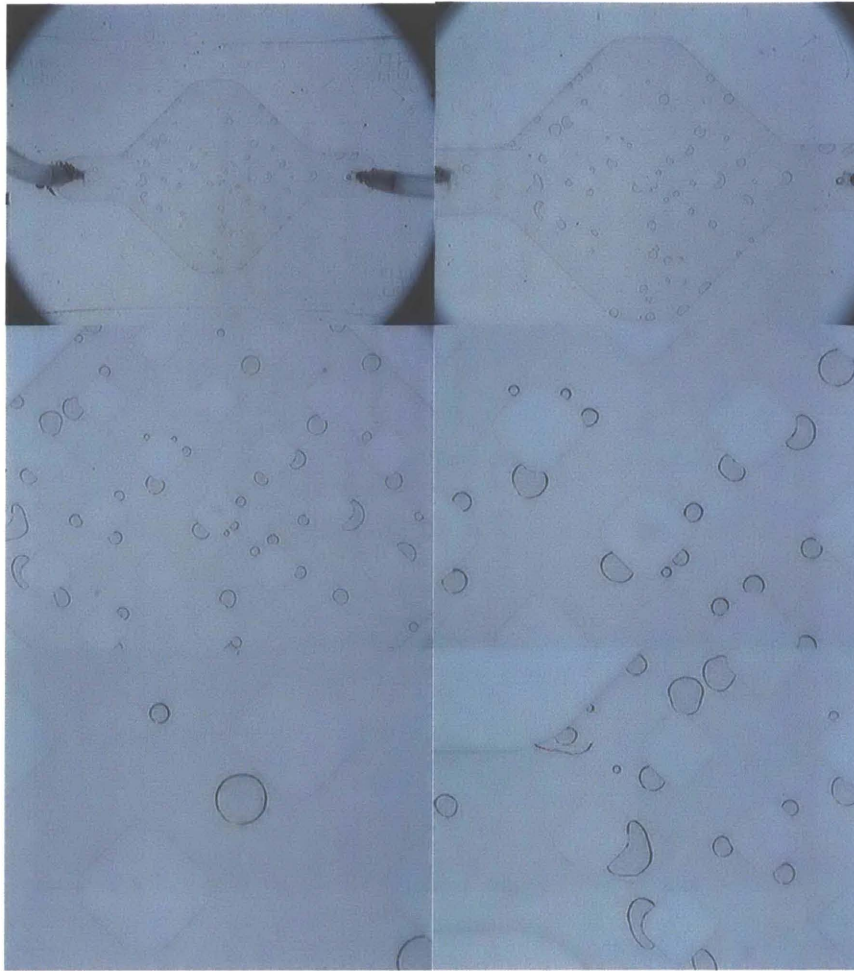
Figure 5. 13 Photos of microfluidic device taken after 12 hours of blood perfusion followed by a flush with saline. They show no residual thrombus formation inside the channels.
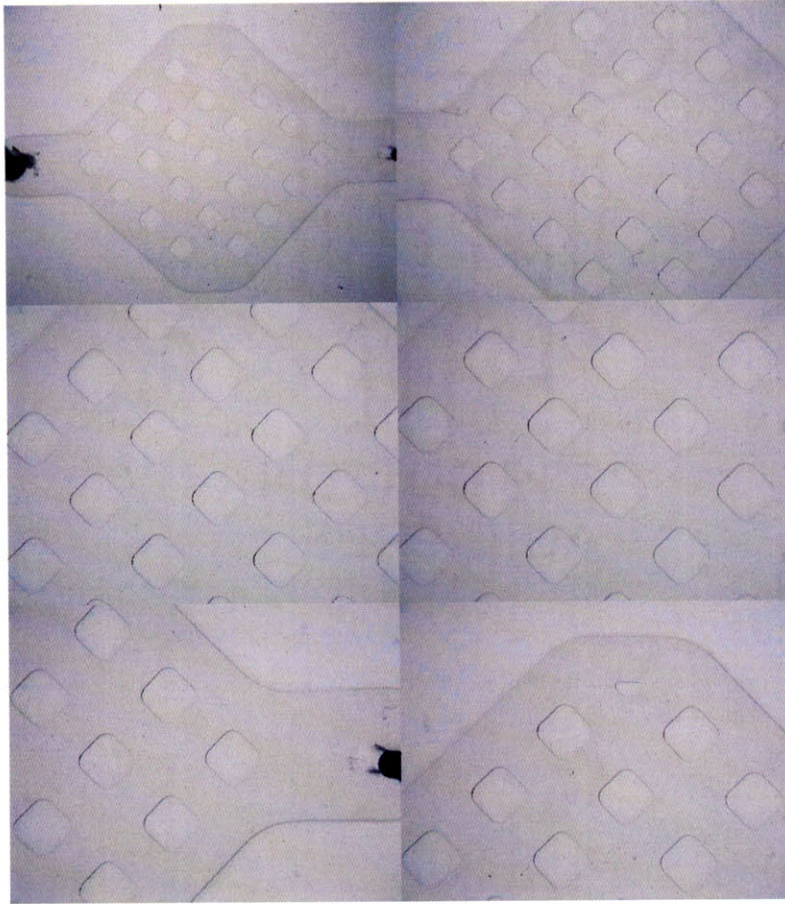
Figure 5. 14 Photos of microfluidic device taken after 12 hours of blood perfusion followed by a flush with saline and additional flush by ethyl alcohol/saline. Ethyl alcohol treatment removed all the air bubbles inside the channel.

Hemolysis Analysis

Flow irregularities related to the geometry of the proposed microfluidic device may result in enhanced shear stress conditions leading to increased hemolysis or significant variations of flow rate resulting in enhanced thrombogenesis. To address the former, the rate of hemolysis was obtained, and represented as the total plasma hemoglobin (TPH) (sample – control) / TPH (control) obtained over a 7 hour perfusion at a flow rate of 0.250 ml min^{-1} (Figure 5.18), a flow condition predicted by previoius simulation to entail minimum hemolysis. Hemolysis rate assayed in this manner was < 5.0% throughout the entire period of device perfusion. The microfluidic chips were further observed for possible thrombus formation following these 6 hour perfusion experiments followed by a washout period. Figure 5.14-15 represents a set of representative microfludic device images. There was no evidence of thrombus formation at any location in the chip. Additionally, in a single long-term (12 hours) experiment, we demonstrated that the total plasma hemoglobin remained stable and not significantly different from control for the entire infusion period and that there was no visible thrombus formation (Figure 5.19).

7 hour device run time (continous perfusion with whole blood)

	Absorption (A)	Total Plasma Hb (mg/dl)	Hemolysis (%)
Control 1	0.228	58.3942	
Sample 1	0.236	60.3354	3.22
Control 2	0.221	56.6957	
Sample 2	0.219	56.2104	-0.86
Control 3	0.223	57.1810	
Sample 3	0.226	57.9089	1.26
Control 4	0.221	56.6957	
Sample 4	0.226	57.9089	2.10
Control 5	0.221	56.6957	
Sample 5	0.226	57.9089	2.10
Control 6	0.222	56.9383	
Sample 6	0.232	59.3648	4.09
Control 7	0.228	58.3942	
Sample 7	0.230	58.8795	0.82
Control 8	0.229	58.6369	
Sample 8	0.227	58.1516	-0.83

Table 5. 2 Hemolysis Analysis. 7 hours of blood perfusion at a flow rate of 0.250mL/min

Total Plasma Hb of Control and Sample
Flow rate: 0.250mL/min
5 Days Old Bovine Blood
Initial HCT 32 % Tested HCT 29%
Running Time: 7 hours

Hemolysis Analysis
Flow rate: 0.250mL/min
5 Days Old Bovine Blood
Initial HCT 32 % Tested HCT 29%
Running Time: 7 hours

Figure 5. 15 Assessment of hemolysis following 7 hour blood perfusion. Hemolysis was determined as a function of flow through the microfluidic construct (sample) compared with flow outside of the microfluidic construct (control) in 4 separate experiments. Samples were obtained every 40 minutes over the course of a 6 hour perfusion at a constant flow rate of 250 $\mu L\ min^{-1}$ and total plasma hemoglobin derived by spectrophotometry. The hemolysis percentage was consistently < 5.0 % and did not increase significantly with the time of perfusion.

12 hours running device run time (continous perfusion with whole blood)

	Absorption (A)	Total Plasma Hb (mg/dl)	Hemolysis (%)
Control 1	0.074	21.0261	7.47
Sample 1	0.081	22.7247	
Control 2	0.123	32.916	-41.82
Sample 2	0.083	23.21	
Control 3	0.084	23.4526	8.52
Sample 3	0.093	25.6365	
Control 4	0.086	23.9379	-5.34
Sample 4	0.081	22.7247	
Control 5	0.095	26.1218	-16.19
Sample 5	0.080	22.482	
Control 6	0.157	42.1661	4.5
Sample 6	0.165	43.1073	
Control 7	0.181	46.9897	-3.2
Sample 7	0.175	45.5338	
Control 8	0.118	37.7027	7.77
Sample 8	0.129	34.3719	
Control 9	0.124	33.1586	0.73
Sample 9	0.125	33.4013	
Control 10	0.131	34.8572	-2.13
Sample 10	0.128	34.1292	
Control 11	0.168	43.8352	-48.5
Sample 11	0.109	29.5189	
Control 12	0.099	27.0924	6.69
Sample 12	0.107	29.0336	
Control 13	0.116	31.2174	-8.43
Sample 13	0.106	28.7909	
Control 14	0.109	29.5189	-5.19
Sample 14	0.103	28.063	
Control 15	0.104	28.3056	1.69
Sample 15	0.106	28.7909	
Control 16	0.106	28.7909	0.84
Sample 16	0.107	29.0336	

Table 5. 3 Hemolysis Analysis. 12 hours of blood perfusion at a flow rate of 0.250mL/min

Total Plasma Hb of Control and Sample
Flow rate: 0.250mL/min
1 Day Old Bovine Blood
Initial HCT 42 % Tested HCT 30%
Running Time: 12hours

Hemolysis Analysis
Flow rate: 0.250mL/min
1 Day Old Bovine Blood
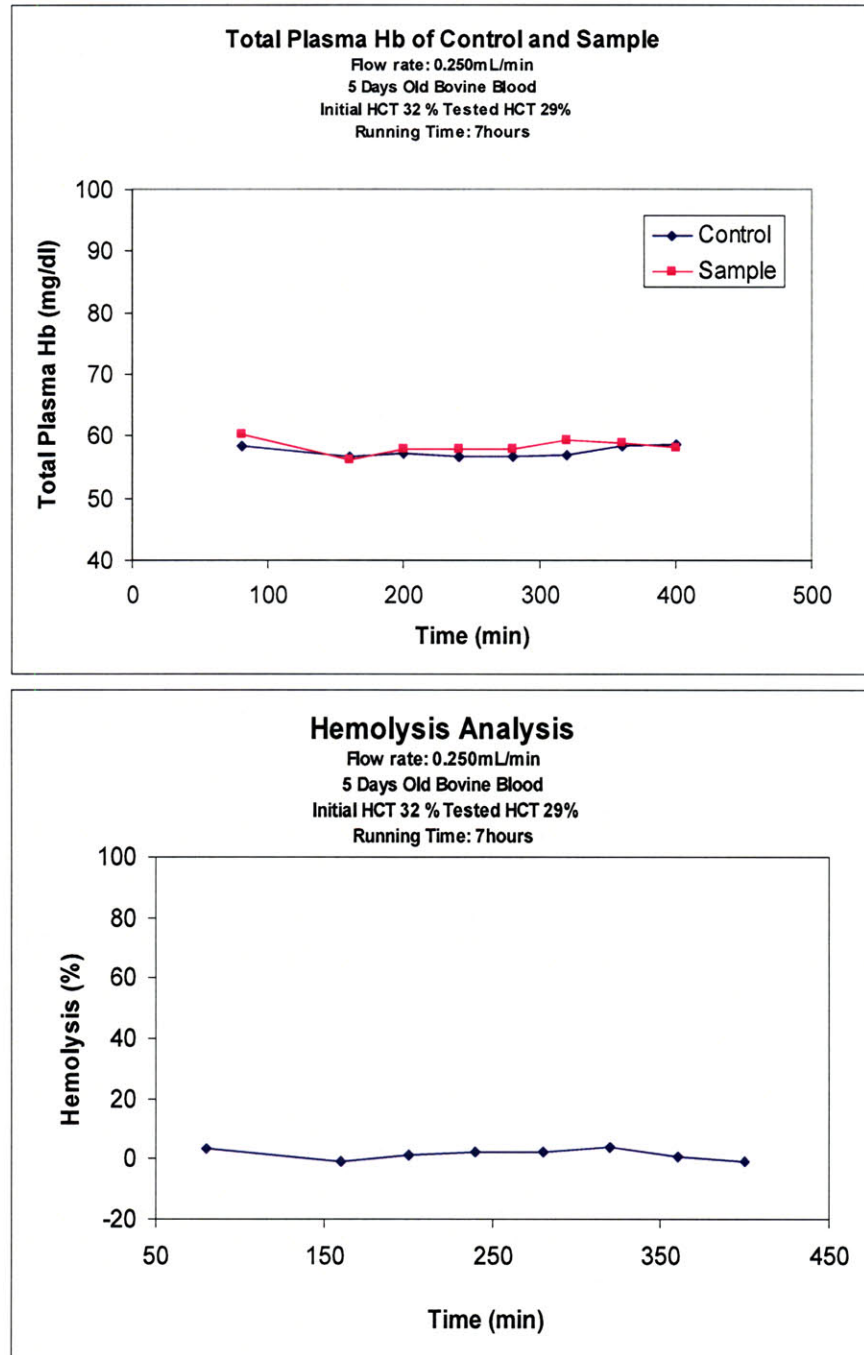Initial HCT 42 % Tested HCT 30%
Running Time: 12hours
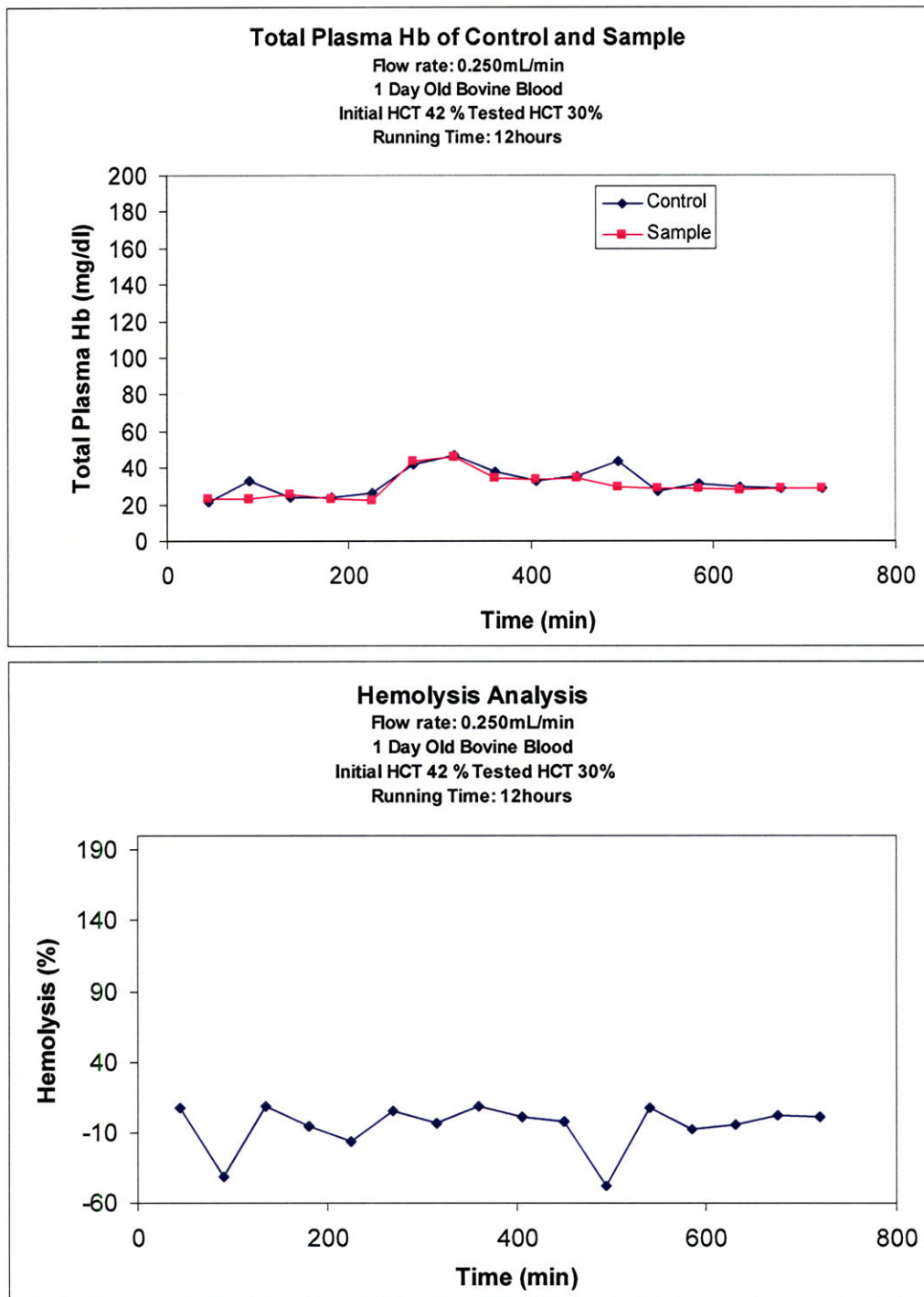
Figure 5. 16 Assessment of hemolysis following 12 hour blood perfusion. Hemolysis displayed as a function of time through the microfluidic construct (sample) compared with flow outside of the microfluidic construct (control). Samples were obtained every 40 minutes over course of a 12 hour blood perfusion at a constant flow rate of 250 μL min^{-1}

(This page intentionally left blank)

Chapter 6

Summary and Conclusions

The ultimate goal of our project is to develop a novel microfluidic device incorporating a photoactive metallic thin film with the capacity to replicate pulmonary capillary respiration in flowing blood. In order to achieve this task, we investigated manufacturing parameters for developing microfluidic devices fabricated from the elastomeric polymer, polydimethylsiloxane (PDMS). In the course of platform development, we have characterized the curing schedules for the heat-cure double layer PDMS ealstomers and investigated interlayer bonding mechanics by analyzing the shear and normal forces required to break the adhesion between the multi-layer PDMS structure. In addition, the pressure required to cause a burst around the microchannels was investigated as well by flowing nitrogen gas directly into the channels.

Fabrication parameters that have been considered in manufacturing multi-layer PDMS devices were catalyst/monomer ratio, primary and secondary bake time, cure temperature, etc. Considering the fact that ideal mixing ratio of PDMS is 10:1 parts A:B (both parts contain different intrinsic ratios of catalyst and monomer), we varied the catalyst/monomer mixing ratio from this reference value to facilitate interlayer bonding.

In the fabrication of two layer devices, the feature size (*i.e.* aspect ratio) played an important role in the success of device manufacture. Microchannels with aspect ratio greater than 10:1 resulted in the frequent failure of multi-layer device fabrication. The primary curing time was critical to the fabrication of multi-layer structure as well. Too little primary cure time in individual layers rendered the PDMS layers be too sticky to be further processed and too much cure time resulted in very poor layer-layer adhesion.

Interlayer bonding analyses (shear, normal, and pressure analysis) revealed the existence of better mixing ratio of certain monomer/catalyst over another in the strength of layer-layer adhesion. For instance, bond strength of a 1:3/1:30 device was much

higher than that of a 1:6/1:15 device. Also, longer secondary baking time produced more robust interlayer bonding. For our device design, the channels could withstand pressures from 23 to 50 psi depending on the monomer/catalyst ratio before the burst between the top and bottom layer occurred.

Based on the manufacture protocols developed, surface modification protocols for polymers were investigated. While silicone rubber (PDMS) is easy to mold and has superior optical clarity, its hydrophobic surface makes it susceptible to non-specific protein adhesion, a particular concern for microfluidic devices to be used in biological assays. Both chemical and physical modifications of the PDMS surface can increase its biocompatibility, rendering the surface hydrophilic or entropically unfavorable for protein adhesion. Most common methods are oxygen plasma treatment, polymer coating or grafting, and chemical treatment with strong acids. We compared the efficacy of these techniques, using fluorescently tagged bacteria flowed through microchannels as reporter particles to measure non-specific adhesion.

Ultimately, utilizing these preliminary data, microscale photocatalytic devices will be designed in such a way that it can be small enough yet to be practical and have high quantum yields of oxygen, *i.e.* to be able to imitate or even exceed the natural capacity of the alveolar-capillary interface. They will also be designed to overcome a challenging subject of biocompatibility of microfluidic devices such as hemolysis and thrombosis, and the final channel network will be constructed to maximize the amount of blood flow and oxygenation while minimizing the damage to circulating red blood cells.

References

1.   R.J. Moreno-Cabral, W.P. Dembitsky, R.M. Adamson, P.O. Daily, Percutaneous extracorporal membrane oxygenation, *Adv. Card. Surg.*, 1994, 5, 163-179.

2.   N.G. Smedira, N. Moazami, C.M. Golding, *et al.*, Clinical experience with 202 adults receiving extracorporeal membrane oxygenation of heart failure, *J. Thorac. Card. Surg.*, 2001, 122, 92-102.

3.   G. Trittenwein, G. Furst, J. Golij, *et al.*, Preoperative ECMO in congenital cyanotic heart disease using the AREC system, *Ann. Thorc. Surg.*, 1997, 63, 1293-1302.

4.   K. Eya, F. Tatsumi, Y. Taenaka, *et al.*, Development of a membrane oxygenator for long-term respiratory support and its experimental evaluation in prolonged ECMO, *ASAIO*, 1996, 42, M832-836.

5.   S.A. Conrad, A. Bagley, B. Bagley, *et al.*, Major findings from the clinical trials of the intravascular oxygenator, *Artificial Organs*, 1994, 18, 846-863.

6.   H. Date, Current status and future of lung transplantation, *Intern Med*, 2001, 40, 87-95.

7.   W. Harringer, K. Wiebe, M. Struber, *et al.*, Lung Transplantation - 10 year experience, *Eur J Cardiothorac Surg*, 1999, 16, 546-554.

8.   J. DeMeester, J.M. Smits, G.G. Persijn, *et al.*, Listing for lung transplantation: life expectancy and transplant effect, stratified by type and stage of lung disease, the Eurotransplant experience, *J Heart Lung Transplant*, 2001, 20, 518-524.

9.   L.D. Sharples, G.J. Taylor, J. Karnon, *et al.*, A model for analyzing the cost of the main clinical events after lung transplantation, *J Heart Lung Transplant*, 2001, 20, 474-482.

10.   J.F. Golob, W.J. Federspiel, T.L. Merrill, B.J., *et al.*, Acute in vivo testing of an intravascular respiratory support catheter, *ASAIO J*, 2001, 47, 434-437.

11.   W.J. Federspiel, T.J. Hewitt, B.G. Hattler, Experimental evaluation of a model for oxygen exchange in a pulsating intravascular artificial lung, *Ann Biomed Eng*, 2000, 28, 160-167.

12.   J.B. Zwischenberger, C.M. Anderson, K.E. Cook, *et al.*, Development of an implantable artificial lung: challenges and progress, *ASAIO J.*, 2001, 47, 316-320

13.   K.A. Dasse, B.F. Monzyk, R.J. Gilbert, *et al.*, Development of a photolytic artificial lung: Preliminary concept validation, *ASAIO J.*, 2003, 49(5), 556-563.

14.   J. Limburg, J.S. Vrettos, L.M. Liable-Sands, *et al.*, A functional model of O-O bond formation by the O_2-evolving complex in photosystem II, *Science*, 1999, 283, 1524-1527.

15.   J.S. Vrettos, G.W. Brudvig, Water oxidation chemistry of photosystem II, *Philos Trans Royal Society of London B Biol Sci*, 2002, 357, 1395-1404.

16.   V.K. Yachandra, V.J. DeRose, M.J. Latimer, *et al.*, Where plants make oxygen: a structural model for the photosynthetic oxygen-evolving manganese cluster, *Science*, 1993, 260, 675-679.

17.   V.K. Yachandra, K. Sauer, M.P. Klein, Manganese cluster in photosynthesis: Where plants oxidize water to dioxygen, *Chem Rev*, 1996, 96, 2927-2950.

18.   P. Fernandez-Ibanez, J. Blanco, S. Malato, *et al.*, Application of the colloidal stability of TiO_2 particles for recovery and reuse in solar photocatalysis, *Water Res.*, 2003, 37(13), 3180-3188.

19.   E. Topoglidis, C.J. Campbell, E. Palomares, J.R. Durrant, Photoelectrochemical study of Zn cytochrome-c immobilized on a nanoporous metal oxide electrode, *Chem Commun (Camb)*, 2002, 21(14), 1518-1519.

20.   A. Hagfeldt, M. Gratzel, Molecular photovoltaics, *Acc Chem Res.*, 2000, 33(5), 269-277.

21.   P. Tsai, C.T. We, C.S. Lee, Electrokinetic studies of inorganic coated capillaries, *J Chromatography B Biomed Appl.*, 1994, 657(2), 285-290.

22.   G.M. Whitesides, D.C. Duffy, D.T. Chiu, et al., Fabrication of microfluidic systems in poly(dimethylsiloxane), *Electrophoresis*, 2000, 21, 27-40.

23.   J. Brandrup and E.H. Immergut, *Polymer Handbook*, 2nd ed., 1974.

24.   B. Huang, H. Wu, S. Kim, B. K. Kobilka, and R. N. Zare, Phospholipid biotinylation of polydimethylsiloxane (PDMS) for protein immobilization, *Lab on a Chip*, 2006, 6, 369-373.

25.   B. Huang, H. Wu, S. Kim, and R. N. Zare, Coating of poly(dimethylsiloxane) with n-dodecyl-β-D-maltoside to minimize nonspecific protein adsorption, *Lab on a Chip*, 2005, 5, 1005-1007.

26.   H. Inoue and S. Kohama, Surface photografting of hydrophilic vinyl monomers
       onto diethyldithiocarbamated polydimethylsiloxane, *J. Appl. Polm. Sci.*, 1984, 29,
       877-889.

27.   A. Papra, A. Bernard, D. Juncker, *et al.*, Microfluidic networks made of
       poly(dimethylsiloxane), Si, and Au coated with polyethylene glycol for patterning
       proteins onto surfaces, *Langmuir*, 2001, 17, 4090-4095.

28.   C. Donzel, M. Geissler, A. Bernard, *et al.*, Hydrophilic poly(dimethylsiloxane)
       stamps for microcontact printing, *Advanced materials*, 2001, 13, 1164-1167.

29.   W. Hellmich, J. Regtmeier, T. T. Duong, *et al.*, Poly(oxyethylene) based surface
       coatings for poly(dimethylsiloxane) microchannels, *Langmuir*, 2005, 21, 7551-
       7557.

30.   J. Lahann, M. Balcells, H. Lu, *et al.*, Reactive polymer coatings: A first step
       toward surface engineering of microfluidic devices, *Anal. Chem.*, 2003, 75, 2117-
       2122.

31.   D. Bodas and C. Khan-Malek, Formation of more stable hydrophilic surfaces of
       PDMS by plasma and chemical treatments, *Microelectronic engineering*, 2006,
       83, 1277-1279.

32.   V. Barbier, M. Tatoulian, H. Li, *et al.*, Stable modification of PDMS surface
       properties by plasma polymerization: Application to the formation of double
       emulsions in microfluidic systems, *Langmuir*, 2006, 22, 5230-5232.

33.   H. Makamba, Y. Hsieh, W. Sung, and S. Chen, Stable permanently hydrophilic
       protein-resistant thin-film coatings on poly(dimethylsiloxane) substrates by
       electrostatic self-assembly and chemical cross-linking, *Anal. Chem.*, 2005, 77,
       3971-3978.

34.   A. Kumar, G.M. Whitesides, Featrues of gold having micrometer to centimeter
       dimensions can be formed through a combination of stamping with an elastomeric
       stamp and an alkanethiol ink followed by chemical etching, *Appl. Phys. Lett.*,
       1993, 63, 2002-2004.

35.   Y. Xia, E. Kim, X.M. Zhao, *et al.*, Complex optical surfaces formed by replica
       molding against elastomeric masters, *Science*, 1996, 273, 347-349.

36.   X.M. Zhao, Y. Xia, G.M. Whitesides, Fabrication of three-dimensional micro-
       structures: Microtransfer molding, *Adv. Mater.*, 1996, 8, 837-840.

37.   E. Kim, Y. Xia, G.M. Whitesides, Polymer microstructures formed by molding in
       capillaries, *Nature*, 1995, 376, 581-584.

38.   J E.Kim, Y. Xia, X.M. Zhao, G.M. Whitesides, Solvent-assisted microcontact molding: A convenient method for fabricating three-dimensional structures on surfaces of polymers, *Adv. Mater.*, 1997, 9, 651-654.

39.   Y. Xia, G.M. Whitesides, Soft lithography, *Annu. Rev. Mater. Sci.*, 1998, 28, 153-184.

40.   Y. Xia and G.M. Whitesides, Soft Lithography, *Chem. Int. Ed.*, 1998, 37, 550-575.

41.   M. A. Unger, H. Chou, T. Thorsen, A. Scherer, and S. R. Quake, Monolithic Microfabricated Valves and Pumps by Multilayer Soft Lithography, *Science*, 2000, 288, 113-116.

42.   F. Garbassi, M. Morra, E. Occhiello, Polymer surfaces, 2nd ed., John Wiley and Sons, New York, 1998, Chapters 2, 6, 7, 12.

43.   M. Morra and E. Occhiello, D. Johnson, *et al.*, On the aging of oxygen plasma-treated polydimethylsiloxane surfaces, *Journal of Colloid Interface Sci.*, 1990, 137, 11-24.

44.   M.K. Chaudhury and G.M. Whitesides, Direct measurement of interfacial interactions between semispherical lenses and flat sheets of poly(dimethylsiloxane) and their chemical derivatives, *Langmuir*, 1991, 7, 1013-1025.

45.   M.K. Chaudhury and G.M. Whitesides, Correlation between surface free energy and surface constitution, *Science*, 1992, 255, 1230-1232.

46.   G.M. Whitesides, A.D. Stroock, I. Gitlin, *et al.*, Components for integrated poly(dimethylsiloxane) microfluidic systems, *Electrophoresis*, 2002, 23, 3461-3473.

47.   C.M. Chan, Polymer surface modification and characterization, Hanser/Gardener Publications, Cincinnati, 1994, Chapters 1, 2 , 5.

48.   G.M. Whitesides, D.C. Duffy, D.T. Chiu, *et al.*, Fabrication of microfluidic systems in poly(dimethylsiloxane), *Electrophoresis*, 2000, 21, 27-40.

49.   D.C. Duffy, J.C. McDonald, O.J. Schueller, G.M. Whitesides, Rapid prototyping of microfluidic systems in poly(dimethylsiloxane), *Anal. Chem.*, 1998, 70, 4974-4984.

50.   J. Jagur-Grodzinski, Heterogeneous modification of polymers, John Wiley and Sons, New York, 1997, Chapters 7, 8.

51.   E. Uchida, Y. Uyama, Y. Ikada, A novel method for graft polymerization onto poly(ethylene terephthalate) film surface by UV irradiation without degassing, *J. Appl. Polm. Sci.*, 1990, 41, 677-687.

52.   T. Richey, H. Iwata, Y. Ikada, *et. al.*, Surface modification of polyethylene balloon catheters for local drug delivery, *Biomaterials*, 2000, 21, 1057-1065.

53.   E. Uchida, Y. Uyama, Y. Ikada, Surface graft polymerization of acrylamide onto poly(ethylene terephthalate) film by UV irradiation, *J. Polym. Sci.: Pt. A*, 1989, 27, 527-537.

54.   S. Hu, X. Ren, N. Allbritton, *et al.*, Surface modification of poly(dimethylsiloxane) microfluidic devices by ultraviolet polymer grafting, *Anal. Chem.*, 2002, 74, 4117-4123.

55.   E.P. Kartalov and S.R. Quake, Microfluidic device reads up to four consecutive base pairs in DNS sequencing-by-synthesis, *Nucleic Acids Research*, 2004, 32, 2873-2879.

56.   B.F. Monzyk, E.C. Burckle, R.J. Gilbert, *et al.*, Photolytically driven generation of dissolved oxygen and increased oxyhemoglobin in whole blood, *ASAIO J.*, 2006, 52, 456-466 .

57.   A.P. Vollmer, R.F. Probstein, R.J. Gilbert, T. Thorsen, Development of an integrated microfluidic platform for dynamic oxygen sensing and delivery in a flowing medium, *Lap on a Chip*, 2005, 5(10), 1059-1066.

58.   A.P. Vollmer, Development of an Integrated Microfluidic Platform for Oxygen Sensing and Delivery, *Master's Thesis* performed under the supervision of Prof. Thorsen and Dr. Gilbert, 2005.

59.   S.S Shevkoplyas, S.C. Gifford, T. Yoshida, M.W. Bitensky, Prototype of an in vitro model of the microcirculation, *Microvasc Res.*, 2003, 65(2), 132-136.

60.   S.C. Gifford, M.G. Frank, J. Derganc, *et al.*, Parallel microchannel-based measurements of individual erythrocyte areas and volumes, *Biophys J.*,2003, 84(1), 623-633.

61.   D. Trebotich, W. Change, D. Liepmann, Modeling of Blood Flow in Simple Microchannels, *Proceeding of Modeling and Simulation of Microsystems*, 2001, 218-222.

62.   W. Huang, R.T. Yen, M. McLaurine, G. Bledsoe, Morphometry of the human pulmonary vasculature, *J Appl Physiol.*, 1996, 81(5), 2123-2133.

63.   R.Z. Gan, Y. Tian, R.T. Yen, G.S. Kassab, Morphometry of the dog pulmonary venous tree, *J Appl Physiol.*, 1993, 75(1), 432-440.

64.   G.E. Kuhnle, J. Groh, F.H. Leipfinger, *et al.*, Quantitative analysis of network architecture, and microhemodynamics in arteriolar vessel trees of the ventilated rabbit lung, *Int J Microcirc Clin Exp.*, 1993, 12(3), 313-324.

65.   T. Onuki, S. Nitta, Computer simulation of geometry and hemodynamics of canine pulmonary arteries, *Ann Biomed Eng.*, 1993, 21(2), 107-115.

66.   A. Vollmer, T. Snyder, M. Kameneva, *et al.*, Development Of A 2D Microfluidic Oxygenation Device. *Presented at the 51st Annual Meeting of the American Society for Artificial Internal Organs*, Washington DC, June, 2005.

67.   Y. Huang, C.M. Doerschuk, R.D. Kamm, Computational modeling of RBC and neutrophil transit through the pulmonary capillaries, *J Appl Physiol.*, 2001, 90(2), 545-564.

68.   M. Shin, K. Matsuda, J. Borenstein, *et al.*, Endothelialized networks with a vascular geometry in microfabricated poly(dimethyl siloxane), *Biomedical Microdevices*, 2004, 6(4), 269-278.

69.   M. Kaazempur-Mofrad, J.P. Vacanti, N.J. Krebs, J.T. Borenstein, A MEMS-based renal replacement system, *Proceedings of the Solid State Sensor, Actuator, and Microsystems Workshop*, Hilton Head, S.C., June 6-10, 2004.

70.   M. Kaazempur-Mofrad, J.P. Vacanti, R.D. Kamm, Computational modeling of flood flow and rheology in fractal microvascular networks. *In Computational Fluid and Solid Mechanics*, Ed. K.J. Bathe, Oxford, Elsevier Science, Ltd, 2001, 864-867.

71.   R.J. Adrian, Bibliography of particle imaging velocimetry using imaging methods, TAM Report:1917-1995, University of Illinois at Urbana-Champaign, 1996.

72.   J.G. Santiago, S.T. Wereley, R.J. Adrian *et al.*, A Particle image velocimetry system for microfluidics, *Experiments in Fluids*, 1988, 25(4), 316-319.

73.   S. Devasenathipathy, J.G. Santiago, K. Takehara *et al.*, Particle imaging techniques for microfabricated fluidic systems, *Experiments in Fluids*, 1983, 34(4), 504-514.

74.   W.L. Lim, Y.T. Chew, T.C. Chew, H.T. Low, Pulsatile flow studies of a porcine bioprosthetic aortic valve in vitro: PIV measurements and shear-induced blood damage, *J. Biomech.*, 2001, 34(11), 1417-1427.

75.   J.B. Dixon, D.C. Zawieja, A.A. Gashev, G.L. Cote, Measuring microlymphatic flow using fast video microscopy, *J. Biomed. Opt.*, 2005, 10(6):064016.

76.   Y. C. Fung, Biomechanics, Mechanical Properties of Living Tissues, Springer-Verlag, New York, 1984.

77.   http://www.mybloodyourblood.org/hs_biology_red.htm 2/13/07.

78.   R.E. Dickerson and I. Geis, Hemoglobin, The Benjamin/Cummings Publishing Company, Menlo Park, 1983.

79.   B. Alberts, A. Johnson, J. Lewis, et al., Molecular Biology of the Cell, Garland, 6th ed., 2002.

80.   A.S. Weyrich, G.A. Zimmerman, Platelets: signaling cells in the immune continuum, *Trends. Immunol.*, 2004, 25: 489-495.

81.   D.D. Wagner, P.C. Burger, Platelets in inflammation and thrombosis, *Thromb. Vasc. Biol.*, 2003, 23, 2131-2137.

82.   M. Iannacone, G. Sitia, M. Isoqawa, *et al.*, Platelets mediate cytotoxic T lymphocyte-induced liver damage, *Nat. Med.*, 2005, 11, 1167-1169.

83.   T.G. Diacovo, K.D. Puri, R.A. Warnock, *et al.*, Platelet-mediated lymphocyte delivery to high endothelial venules, *Science*, 1996, 273: 252-255.

84.   E. P. Solomon, L.R. Berg, C. Villee, *et al.*, Biology, 4th ed., Saunders College, 1996.

85.   E. S. West and W. R. Todd, Biochemistry, third edition, The MacMillan Company, New York, 1961.

86.   L. Bitsch, Blood Flow in Microchannels, Master's thesis, 2002.

87.   S.B. Litwin, S.K. Mitra, J. Lazerson, *et al.*, Use of activated clotting time for monitoring anticoagulation during cardiopulmonary bypass in infants and children with congenital heart disease, *Cardiovasc. Dis.*, 1981, 8(3), 364-371.

88.   J. Hirsh, T.E. Warkentin, J.E. Dalen, *et al.*, Heparin and Low-Molecular Weight Heparin: Mechanism of Action, Pharmacokinetics, Dosing Considerations, Monitoring, Efficacy, and Safety, *Chest*, 1998, 114(5 Suppl), 489-510.

89.   J.J. Ferguson, Conventional anti-thrombotic approaches, *American Heart J.*, 1995, 130(3 Pt2), 651-657.

90. P.G. Hattersley, Activated coagulation time of whole blood, *Am. Med. Assoc.*, 1996, 196(5), 436-440.

91. R. Malinauskas, Plasma hemoglobin measurement techniques for the in-vitro evaluation of blood damage caused by medical device, *Artificial Organs*, 1997, 21, 1255-1267.

92. J. Zhang, B. Gellman, Z.J. Wu, *et al.*, Computational and experimental evaluation of the fluid dynamics and hemocompatibility of the CentriMag blood pump, *Artificial Organs*, 2006, 30(3), 168-177.

93. E.N. Sorensen, G.W. Burgreen, A.F. Antaki, *et al.*, Computational simulation of platelet deposition and activation: I. Model development and properties, *Annals of Biomed. Eng.*, 1999, 27, 436-448.

94. W. Siess, Molecular mechanisms of platelet activation, *Physiol Rev.*, 1989, 69(1), 58-178.